AN EXPERIMENTAL AND NUMERICAL INVESTIGATION
OF MIXED CONVECTION IN RECTANGULAR ENCLOSURES

By

Gregory P. Nurnberg, B.Eng., M.Eng.

A Thesis
Submitted to the School of Graduate Studies
in Partial Fulfilment of the Requirements
for the Degree
Doctor of Philosophy

McMaster University



TO JAN

AN INVESTIGATION OF MIXED
CONVECTION IN ENCLOSURES

DOCTOR OF PHILOSOPHY(1994) McMASTER UNIVERSITY
(Mechanical Engineering) Hamilton, Ontario

TITLE: An Experimental and Numerical Investigation of Mixed Convection in Rectangular Enclosures

AUTHOR: Gregory P. Nurnberg, B.Eng. (McMaster University)
M.Eng.(McMaster University)

SUPERVISORS: Dr. M. Shoukri
Dr. P. Wood

NUMBER OF PAGES: xvi, 232

## ABSTRACT

The cooling of a hot surface by fluid motion has many applications in engineering. For these mixed convective problems, the forced component of fluid motion may be in the direction of the buoyancy vector or it may oppose the buoyancy force. In the present study, the opposing mode is used to study the interaction of inertia and buoyancy forces in a fluid. Both numerical and experimental techniques are used to study the flow in a rectangular cavity of aspect ratio 2.

The inlet Reynolds number is varied between 800 and 1300 and the Grashof number based on the height of the enclosure is varied between 0 and 2.4 X $10^{10}$. The cases considered correspond to Archimedes numbers of approximately 0, 1, 10 and 20.

The flow field is observed qualitatively using laser induced fluorescence and a detailed flow field is generated using a laser doppler anemometer. Temperature profiles are found using fine wire thermocouple probes. These detailed measurements may provide a data base for the verification of computer programs used to predict mixed convection as there are no such detailed data bases in the present literature.

Numerical modelling is based on the SIMPLER algorithm with QUICK differencing. The observed flow field indicated that some regions in the cavity were turbulent while other regions were laminar. This observation suggests the necessity of a low Reynolds number turbulence model. In this study, two forms of the low Reynolds number k-ε model are used. In addition, the commercial computational fluid dynamics program, FLUENT, is used to predict the flow.

Comparison of the experimental and computational results suggest that for isothermal and buoyancy dominated flow cases the computational modelling is adequate. Difficulties arise in the





prediction of the intermediate Archimedes number cases as the predicted flow is dominated by buoyancy while the experiments show more of a balance. Sources for this discrepancy are discussed.





## ACKNOWLEDGEMENTS

The author wishes to express his appreciation to the following individuals and organizations that have contributed to the completion of this study:

- Dr. M. Shoukri and Dr. P. Wood for their supervision, guidance and financial assistance throughout the course of this research program.
- Mr. Joe Verhaeghe and Mr. Ron Lodewyks of the Department of Mechanical Engineering technical staff for their assistance in the instrumentation and construction of the test loop.
- The Ontario Graduate Scholarship Program and the Department of Mechanical of Engineering for their financial support.
- Fellow graduate students, with whom I shared a pleasant, friendly and cooperative working atmosphere.
- My family, especially my parents, for their continued support and encouragement.
- Finally, to Jan and Kelly whose love, continued understanding, support and care provided the incentive to complete this research.




## TABLE OF CONTENTS

TABLE OF CONTENTS (Continued)





TABLE OF CONTENTS (Continued)





## NOMENCLATURE

| | |
|---|---|
| $a$ | Inlet ratio of the cavity (see Equation 2.2) |
| $a_i$ | $i^{th}$ discretization coefficient (see Equations 6.6-6.12) |
| $A$ | Cavity aspect ratio (see Equation 2.3) |
| $A_i$ | Area of the $i^{th}$ face of the control volume |
| Ar | Archimedes number of the system (see Equation 2.6) |
| $c_1$ | Boundary condition descriptor (see Figure 6.3) |
| $c_2$ | Boundary condition descriptor (see Figure 6.3) |
| $c_3$ | Boundary condition descriptor (see Figure 6.3) |
| $C_D$ | Empirical turbulence model constant |
| $C_p$ | Specific heat of the fluid at constant pressure |
| $C_\mu$ | Empirical turbulence model constant (see Table 2.1) |
| $C_1$ | Empirical turbulence model constant (see Table 2.1) |
| $C_2$ | Empirical turbulence model constant (see Table 2.1) |
| $C_3$ | Empirical turbulence model constant (see Table 2.1) |
| $d_f$ | Fringe spacing (see Equation 3.3) |
| $d_m$ | Diameter of LDA measurement volume (see Equation 4.1) |
| $D$ | Inlet height |
| $\text{Đ}$ | Low Reynolds number model extra term (see Table 2.2) |
| $\text{Đ}^*$ | Dimensionless low Reynolds number model extra term (see Equation 5.46) |
| $D_i$ | Conductance across control volume face i (see Equation 6.14) |
| $D_{e^{-2}}$ | Diameter of laser beam |
| $D_H$ | Hydraulic diameter |
| $\hat{E}$ | Low Reynolds number model extra term (see Table 2.2) |
| $\hat{E}^*$ | Dimensionless low Reynolds number model extra term (see Equation 5.48) |
| $E$ | Wall roughness parameter |
| $f_D$ | Doppler frequency (see Equation 3.4) |
| $f_\mu$ | Low Reynolds number model damping function (see Table 2.2) |
| $f_1$ | Low Reynolds number model damping function (see Table 2.2) |
| $f_2$ | Low Reynolds number model damping function (see Table 2.2) |
| $f_3$ | Low Reynolds number model damping function (see Table 2.2) |
| $F_A$ | Apparent focal length of LDA |
| $F_i$ | Mass flowrate across control volume face i (see Equation 6.15) |
| $g_i$ | $i^{th}$ component of the acceleration due to gravity |
| $G$ | Generation of turbulence (see Equation 5.14) |
| $G^*$ | Dimensionless generation of turbulence (see Equation 5.32) |
| $Gr_L$ | Grashof number based on the laminar viscosity (see Equation 2.5) |
| $Gr_T$ | Grashof number based on the turbulent viscosity (see Equation 5.33) |
| $h$ | Local convective heat transfer coefficient |
| $H$ | Cavity height |
| $J_i$ | Flux across control volume face i (see Equation 6.2) |
| $k$ | Dimensional turbulent kinetic energy (see Equation 2.17) |
| $k^*$ | Dimensionless turbulent kinetic energy (see Equation 5.19) |



NOMENCLATURE (Continued)

| | |
|---|---|
| $K$ | Thermal conductivity of the fluid |
| $l_m$ | Length of LDA measurement volume |
| $\ell_m$ | Mixing length (see Equation 2.20) |
| $L$ | Turbulence length scale |
| Nu | Nusselt number (see Equation 7.7) |
| $p$ | Fluid pressure |
| $P$ | Dimensionless pressure |
| $Pe_i$ | Peclet number at control volume face i (see Equation 6.15) |
| Pr | Fluid Prandtl number (see Equation 2.1) |
| Ra | Rayleigh number (see Figure 2.2) |
| Re | Inlet Reynolds number (see Equation 2.4) |
| $Re_t$ | Turbulent Reynolds number (see Equation 2.49) |
| $Re_T$ | Reynolds number based on the turbulent viscosity (see Equation 5.28) |
| Ri | Richardson number of the system (see Equation 2.6) |
| $S^\phi$ | Source term for variable $\phi$ (see Table 6.2) |
| $S_C$ | Constant part of the source term (see Table 6.3) |
| $S_i$ | Sign of the velocity at control volume face i (see Equation 6.26) |
| $S_P$ | Variable part of the source term (see Table 6.3) |
| $t$ | Time |
| $T_J$ | Temperature of the inlet jet |
| $T_R$ | Reference temperature (see Equation 5.5) |
| $T_W$ | Temperature of the heated wall |
| $u$ | Velocity component in the x coordinate |
| $U$ | Dimensionless velocity (see Equation 5.16) |
| $u_J$ | Average volumetric inlet velocity |
| $u^+$ | Dimensionless velocity (see Equation 2.32) |
| $v$ | Velocity component in the y coordinate |
| $V$ | Dimensionless velocity (see Equation 5.16) |
| $w$ | Velocity component in the z coordinate |
| $x$ | Dimensional horizontal coordinate (see Figure 3.1) |
| $X$ | Dimensionless horizontal coordinate (see Equation 5.15) |
| $y$ | Dimensional vertical coordinate (see Figure 3.1) |
| $y^+$ | Dimensionless coordinate (see Equation 2.31) |
| $Y$ | Dimensionless vertical coordinate (see Equation 5.15) |
| $z$ | Dimensional horizontal coordinate (see Figure 3.1) |

**Greek Variables**

| | |
|---|---|
| $\alpha_L$ | Laminar thermal diffusivity of the fluid |
| $\alpha_T$ | Turbulent thermal diffusivity of the fluid (see Equation 5.11) |
| $\beta$ | Coefficient of thermal expansion of the fluid |
| $\gamma$ | Distance from separation height (see Equation 4.2) |
| $\Gamma$ | General diffusion coefficient |
| $\delta_{ij}$ | Kronecker delta (see Equation 2.16) |
| $\delta X$ | Horizontal distance between neighbouring nodes (see Figure 6.2) |

NOMENCLATURE (Continued)

| | |
|---|---|
| $\delta Y$ | Vertical distance between neighbouring nodes (see Figure 6.2) |
| $\Delta t$ | Length of time step |
| $\Delta V$ | Volume of the control volume |
| $\Delta X$ | Width of control volume (see Figure 6.2) |
| $\Delta Y$ | Height of control volume(see Figure 6.2) |
| $\Delta\phi$ | Absolute error in variable $\phi$ (see Equation B.2) |
| $\epsilon$ | Dimensional rate of dissipation of turbulent kinetic energy |
| $\epsilon^*$ | Dimensionless rate of dissipation of turbulent kinetic energy (see Equation 5.20) |
| $\theta$ | Dimensionless temperature (see Equation 5.17) |
| $\Theta$ | Half angle between laser beams |
| $\kappa$ | von Karman's constant |
| $\lambda_o$ | Wavelength of laser light |
| $\mu_L$ | Laminar dynamic viscosity of the fluid |
| $\nu_L$ | Laminar kinematic viscosity of the fluid |
| $\nu_T$ | Turbulent kinematic viscosity (see Equation 2.27) |
| $\nu^*$ | Dimensionless turbulent viscosity (see Equation 7.7) |
| $\pi$ | Pi |
| $\rho$ | Fluid density |
| $\sigma_\epsilon$ | Prandtl-Schmidt number for dissipation rate (see Table 2.1) |
| $\sigma_k$ | Prandtl-Schmidt number for turbulent kinetic energy (see Table 2.1) |
| $\sigma_T$ | Turbulent Prandtl number (see Table 2.1) |
| $\tau$ | Shear stress |
| $\phi$ | General flow variable |
| $\psi^*$ | Dimensionless stream function (see Equation 7.6) |
| $\Psi$ | Turbulence intensity (see Equation 2.46) |

Subscripts

| | |
|---|---|
| b | Constant part |
| BUOY | Buoyancy source term |
| DIS | Dissipation of turbulent kinetic energy source term |
| e | East control volume face (see Figure 6.2) |
| E | East node (see Figure 6.2) |
| GEN | Generation of turbulent kinetic energy source term |
| L | Laminar |
| LIN | Linearized term |
| LR | Low Reynolds number model source term |
| n | North control volume face (see Figure 6.2) |
| nb | Neighbouring points |
| N | North node (see Figure 6.2) |
| P | Computational node being solved for |
| QU | QUICK source term |
| s | South control volume face (see Figure 6.2) |
| S | South node (see Figure 6.2) |



NOMENCLATURE (Continued)

| | |
|---|---|
| T | Turbulent |
| TUR | Turbulent kinetic energy source term |
| VIS | Viscous source term |
| VP | Variable property model source term |
| w | West control volume face (see Figure 6.2) |
| W | West node (see Figure 6.2) |

Superscripts

| | |
|---|---|
| H | Refer to the hybrid differencing scheme |
| Q | Refer to the QUICK differencing scheme (see Equations 6.18-6.25) |
| overbar | Time averaged term |
| ' | Fluctuating term |



## LIST OF FIGURES





LIST OF FIGURES (Continued)

LIST OF FIGURES (Continued)





LIST OF TABLES





# CHAPTER 1

# INTRODUCTION

## 1.1 Nature of the Flows and Heat Transfer

The mechanism of convective heat transfer is referred to as heat transfer to a fluid in motion. The two modes of convection are free and forced convection and the heat transfer rates are usually estimated by considering one of these modes dominant.

As heat is transferred to or from a fluid, the temperature gradients present give rise to density gradients. In the presence of a body force, such as gravity, these density gradients bring about fluid motion. This mode of heat transfer is called free or natural convection. Since the velocity field is determined by the buoyancy effect of the fluid, the velocity and temperature fields are strongly coupled. The heat transfer is usually dependent on fluid properties through the Prandtl and Grashof numbers (see section 2.1 for a definition of these parameters).

In the case of forced convection, the fluid motion is due primarily to some external force. This external force may be the result of a fan, pump, the wind, etc. With this type of convection, usually the velocity field is determined first and the temperature field is determined from it. The heat transfer rate is a function of the Reynolds and Prandtl numbers.

In many engineering applications the effect of buoyancy and forced convection are of the same order. In this case, the heat transfer is referred to as mixed or combined convection. The present study considers this type of convection in rectangular enclosures.





## 1.2 Practical Applications

The study of mixed convection in enclosures has many practical applications in engineering. In many of these applications, the geometry is complex and the flow structures typically exhibit turbulence and recirculation which are difficult to model. Although the present work uses a simple rectangular geometry, it provides a fundamental understanding of the buoyancy/inertial interaction of the flow that is necessary for the prediction of more complex geometries.

Some direct applications include the heating, cooling and ventilation of rooms and buildings, the cooling of electronic components, the study of thermal pollution in water resources, the study of fluid motion in storage tanks used in solar heating, the analysis of heat exchangers, and many applications in the nuclear industry.

## 1.3 Objectives of the Present Work

The present work is a combination of both an experimental and a numerical study of mixed convection in enclosures. While each of these studies complement the other, each has its own objectives.

In the experimental study, the velocity, temperature, and turbulent fields are obtained in the enclosure. In addition, overall heat transfer correlations are presented. The main motivation for the experimental study is to provide experimental data which may be used to compare and verify numerical simulations. This is necessary as there are a limited number of experimental studies.

The numerical study will aid in the future development of numerical codes. Some of the mathematical modelling and some aspects of numerical formulations are strongly problem dependent. As there are no extensive numerical studies of mixed convection in enclosures in the

current literature, the present numerical study will aid in the testing of the performance of some of the models and formulations.

# CHAPTER 2

# LITERATURE SURVEY

## 2.1 Introduction

Before a summary of previous literature is presented, a brief explanation of terminology and parameters used in mixed convection problems is presented. In the present study, the velocity, temperature, and turbulence fields will be obtained both experimentally and numerically in a rectangular cavity. The specific cavity is shown schematically in Figure 2.1. The enclosure shown is a rectangular cavity with a horizontal jet entering in the upper left corner. This inlet jet has specified velocity and temperature profiles ($u_j$ and $T_j$ respectively). The fluid discharges by way of a horizontal duct located in the lower left corner of the cavity. All solid boundaries are insulated with the exception of the right wall, which is maintained isothermally at $T_w$.

This problem may be specified in terms of dimensionless parameters. These are the fluid Prandtl number, the cavity inlet ratio, the cavity aspect ratio, the inlet Reynolds number, and the Grashof number. The Prandtl number, Pr, is a dimensionless parameter defined as the ratio of momentum to thermal diffusion and is expressed as

$$Pr = \frac{\mu_L C_p}{K} = \frac{\nu_L}{\alpha_L} \tag{2.1}$$

where $\mu_L$ is the dynamic viscosity of the fluid,

$C_p$ is the specific heat at constant pressure,

K is the thermal conductivity of the fluid,

$\nu_L$ is the kinematic viscosity, and

$\alpha_L$ is the thermal diffusivity of the fluid.





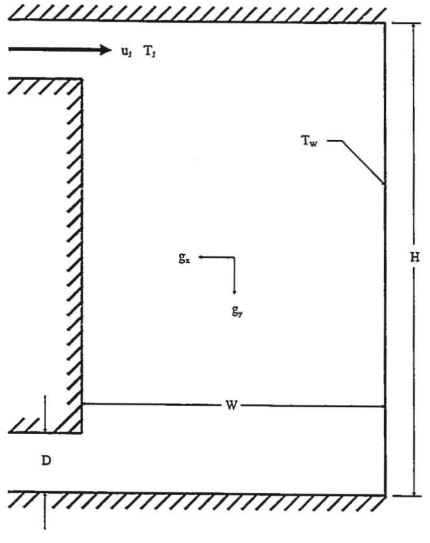


**Figure 2.1: Problem Specification**



The inlet ratio, $a$, is defined as the ratio of the inlet height to the cavity height and is expressed as

$$a = \frac{D}{H} \tag{2.2}$$

It must be noted that, in the current study, the outlet height equals the inlet height. The cavity aspect ratio, A, is the ratio of the height to width of the cavity

$$A = \frac{H}{W} \tag{2.3}$$

The inlet Reynolds number, Re, is the ratio of inertial to viscous forces and is defined as

$$Re_D = \frac{u_j D}{\nu_L} \tag{2.4}$$

The system Grashof number, Gr, is the ratio of buoyant to viscous forces and is expressed as

$$(Gr_i)_H = \frac{g_i \beta (T_W - T_j) H^3}{\nu_L^2} \tag{2.5}$$

In this notation, the subscript $i$ refers to the component of gravity and the subscript H refers to the length scale. In the present work, the non-zero component of gravity is $g_y$. The length scale is the height of the cavity as an important boundary layer forms on the heated wall. Another convenient parameter that is often used with mixed convection is the Archimedes (Ar) or Richardson (Ri) number. In general, this variable is,

$$Ar = Ri = \frac{Gr}{Re^2} \tag{2.6}$$

This parameter is defined as the ratio of buoyant forces to inertial forces and is derived from the buoyant term in the dimensionless momentum equations. This term appears as a source term in the dimensionless governing equations. If the Grashof and Reynolds numbers do not have the same length scale additional dimensionless parameters may be present in this term.

In Figure 2.1, the fluid inertia drives the fluid across the top boundary. As it meets the solid right wall, the fluid turns down the right boundary, and as it meets the lower boundary, the fluid turns horizontally toward the exit. As the fluid flows adjacent to the right boundary, heat is transferred to or from the wall. If the boundary temperature is less than the fluid temperature, the fluid transfers heat to the wall resulting in a downward buoyancy force. Since the buoyancy force is acting in the same direction as the inertial force, the flow is said to be "aiding flow". If the temperature of the wall is greater than the fluid temperature, heat is transferred to the fluid resulting in an upward buoyancy force. Since the buoyancy and inertial forces oppose each other, the flow is said to be "opposing flow". The aiding or opposing nature of the flow may be characterized in terms of the Grashof number.

$$\begin{aligned} Gr_L &> 0 \quad \text{for opposing flow} \\ Gr_L &= 0 \quad \text{for isothermal flow} \\ Gr_L &< 0 \quad \text{for aiding flow} \end{aligned} \tag{2.7}$$

## 2.2 Mixed Convection in Enclosures

The study of mixed convection in internal vertical and horizontal flows has been studied extensively in the past. Typically, the geometry used in most of the research includes flow between parallel plates and flow in tubes and ducts (both circular and non-circular). While the results of this research is insightful, it is not presented in this literature survey for the sake of brevity. However, Gebhart et al. [1] provides a complete literature survey on this topic and others. The research of mixed convection in confined enclosures is limited. A detailed survey of the current literature follows.



### 2.2.1 Previous Numerical Research

Oberkampf and Crow [2] considered an open reservoir with a horizontal inlet jet at the surface on one end of the reservoir and a horizontal outlet port at various heights on the opposite end. The study considered the effects of inflow and outflow, heat transfer and wind shear at the surface. In a well mixed reservoir, the fluid circulates top to bottom by way of large vortices, while in a stratified reservoir, the vertical motion of the fluid is inhibited by buoyancy. Wind speed also had a significant effect on the temperature and flow field. An aiding wind increased the speed of the flow while dissipating a considerable amount of heat (by convection and evaporation). An opposing wind forced the heated jet below the surface and significantly reduced the heat dissipation to the atmosphere. The researchers also reported a high amount of computer time necessary for the simulations.

To study the flow inside solar energy storage tanks, Cabelli [3] used a stream function vorticity approach to calculate a laminar flow field. The results indicate that for a Richardson number greater than about unity, buoyant effects were dominant.

Hjertager and Magnussen [4,5] predicted three-dimensional turbulent flow in a room. In this work both the isothermal and buoyant flows were considered. Comparisons with experiments, indicated that for isothermal flows the prediction is adequate. However, inadequate results were obtained with buoyant flows. Reference [5] states that reliable measurements are needed for the validation of the computer codes.

Shoukri and Ahluwalia [6] studied turbulent mixed convection in enclosures. In this study, an explicit numerical scheme and a two equation, k-ε, turbulence model were employed. The boundary conditions consisted of a square enclosure with two inlets (one at each end) and an outlet port (in the centre) of the bottom wall. The fluid was heated volumetrically in a region in the centre of the cavity. The study indicated that there are strong interactions between the



inertial forces and the buoyancy forces and that these interactions had a significant effect on the temperature field. For the case considered, it was found that for an Archimedes number greater than approximately 0.2, the flow was buoyancy dominated and for Archimedes numbers less than this value, the flow was dominated by inertia. The results also indicated that turbulence modelling was needed for such flow interactions. The k-ε model appeared to give adequate results.

Cha and Jaluria [7,8] studied mixed convection flow for energy extraction. Hot fluid was withdrawn from the top of the cavity and cold water was placed in the cavity at the bottom to preserve thermal stratification. The effect of buoyancy was found to be significant for Richardson numbers greater than 0.1 and was very strong for Ri greater than about 1. The horizontal spread and the vertical mixing was found to be dependent on the inlet parameters.

Oosthuizen and Paul [9] modelled laminar mixed convection using a finite element stream function-vorticity formulation. The problem specification is identical to that of Figure 2.1, with the exception of the left wall being maintained isothermally at the same temperature as the jet temperature. This study found that the buoyancy forces increase the average heat transfer for aiding flow and decrease the heat transfer rate in the case of opposing flow. However, for opposing flow, the heat transfer is enhanced by buoyancy if the Reynolds number is very small. The effect of buoyancy may be neglected if

$$\frac{Nu_{forced}}{Nu_{free}} > 2.5 \tag{2.8}$$

For buoyancy dominated flow, the inertial force tends to make a more uniform heat transfer distribution. For the opposing flow case, the local heat transfer rate is significantly influenced by the Reynolds number.



Kumar and Yuan [10] used a SIMPLE family algorithm to predict laminar mixed convection. In this study, a vertical isothermal jet entered the cavity in the upper left corner. The outlet port (vertical as well) was in the upper right corner. The entire cavity was maintained at a constant temperature. This study concluded that buoyancy effects have been found to be significant on the flow and temperature fields and on the friction factor and heat transfer rate.

Recently, papers have been written which deal with reviews of current numerical analysis. These include the papers of Patankar [11] and Leschziner [12]. While these papers are not written specifically for modelling mixed convection, many of the principles presented may be employed when modelling such flows.

### 2.2.2 Previous Experimental Research

Neiswanger, Johnson and Carey [13] conducted flow visualization and measured local heat transfer for cross flow mixed convection in a rectangular enclosure with restricted inlet and outlets. Until the publication of this paper, the authors claimed that no detailed experimental studies had been conducted on high Rayleigh number mixed convection near vertical walls in enclosures. For Reynolds numbers less than 2000, the flow was laminar. The flow structure changed considerably at a Reynolds number of 5000. Neiswanger et al. suggest that there is a need for more experimental data for different geometries and Prandtl numbers.

Jaluria and Cooper [14] studied negatively buoyant wall flows. In this study, a detailed investigation of penetration, entrainment, and heat transfer characteristics of buoyant wall jets is presented.

### 2.2.3 Natural Convection in Enclosures

A brief review of natural convection in enclosures is presented as this has been studied extensively in the past. In addition, natural convection may be considered a limiting case of mixed convection (completely buoyancy dominated). Thus some aspects of natural convection may be applicable to mixed convection.

The present survey is limited to rectangular vertical cavities. In this configuration, the two vertical walls are differentially heated and the horizontal walls are isothermal (see Figure 2.2). Natural convection problems are usually specified in terms of the fluid Prandtl number, the system Rayleigh number and the cavity aspect ratio. The Prandtl number and aspect ratio have been previously defined and the Rayleigh number is defined as the product of the Grashof and Prandtl numbers. The review papers of Catton [15] and Ostrach [16,17] present complete literature reviews of rectangular vertical cavities as well as others of special interest. Ostrach [16] states that vertical cavities contain all of the essential physics relevant to all confined natural convection problems.

In 1978, the conference on Numerical Methods in Laminar and Turbulent Flow was held at University College, Swansea. During this conference, a session concerning the comparison of numerical techniques applied to standard problems was held. This session concluded that buoyancy driven flow in a cavity with differentially heated sides was an adequate problem for a comparison. For this standard problem, the Rayleigh numbers based on the temperature difference of the vertical walls were set at $10^3$, $10^4$, $10^5$ and $10^6$. The fluid in the cavity had a Prandtl number of 0.71 which corresponds to air.

A year later, after a great deal of discussion with various mathematicians and engineers, it was decided that the two-dimensional problem of Mallison and de Vahl Davis [18] was an adequate test case. Following the discussions, Jones and de Vahl Davis invited contributors to



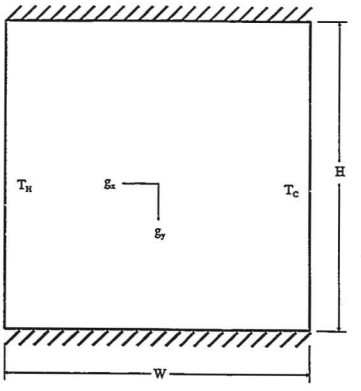


$$Ra = \frac{g\beta(T_H - T_C)H^3}{\nu\alpha}$$

$$Pr = \frac{\nu}{\alpha}$$

$$A = \frac{H}{W}$$

**Figure 2.2: Natural Convection in a Vertical Rectangular Cavity**



submit a solution for the flow and thermal fields. The contributors were requested to submit the following information

(a) the average Nusselt number,

(b) the maximum and minimum local Nusselt numbers on the hot wall and their locations,

(c) the maximum vertical velocity on the horizontal midplane and its location,

(d) the maximum horizontal velocity on the vertical midplane and its location,

(e) contour plots of the velocity components, and, if available, the stream function, the pressure and the temperature.

In 1983, de Vahl Davis and Jones published two papers on this subject [19,20]. The first was a summary and assessment of 37 solutions and the second was the description of a bench mark solution. The authors claim that the bench mark solution is accurate to within one percent. The motivation for obtaining a highly accurate solution was to have something to compare with for validating computer programs. In 1990, Hortmannn et al. [21] used a finite volume multigrid procedure to predict the bench mark solution. They predicted their solution to be accurate to within 0.01%.

Hyun and Lee [22] predicted transient natural convection in a square cavity. This study concluded that if the Prandtl number is greater than unity, oscillations in the solution were evident if

$$Ra > Pr^4 A^{-4} \tag{2.9}$$

The present literature survey for laminar natural convection is restricted to these cases as the bench mark problem may be considered the definitive test case. Several researchers have studied turbulent natural convection using both experimental and numerical techniques. A detailed discussion of this literature is presented after turbulence modelling has been introduced



(see section 2.5). In this section, specific emphasis is placed on the effect of turbulence modelling.

## 2.3 Turbulence Modelling

Turbulent motion is described as being rotational, intermittent, highly disordered, and dissipative [23]. In principle, the instantaneous conservation equations apply equally to a turbulent motion as to a laminar one. However, at present, this is not a practical route as the important details of turbulence are small scale in character. For example, in gaseous flow, the eddies responsible for the decay of turbulence are of the order of 0.1 mm [24]. In most engineering applications, the flow domain is many orders of magnitude larger and hence direct simulations require large computing times and computer memory.

A complete description of different turbulence models is beyond the scope of the present project. Thus the objective of this chapter is to provide an understanding of the need of turbulence models and to provide background information necessary for the discussion of the wall bounded models presented in section 2.4. A comprehensive discussion of turbulence modelling may be found in references [23,24,25].

### 2.3.1 Time-Averaged Governing Equations

Fortunately, in most applications, the engineer is only concerned with the time-averaged effects of turbulence. Thus, the first step towards the modelling of turbulent flow is the decomposition of the flow variables into a time-averaged and fluctuating component. Thus, a given flow variable, $\Phi$, is decomposed by

$$\Phi = \bar{\Phi} + \Phi' \tag{2.10}$$

The overbar denotes the time-averaged value while the prime denotes the random variation about the mean. With the substitution of equation (2.10) into the governing equations, the time-averaged governing equations may be derived. For nearly incompressible flow, the resulting two-dimensional cartesian equations of motion written in tensor notation are:

*Continuity*

$$\frac{\partial \bar{u}_i}{\partial x_i} = 0 \tag{2.11}$$

*Momentum*

$$\frac{\partial \bar{u}_i}{\partial t} + \frac{\partial \overline{u_i u_j}}{\partial x_j} = -\frac{1}{\rho}\frac{\partial \bar{p}}{\partial x_i} + \frac{\partial}{\partial x_i}\left[\frac{\mu_L}{\rho}\frac{\partial \bar{u}_i}{\partial x_j} - \overline{u_i' u_j'}\right] - g_i\beta(\bar{T} - T_R) \tag{2.12}$$

*Energy*

$$\frac{\partial \bar{T}}{\partial t} + \frac{\partial \overline{u_j T}}{\partial x_j} = \frac{\partial}{\partial x_j}\left[\alpha_L \frac{\partial \bar{T}}{\partial x_j} - \overline{u_j' T'}\right] \tag{2.13}$$

In this form, the buoyancy source term in the momentum equation has been modelled with the Boussinesq approximation. This approximation states that the density of the fluid is considered constant except in the buoyancy source term. This term is the last term in equation 2.12 and is responsible for the motion of the fluid due to density gradients. Without this approximation, the buoyancy source term is modelled by $+\bar{\rho}g$. The use of the Boussinesq equation is discussed in Chapter 7. For simplicity, it is usual to drop the overbar in the governing equations on all the terms except the Reynolds stress term, $\overline{u_i' u_j'}$ and the turbulent heat flux term, $\overline{u_i' T'}$. This notation has been adopted in the present work. These equations are not closed as there are more unknowns than equations. The averaged equations of motion differ from their instantaneous counterparts, as the former contains the Reynolds stress term and the turbulent heat flux term. The obvious approach to close the set of equations is to derive exact equations for the Reynolds



stress and turbulent heat flux terms. This is a possible solution to the closure problem but the resulting equations for these terms contain higher order terms [25]. For example, the partial differential equation for the Reynolds stress term, $\overline{u_i' u_j'}$, contains a third order term, namely, $\overline{u_i' u_j' u_k'}$. Equations for the third order terms contain fourth order terms. In general, closure schemes are usually stopped at second order terms and the third order terms are approximated by known variables.

### 2.3.2 The Turbulent Viscosity Concept

Another approach to the closure of the equations is to use a simple turbulence transport model. These models use an eddy or turbulent viscosity concept. Some examples of the models include the zero, one and two equation models where the number of equations refers to the number of partial differential equations in the model.

Boussinesq introduced the first concept of a turbulence model [24]. Analogous to Newton's law of viscosity,

$$\tau_L = \mu_L\left[\frac{\partial u_i}{\partial x_j} + \frac{\partial u_j}{\partial x_i}\right] \tag{2.14}$$

Boussinesq suggested using a turbulent shear stress, $\tau_T$, equal to the product of the mean velocity gradient and a turbulent viscosity. Thus

$$\tau_T = -\rho\,\overline{u_i' u_j'} = \mu_T\left[\frac{\partial u_i}{\partial x_j} + \frac{\partial u_j}{\partial x_i}\right] - \frac{2}{3}\rho\delta_{ij}k \tag{2.15}$$

The turbulent viscosity, $\mu_T$, is not a property of the fluid but is dependent on the local turbulence. Its value may vary from flow to flow and even point to point within a given flow. The first term on the right hand side of equation 2.15 accounts for the shear stress due to turbulent motion just as equation 2.14 accounts for the shear stress due to molecular motion. The second term on the



right hand side of equation 2.15 accounts for the normal stresses due to turbulent motion just as the static pressure, $P/\rho$, accounts for the normal stresses due to molecular motion. The variable, $\delta_{ij}$, is the Kronecker delta and is defined as,

$$\begin{aligned} \delta_{ij} &= 1 \text{ if } i=j \\ &= 0 \text{ if } i\neq j \end{aligned} \tag{2.16}$$

The symbol, k, denotes the turbulent kinetic energy and is defined as

$$k = \frac{1}{2}\overline{u_i' u_i'}\,. \tag{2.17}$$

In a similar manner the turbulent heat flux can be expressed as,

$$-\overline{u_j' T'} = \frac{\nu_T}{\sigma_T}\frac{\partial T}{\partial x_j} \tag{2.18}$$

where $\sigma_T$ is turbulent Prandtl number [26].

The concept of turbulent viscosity provides a basis for turbulence modelling but it itself cannot be considered a model since it can't be determined from calculable quantities. Thus additional modelling must be used in conjunction with the turbulent viscosity concept.

### 2.3.3 Zero Equation Models

The first proposed zero equation model for the turbulent viscosity, $\mu_T$, is the mixing length hypothesis [24]. Prandtl suggested that the turbulent viscosity be described as,

$$\mu_T = \rho\ell_m^2\left|\frac{\partial u_i}{\partial x_j}\right| \tag{2.19}$$

where the mixing length, $\ell_m$, must be prescribed algebraically. The mixing length hypothesis has been tested extensively in the past and has many limitations. This model is based on the assumption that the turbulence is in local equilibrium. Thus, the turbulence is dissipated and produced at the same rate. This hypothesis does not account for the convection, diffusion or



history of turbulence. As a result, the model incorrectly predicts the turbulent viscosity to be zero whenever the velocity gradient is zero [25].

In 1930, von Karman proposed that the mixing length may be modelled using

$$\ell_m = \kappa\left|\frac{\partial u_i/\partial x_j}{\partial^2 u_i/\partial x_j^2}\right| \tag{2.20}$$

where $\kappa$ is von Karman's constant ($\kappa = 0.42$). Von Karman's proposal is limited at inflection points of the velocity profile (i.e. $\partial^2 u_i/\partial x_j^2 = 0$). At this location the mixing length is infinite and cannot be used to compute the finite shear stress.

It must be noted that equation (2.19) and equation (2.20) are based on erroneous physical arguments but can be regarded as definitions for the quantities $\nu_T$ and $\ell_m$ which in simple flows are easier to determine than $\overline{u_i' u_j'}$ itself [27]. In many problems it is difficult to specify the mixing length and in flow situations more complex than shear layers it may be impossible.

Launder and Spalding [24] presented a review of other zero equation models.

### 2.3.4 One Equation Models

In an attempt to overcome limitations of the zero equation models, turbulence models have been developed to account for the transport and history of turbulence. This is accomplished with the use of a transport equation for an acceptable velocity scale of turbulence. Several models use the square root of the turbulent kinetic energy, $\sqrt{k}$, for the dependent variable in the differential transport equation. An exact equation may be derived from the Navier-Stokes equation. The following equation for the turbulent kinetic energy is exact with the exception of the first term on the right hand side. This term, called the diffusion term, assumes that the

diffusion is proportional to the gradient of k. The constant, $\sigma_k$, is an empirical diffusion number commonly referred to as the turbulent Schmidt number.

$$\frac{\partial k}{\partial t} + u_i \frac{\partial k}{\partial x_i} = \frac{\partial}{\partial x_i}\left[\nu_L + \frac{\nu_T}{\sigma_k}\right]\frac{\partial k}{\partial x_i} - \overline{u_i' u_j'}\frac{\partial u_i}{\partial x_j} - \varepsilon \qquad (2.21)$$

The second term on the right hand side accounts for the production of turbulence. The dissipation term, $\varepsilon$, is modelled on the assumption that in an equilibrium flow, the rate of energy dissipated by the smallest eddies is equal to the rate of energy fed down the chain of eddies from the largest to the smallest [23]. The dissipation is determined from

$$\varepsilon = C_D \frac{k^{3/2}}{L} \qquad (2.22)$$

where $C_D$ is an empirical constant and L is a length scale. For the case of buoyant flow, as is the case of mixed convection, an additional term is included in the differential equation to account for the production of turbulent kinetic energy due to buoyancy. This production term is added to the right side of equation (2.21) and is [28]

$$G_B^k = g_i \beta \frac{\nu_T}{\sigma_T}\frac{\partial T}{\partial x_i} \qquad (2.23)$$

This term is naturally obtained as a result of time-averaging the momentum equation when the buoyancy term is included. The turbulent Reynolds stresses are related to the turbulent kinetic energy through the Prandtl-Kolmogorov relationship,

$$\nu_T = C_\mu \sqrt{k}\, L \qquad (2.24)$$

where $C_\mu$ is an empirical constant and L is a length scale which must be prescribed from simple empirical functions similar to those used with the mixing length [23]. Although the equation for the turbulent kinetic energy accounts for the transport and history of kinetic energy, its range of applications is limited by the prescription of the length scale, L. This model works well in



simple shear flows or boundary layers where it is easy to specify the length scale, L. However in complex flows it is no easier to prescribe than $\ell_m$ was in the mixing length hypothesis [25]. Therefore the trend has been to use two equation models where the length scale is also determined from a differential equation.

### 2.3.5 Two Equation Models

For any improvement over the transport models presented thus far, an additional transport equation for the length scale must be used. This allows the length scale to be influenced by transport and history processes in a similar manner to the turbulent kinetic energy [25]. Several models have been adopted such as the k-w, k-ε, and the k-kL models where w represents the square of the vorticity and $\varepsilon$ the rate of dissipation. These models have achieved moderate success. The k-ε model will be discussed in detail as it has been used to predict recirculating flow successfully [23].

The equation for the dissipation of turbulent kinetic energy may be derived from the Navier-Stokes equations. However many modelling assumptions must be made and the result is very empirical [25]. The usual equation for the rate of dissipation of turbulent energy, using the assumption of infinite Reynolds number, is

$$\frac{\partial \varepsilon}{\partial t} + u_i \frac{\partial \varepsilon}{\partial x_i} = \frac{\partial}{\partial x_i}\left[\left(\nu_L + \frac{\nu_T}{\sigma_\varepsilon}\right)\frac{\partial \varepsilon}{\partial x_i}\right] + C_1 \frac{\varepsilon}{k}\nu_T\left(\frac{\partial u_i}{\partial x_j} + \frac{\partial u_j}{\partial x_i}\right)\frac{\partial u_i}{\partial x_j} - C_2 \frac{\varepsilon^2}{k} \qquad (2.25)$$

where $\sigma_\varepsilon$ is an empirical diffusion constant commonly referred to as the Prandtl-Schmidt number for the dissipation rate. Just as a buoyancy term appears in the turbulent kinetic energy equation, some authors use such a term in the rate of dissipation equation. This source term is

$$G_B^\varepsilon = C_3\, g_i\, \beta \frac{\varepsilon}{k}\frac{\nu_T}{\sigma_T}\frac{\partial T}{\partial x_i} \qquad (2.26)$$



Other authors argue that there is no physical reasoning for including such a term and neglect it in the conservation equation [28,29]. Some work has indicated that the inclusion of this term is completely insignificant [29,30].

The normally used constants in the k-ε equation are presented in Table 2.1 [26,31].

**Table 2.1: Constants used in the k-ε Model**

| $C_\mu$ | $C_1$ | $C_2$ | $C_3$ | $\sigma_\varepsilon$ | $\sigma_k$ | $\sigma_T$ |
|---|---|---|---|---|---|---|
| 0.09 | 1.44 | 1.92 | 0.7 | 1.3 | 1.00 | 0.9 |

The complete k-ε model with the inclusion of buoyancy terms in two-dimensional flow is,

$$\nu_T = \frac{C_\mu k^2}{\varepsilon} \qquad (2.27)$$

$$\frac{\partial k}{\partial t} + u\frac{\partial k}{\partial x} + v\frac{\partial k}{\partial y} = \frac{\partial}{\partial x}\left[\left(\nu_L + \frac{\nu_T}{\sigma_k}\right)\frac{\partial k}{\partial x}\right] + \frac{\partial}{\partial y}\left[\left(\nu_L + \frac{\nu_T}{\sigma_k}\right)\frac{\partial k}{\partial y}\right] + G - \varepsilon - \beta g_x \frac{\nu_T}{\sigma_T}\frac{\partial T}{\partial x} - \beta g_y \frac{\nu_T}{\sigma_T}\frac{\partial T}{\partial y} \qquad (2.28)$$

$$\frac{\partial \varepsilon}{\partial t} + u\frac{\partial \varepsilon}{\partial x} + v\frac{\partial \varepsilon}{\partial y} = \frac{\partial}{\partial x}\left[\left(\nu_L + \frac{\nu_T}{\sigma_\varepsilon}\right)\frac{\partial \varepsilon}{\partial x}\right] + \frac{\partial}{\partial y}\left[\left(\nu_L + \frac{\nu_T}{\sigma_\varepsilon}\right)\frac{\partial \varepsilon}{\partial y}\right] + C_1 \frac{\varepsilon}{k} G - C_2 \frac{\varepsilon^2}{k} - C_3 \beta g_x \frac{\varepsilon}{k}\frac{\nu_T}{\sigma_T}\frac{\partial T}{\partial x} - C_3 \beta g_y \frac{\varepsilon}{k}\frac{\nu_T}{\sigma_T}\frac{\partial T}{\partial y} \qquad (2.29)$$

where the mechanical production of turbulence, G, is



$$G = \nu_T\left[2\left(\frac{\partial u}{\partial x}\right)^2 + 2\left(\frac{\partial v}{\partial y}\right)^2 + \left(\frac{\partial u}{\partial y} + \frac{\partial v}{\partial x}\right)^2\right] \qquad (2.30)$$

## 2.4 Wall Bounded Turbulent Flows

As the wall is approached in a turbulent flow field, a further computational difficulty arises. Within a very thin region near the boundary, the effective transport coefficients change by more than an order of magnitude as viscous effects dominate the turbulence effects [30]. In this situation the models presented in section 2.3 are not capable of predicting the flow in their present form as they are based on the assumption of infinitely high Reynolds number. As discussed in the previous section, the zero and one equation models are inadequate to model the complex flow in a cavity. Therefore this section deals solely with wall bounded models used in conjunction with a two equation model of turbulence.

In the wall bounded region, the models must be modified or additional modelling must be incorporated into the fully turbulent models to account for the effect of viscosity near the walls. In an attempt to model this transitional layer, several methods have been adopted. These include wall functions, low Reynolds number modelling, parabolic sublayer, and two layer approaches.

In each subsection of this chapter an overview of these wall bounded models is presented subjectively. At the end of each subsection a discussion of the merits and limitations of each method is presented.

### 2.4.1 Wall Functions

Wall functions are formulae based on experimental data which attempt to account in an overall fashion for the effects of the wall [25]. The usual approach to applying wall functions is to place the first computational grid node in the turbulent region where the logarithmic velocity law may be applied (see Figure 2.3-a).

Unless otherwise stated, most of the information in section 2.4.1 is cited from Ciafalo and Collins [32].

Wall functions commonly assume a viscosity dominated sublayer where the profiles are linear followed by a logarithmic region. If the friction velocity, $u_\tau = \sqrt{\tau_w/\rho}$, is used as a velocity scale and $\nu_L/u_\tau$ as a length scale, the distance and velocity are nondimensionalized by

$$y^+ = \frac{y u_\tau}{\nu_L} \tag{2.31}$$

$$u^+ = \frac{u}{u_\tau} \tag{2.32}$$

The profiles of velocity are assumed to follow [32]

$$u^+ = y^+ \quad \text{for} \quad y^+ \le y_v^+ \tag{2.33}$$

$$u^+ = \frac{1}{\kappa} \ln (E y^+) \quad \text{for} \quad y^+ > y_v^+ \tag{2.34}$$

where $\kappa$ is von Karman's constant ($\kappa \approx 0.42$) and

$y_v^+ \cong 11$.

To ensure continuity at the boundary between the two velocity profiles, E is related to $y_v^+$ by



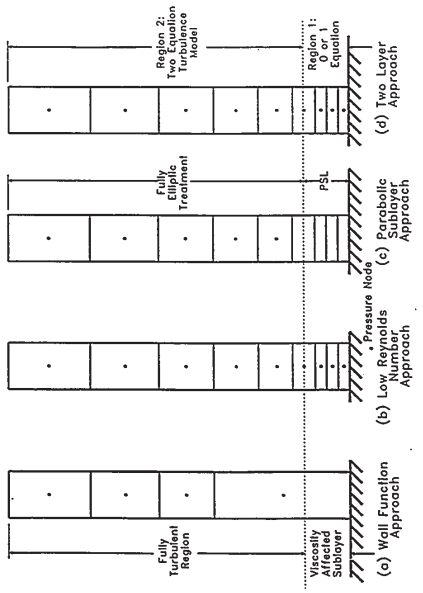


Figure 2.3: Wall Bounded Turbulence Models



$$y_v^+ = \frac{1}{\kappa} \ln \left(E y_v^+\right) \tag{2.35}$$

from which a value of E ≈ 9 has been used by many investigators.

Another common velocity scale is the square root of the turbulent kinetic energy at the near wall grid point, $k_p^{1/2}$. This scaling is derived by solving the kinetic energy equation for a simple shear flow. The shear velocity, $u_\tau$, and the dimensionless distance, $y^+$, can be related to the turbulent kinetic energy by neglecting the diffusion and convection terms and equating the generation and dissipation terms. The distance and velocity are nondimensionalized by

$$y^+ = \frac{C_\mu^{1/4} k_p^{1/2} y}{\nu_L} \tag{2.36}$$

$$u^+ = \frac{u C_\mu^{1/4} k_p^{1/2}}{\tau_w/\rho} \tag{2.37}$$

This scaling is based on the assumption that for an equilibrium boundary layer, the turbulent kinetic energy is almost a constant ($C_\mu^{-1/2}\ \tau_w/\rho$) in the region $20 \le y^+ \le 60$. The velocity profiles are calculated using equations (2.33) and (2.34). $k_p$ is calculated from a modified turbulent kinetic energy equation and the dissipation in the near wall cell is calculated from

$$\varepsilon = \frac{C_\mu^{1/4} k_p^{3/2} u_p^+}{y_p} \tag{2.38}$$

A different approach [32] used the square root of the turbulent kinetic energy at the edge of the viscous sublayer, $k_v^{1/2}$, as the velocity scale. The distance and velocity are nondimensionalized by

$$y^+ = \frac{y k_v^{1/2}}{\nu_L} \tag{2.39}$$



$$u^+ = \frac{u k_v^{1/2}}{\tau_w/\rho} \tag{2.40}$$

The velocity profile within the viscous sublayer is calculated from equation (2.33). Outside the viscous sublayer the velocities are calculated by

$$u^+ = \frac{1}{\kappa^*} \ln \left(E^* y^+\right) \quad \text{for } y^+ > y_v \tag{2.41}$$

where $\kappa^* = \kappa C_\mu^{1/4}$ and

$E^* = E C_\mu^{1/4}$

The sublayer thickness is defined by

$$Re_v = \frac{y_v k_v^{1/2}}{\nu_L} = 20 = \text{constant} \tag{2.42}$$

The value of turbulent kinetic energy at the edge of the viscous sublayer is calculated by extrapolating the value of k at the two grid points nearest the wall. This requires the solution of a cubic equation since y is defined in terms of k .

Outside of the sublayer the profile of turbulent kinetic energy is assumed to be linear, but within the sublayer it is assumed to be parabolic

$$k = k_v \left[\frac{y}{y_v}\right]^2 \quad \text{for } y^+ \le y_v^+ \tag{2.43}$$

The rate of dissipation of turbulent kinetic energy follows

$$\varepsilon = \frac{2\nu_L k_v}{y_v^2} \quad \text{for } y^+ \le y_v^+ \tag{2.44}$$

$$\varepsilon = \frac{k^{1/2}}{C_1 y} \quad \text{for } y^+ > y_v^+ \tag{2.45}$$

where $C_1 = 2.25$.

In the wall function methods described thus far, the near wall region is separated into two regions, namely the viscous sublayer and the logarithmic region. The current literature also describes wall function methods which use a three layer model. In this approach the flow field is divided into three regions. These regions are:

Viscous sublayer for $y^+ \leq 5$,

Buffer layer for $5 < y^+ \leq 30$, and

Fully turbulent region for $y^+ > 30$

Other variations of the wall function method are available in the current literature. Patel and Chen [33] use a two point wall function method and claim that much of the sensitivity of the solutions to the location of the first grid point is removed.

Ciafalo and Collins [32] claim to have developed a new treatment for the prediction of wall bounded turbulent flow. This treatment keeps classic wall functions and scaling based on the near wall turbulent kinetic energy but allows the thickness of the viscous sublayer, $\delta^+$, to vary with the local turbulence intensity, $\psi$. The turbulence intensity is defined as

$$\psi_p = \frac{k_p^{1/2}}{u_p} \tag{2.46}$$

For an equilibrium boundary layer, the distance and velocity, may be scaled using the friction velocity (see equations (2.31, 2.32). The nondimensional turbulent kinetic energy is

$$k^+ = \frac{k}{u_\tau^2} = C_\mu^{-1/2} \left[\frac{y^*}{y_{vo}^*}\right]^2 \quad \text{for } y^* \leq y_{vo}^* \tag{2.47}$$

$$k^+ = C_\mu^{-1/2} = \text{constant} \quad \text{for } y^* > y_{vo}^* \tag{2.48}$$

Equation (2.48) is valid for $y^+$ up to about 50 or 100. Outside of this region the values of $k^+$ depend on the free stream turbulence levels.



The wall function method has been most widely used and is preferred for many practical purposes. This method has two merits. Firstly it economizes computer time and memory and secondly it allows the addition of empirical information in special cases such as incorporating wall roughness [31]. However, as larger and larger computer memories become available, some of the arguments for wall functions begin to weaken [34]. In addition, there are a number of instances in which the standard wall functions approach has to be abandoned, eg. turbulent boundary layers at low and transitional Reynolds numbers, unsteady and separated flows and flow over spinning surfaces [35].

For separated flows and reattaching flows, wall functions with velocity scaling based on $(\tau_w/\rho)^{1/2}$ is unsuitable. In this situation the predicted profiles of Nusselt number gives a minimum value at the reattachment point while experiments show a maximum [32,36].

Wall functions with the velocity scaling based on $(k_p^{1/2})$ are advantageous for unsteady flows and are more general. When used to predict separated flows however, the model yields disappointing results. It underpredicts heat transfer in the low to medium Reynolds number range and overpredicts heat transfer in the high Reynolds number range [32].

Wall functions with the velocity scale based on $(k_p^{1/2})$ also underpredict the heat transfer coefficient for low Reynolds numbers and overpredict the heat transfer coefficient in the high Reynolds number range. In some cases computational difficulties arise when using this scaling [32].

Henkes and Hoogendoorn [37] state that no good wall function exists for the natural convection boundary layer. In addition, the logarithmic wall functions only hold for forced convection boundary layers with small pressure gradients.



At the 12th IAHR meeting, predictions of several computer codes were compared with experimental data from an abrupt pipe expansion. Most of the predictions used a k-$\varepsilon$ turbulence model with wall functions. In general, the peak Nusselt numbers were underpredicted for Reynolds numbers less than $10^5$ and were overpredicted for higher Reynolds numbers [32].

The improved wall treatment of Ciafalo and Collins shows better agreement with experimental heat transfer data. However, there is a need for improvement in heat transfer predictions upstream of reattachment. In this region any wall function fails [32].

### 2.4.2 Low Reynolds Number Modelling

In an attempt to create a model valid in the laminar, semi-laminar and fully turbulent regions, the low Reynolds number approach was devised. In this approach, computations extend into the viscous sublayer. As the wall is approached, the local turbulent Reynolds number, $Re_t$, decreases. Viscous effects become important for turbulent Reynolds numbers less than about 150 [36] where the turbulent Reynolds number is defined by

$$Re_t = \frac{k^2}{\nu_L \varepsilon} \tag{2.49}$$

The number of nodes needed across the viscosity affected sublayer may be as high as twenty or thirty to resolve the highly non-linear variation in turbulent transport coefficients [34] (see Figure 2.3-b).

In this version of the model, k and $\varepsilon$ are determined from

$$\nu_T = C_\mu f_\mu \frac{k^2}{\varepsilon} \tag{2.50}$$



$$\varepsilon = \bar{\varepsilon} + D \tag{2.51}$$

$$\frac{\partial k}{\partial t} + u\frac{\partial k}{\partial x} + v\frac{\partial k}{\partial y} = \frac{\partial}{\partial x}\left[\left(\nu_L + \frac{\nu_T}{\sigma_k}\right)\frac{\partial k}{\partial x}\right] + \frac{\partial}{\partial y}\left[\left(\nu_L + \frac{\nu_T}{\sigma_k}\right)\frac{\partial k}{\partial y}\right] + G - \varepsilon - \beta g_y \frac{\nu_T}{\sigma_T}\frac{\partial T}{\partial y} \tag{2.52}$$

$$\frac{\partial \bar{\varepsilon}}{\partial t} + u\frac{\partial \bar{\varepsilon}}{\partial x} + v\frac{\partial \bar{\varepsilon}}{\partial y} = \frac{\partial}{\partial x}\left[\left(\nu_L + \frac{\nu_T}{\sigma_\varepsilon}\right)\frac{\partial \bar{\varepsilon}}{\partial x}\right] + \frac{\partial}{\partial y}\left[\left(\nu_L + \frac{\nu_T}{\sigma_\varepsilon}\right)\frac{\partial \bar{\varepsilon}}{\partial y}\right] + C_1 f_1 \frac{\bar{\varepsilon}}{k} G - C_2 f_2 \frac{\bar{\varepsilon}^2}{k} - C_3 \beta g \frac{\bar{\varepsilon}}{k}\frac{\nu_T}{\sigma_T}\frac{\partial T}{\partial y} + \hat{E} \tag{2.53}$$

This model differs from the basic version of the k-$\varepsilon$ model by the inclusion of damping functions ("f" functions) to modify the constants, $C_i$ and extra terms are added to better represent the near wall behaviour. The modifications are [35]:

**The dissipation variable, $\bar{\varepsilon}$:** The proposal of using $\bar{\varepsilon}$ as the dissipation variable is due to Jones and Launder [38], who cited decisive computational advantages because $D$ is chosen such that, $\bar{\varepsilon} = 0$, at the wall. This is a numerically convenient boundary condition.

**The function $f_\mu$:** The function $f_\mu$ multiplies the eddy viscosity relation and is introduced to imitate the effect of molecular viscosity on the shear stress.

**The function $f_1$ and the extra term $\hat{E}$:** Several models use a damping function $f_1$ and/or an additional empirical term. This term is used to increase the magnitude of $\hat{E}$ in the vicinity of the wall.

**The function $f_2$:** The function $f_2$ is used to incorporate low Reynolds number effects on the destruction term in the $\varepsilon$ equation.

An evaluation of several low Reynolds number turbulence models is available in [35]. Henkes and Hoogendoorn [37] state that the low Reynolds number models of Lam and Bremhorst [39], Chien [40], and Jones and Launder [38] gave the best results when describing the velocity profiles for natural convection (flow field). The modified forms of the Jones and Launder model [41] and Lam and Bremhorst model [42] are presented in Table 2.2. The variable, n, refers to the distance to the closest boundary.

In one study [36] a low Reynolds number model was applied to an abrupt pipe expansion. This study concluded that the predicted heat transfer coefficient in the vicinity of the reattachment point was seven times greater than that measured. In 1987, Yap [43] found the cause of the problem to be the excessive level of near wall length scales that are generated in separated flows. In an attempt to overcome this problem, Yap suggested adding an additional source term to the rate of dissipation of turbulent kinetic energy equation.

$$S_\varepsilon = 0.83 \left[\frac{\tilde{\varepsilon}^2}{k}\right] \left[\frac{k^{3/2}}{C_l y\varepsilon} - 1\right] \left[\frac{k^{3/2}}{C_l y\varepsilon}\right]^2 \qquad (2.54)$$

With the addition of this term, Yap found the maximum heat transfer coefficient to be comparable with his experiments and the Reynolds number dependence was also improved.

Patel et al. [35] suggest that most modifications to the basic high Reynolds number turbulence model lack a sound physical basis. A major disadvantage of this approach is that a fine grid analysis is necessary in the vicinity of the wall thereby drastically increasing both computational time and memory. However, Launder [36] states that with increasing computing power available, it is feasible to adopt low Reynolds number models in complex flows.



Table 2.2: Typical Low Reynolds Number Models

| | Jones and Launder | Lam and Bremhorst |
|---|---|---|
| $f_\mu$ | $\exp\left[\frac{-2.5}{1 + Re_t/50}\right]$ | $\exp\left[\frac{-3.4}{(1 + Re_t/50)^2}\right]$ |
| $f_1$ | 1.0 | $1 + \left[\frac{0.14}{f_\mu}\right]^3$ |
| $f_2$ | $1. - 0.3\ \exp\left(Re_t^2\right)$ | $\frac{[1 - 0.27\exp(-Re_t^2)] *}{[1 - \exp(-Re_n)]}$ |
| $D$ | $-2\nu_L\left[\frac{\partial\sqrt{k}}{\partial x_i}\right]^2$ | 0 |
| $\hat{E}$ | $2\nu_L\nu_T\left[\frac{\partial^2 u_i}{\partial x_j^2}\right]^2$ | 0 |
| k (b.c.) | k = 0 | k = 0 |
| $\varepsilon$ (b.c.) | $\tilde{\varepsilon} = 0$ | $\frac{\partial\tilde{\varepsilon}}{\partial\eta} = 0$ |
| $Re_n$ | | $\frac{\sqrt{k}\ n}{\nu}$ |

Ciafalo and Collins [32] state that low Reynolds number models are inadequate when applied to separated flows. In some cases they significantly overpredict heat transfer rates while in other cases they significantly underpredict heat transfer.



Ince and Launder [44] applied a low Reynolds number model to natural convection in a vertical rectangular cavity with an infinite aspect ratio. From their study they concluded that the usual forms of the low Reynolds number model do not adequately predict the correct flow rate or heat transfer in the cavity. Agreement was, however, reasonable with the addition of the Yap correction.

### 2.4.3 Two Layer Models

The two layer models approach assumes the flow field can be divided into two fluid layers in the vicinity of the wall. The region adjacent to the wall is modelled with one turbulence model and the other layer is modelled with a different turbulence model. At the interface of the two layers, both models must predict identical flow variables.

One of the most basic two layer models is the parabolic sublayer. The parabolic sublayer (PSL) also adopts a fine grid analysis except that over a thin layer adjacent to the wall the flow is assumed to be parabolic and the variation of static pressure is neglected (see Figure 2.3-c) [45].

In the thin parabolic sublayer adjacent to the wall, major simplifications may be made to the conservation equations. Iacovides and Launder [45] suggest the following simplifications:

(a) The pressure does not need storing as it is given by the pressure just outside the region.

(b) No pressure iteration equation has to be solved.

(c) The velocity normal to the wall may be obtained very rapidly by cell continuity rather than by solving the normal momentum equation.

The benefit of the PSL approach is that it uses a fine grid analysis in the vicinity of the wall without a significant increase in computing costs compared with the wall function method [45].



Chen and Patel [33,46] suggest a slightly more complex two layer model. In this approach the flow field is divided into two regions (see Figure 2.3-d). Region 1 includes the sublayer, buffer layer and part of the logarithmic region while region 2 contains the remainder of the flow field. Region 2 is modelled using a standard two equation, k-ε, model of turbulence while region 1 uses either a zero or one equation model. The main difference between this approach and the PSL approach is that in the latter approach the governing equations are simplified while in the former the fully elliptic equations are solved [46]. Chen and Patel [46] show that the two layer approach is successful in economically solving important features of wall bounded flows.

Two layer models are not easily implemented in general purpose codes, and require special care for each flow. In one instance PSL was not found useful [32].

When compared with the low Reynolds number model, the PSL approach reduced computational times by a factor of two or three when there were no flow reversals present. However, in the case of flow reversal the benefits were significantly reduced [45].

### 2.4.4 Discussion of Near Wall Turbulence Models for Separated Flows

The selection of a near wall turbulence model appears to be very problem dependent. The characteristics of the models were discussed for separated flows and/or reattaching flows. For these types of flows the following conclusions can be drawn:

The wall functions with velocity scales based on the friction velocity, the turbulent kinetic energy of the near wall grid point, or the turbulent kinetic energy at the edge of the viscous sublayer fail to predict heat transfer when separation or reattachment is present. The improved wall function method presented appears to have some promise in predicting the heat transfer distribution but additional work is required.

The two layer models are difficult to incorporate into computer codes. In addition, it is unlikely that the parabolic sublayer approach will save on computing costs.

The usual forms of the low Reynolds number models lack a sound physical basis and are inadequate when applied to separated flows.

The Yap correction applied with a low Reynolds number model appears to yield adequate results.

### 2.5 Turbulence Modelling in Buoyancy Driven Flows

In 1983, Markatos and Pericleous [28] extended the bench mark case study (see Figure 2.2) of laminar natural convection in a two-dimensional cavity to include turbulence. The problem was solved numerically for Rayleigh numbers up to $10^{16}$ using a standard two equation, k-ε, turbulence model with wall functions. It is concluded that the k-ε model is an adequate model for predicting the overall flow structure. However additional research must be conducted to provide more realistic wall functions.

At the University of Washington, Emery's group [47,48] have also studied this problem computationally for Rayleigh numbers up to $10^{12}$. Abrous [47] used a low Reynolds number k-ε turbulence model and Silva and Emery [48] compared the results of a k-ε model and an algebraic stress model. Silva and Emery stated that the algebraic stress model is sensitive to the complex flow in the corners. Larger differences in the prediction of the algebraic stress model and the k-ε are evident in the higher Rayleigh number cases. In addition, significantly finer meshes and higher computing times are required for the algebraic stress model. Silva and Emery also stated that no local experimental data exists to compare with their predictions.

Schmidt's group [41,49,50] studied natural convection in water filled rectangular enclosures both experimentally and computationally. The aspect ratios of the cavities were 2 and



10 and the Rayleigh numbers varied between $5.43 \times 10^8$ to $8.79 \times 10^{10}$. The velocity profiles were measured with a laser doppler anemometer (LDA) and the flow was predicted with a multilevel-multigrid PISO algorithm code. Turbulence has been modelled with either a zero equation or two equation low Reynolds number model. Giel [41] states that the zero equation model is inadequate as the calculations were unstable. In addition the effect of turbulence was studied using two low Reynolds number models. The Humphrey and To [51] model tended to overpredict the turbulence while the Jones and Launder model [38] tended to underpredict the turbulence quantities. In fact, there was no significant difference between the Jones and Launder predictions and the predictions obtained assuming laminar flow. Giel [41] also stated the convergence rate is greatly improved with the implementation of a multilevel-multigrid algorithm.

Cheesewright et al. [52] conducted experiments in a tall two-dimensional cavity of Rayleigh number $4 \times 10^{10}$. Velocity measurements were conducted using a laser doppler anemometer and the core temperatures were obtained. Davidson [42,53] predicted this flow with a low Reynolds number k-ε turbulence model and a hybrid model. The hybrid model combined the non-isotropic properties (due to buoyancy) of the algebraic stress model with the k-ε model. The mean velocity and temperature predictions of both of these models were in excellent agreement with the experimental data of Cheesewright et al. [52]. Davidson [53] stated that both the Reynolds stress model and the algebraic stress model required significantly more computational time than the k-ε model. In addition, they are numerically unstable and may lead to convergence problems. The hybrid model presented overcomes these shortcomings while still accounting for the non-isotropic effects due to buoyancy. The hybrid model predictions of the Reynolds stress and turbulent heat flux were significantly larger than that of the k-ε predictions. Davidson [42] also stated that the convergence rate may be greatly increased with the use of the Coupled Equation Line Solver (CELS) of Galpin and Raithby [54].



Henkes et al. [55] predicted two-dimensional natural convection in a vertical square cavity for Rayleigh numbers up to $10^{14}$ for air and up to $10^{15}$ for water. In this study, the results of a standard k-ε model were compared with the results of two low Reynolds number k-ε models, namely, the Jones and Launder [38] and the Chien [40]. The standard k-ε model with wall functions was found to overpredict the turbulence quantities by 30%. For water, the standard k-ε model predicted negligible values of turbulence quantities (k, ε and $\nu_T$) for Rayleigh numbers up to $10^{11}$ while the Jones and Launder model predicted negligible turbulence quantities for Rayleigh numbers up to $10^{13}$. The predictions of the low Reynolds number models suggests that nonunique solutions can be obtained in the laminar turbulent transition regions. However, for all models tested, unique solutions exist for fully turbulent flows.

Lankhorst et al. [56] used the LDA technique to measure the velocity profiles in an air filled cavity. The Rayleigh number range for the measurements were $1 \times 10^9$ to $4 \times 10^9$. The measurements were compared with the predictions of Lankhorst et al. [57]. For a Rayleigh number of $10^9$, the predicted velocity profile agreed well with the measured profile. However at a Rayleigh number of $2 \times 10^9$, the three-dimensional computation predicted the velocity peak within the boundary layer and the two-dimensional calculation had better agreement at the edge of the boundary layer.

To date, there have been no systematic studies on the various turbulence modelling methods in mixed convection with flow reversal. Since the selection of an adequate turbulence model is problem dependent, some conclusions have been drawn from the current literature pertaining to turbulence models for separating flow and turbulence models for buoyancy driven flow. These publications suggest that a low Reynolds number k-ε turbulence model applied with the Yap correction may yield adequate results. The objective of the present numerical investigation is to complete a systematic study of different forms of the k-ε turbulence model and



to test the performance of various mathematical models and numerical formulations when applied to mixed convective flows in cavities.

# CHAPTER 3

# EXPERIMENTAL APPARATUS

## 3.1 Introduction

This chapter presents a brief description of the experimental apparatus.

Since the computer code developed in the present work is based on two-dimensional conservation equations (see Chapter 5), the test cell has been designed to produce this type of flow as closely as possible. A description of the materials, dimensions, and components of the test cell are presented in section 3.2. In addition the components of the flow loop are also described in this section.

The velocity and turbulence fields are investigated using flow visualization and are measured with a Laser Doppler Anemometer (LDA). This measuring technique has many advantages. These include [58]

(i) Does not disturb the flow,

(ii) High spatial resolution,

(iii) Fast response,

(iv) Response is linear and easily calibrated,

(v) Directional discrimination is possible, and

(vi) Operation is not usually seriously affected by temperature.

A brief theory and description of the LDA is presented in section 3.4.

The temperature fields are measured with fine wire thermocouple probes. These thermocouples give good accuracy, spatial resolution and frequency response to measure the





temperature field within the cavity. The geometry of the thermocouple probes and the choice of material and size are discussed in section 3.5.

## 3.2 Description of Test Cell and Loop

### 3.2.1 The Test Cavity

An acrylic test cell is used to obtain two-dimensional results. The test cell is constructed from 25.4 mm thick clear acrylic and has height of 297 mm, a width of 149 mm, and a depth of 48.5 mm as shown in Figure 3.1. A horizontal jet, of width 8 mm ($D_H$ = 13.7 mm), enters the cavity at the top of one of the vertical walls. A 203 mm flow development length is incorporated into the cavity to assure fully developed flow. The inlet to this development length is by way of a 12.7 by 12.7 mm ($D_H$ = 12.7 mm) entrance. Using a similar inlet, Johnson [59] found the inlet jet to be two-dimensional. The flow exits the cavity horizontally at the bottom of the same vertical wall. The exit is geometrically identical to the entrance.

The opposite vertical wall is constructed from a 9.5 mm thick copper plate and is maintained at a uniform temperature by 10 electric film heaters as shown in Figure 3.2. These heaters are placed on the back of the copper wall (not the flow side), have dimensions of 48.5 by 29.7 mm each, and are controlled independently. Eighteen iron/constantan thermocouples are used to measure the inner wall temperature and are located approximately 0.5 mm from the inner surface. Ten thermocouples are located on the centre line of the copper wall and eight are offset to determine the validity of the two-dimensional heating assumption.

The pressure is monitored using a pressure gauge mounted at the top of the test cavity. The entire cavity is insulated with 25.4 mm expanded polystyrene to reduce heat losses to the atmosphere.



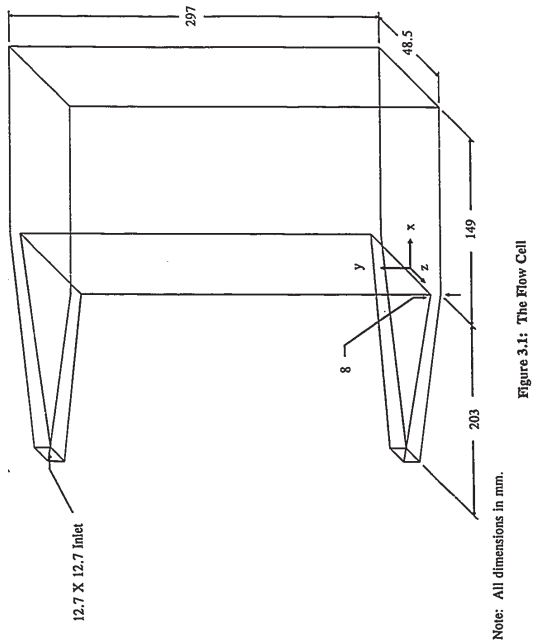


Figure 3.1: The Flow Cell



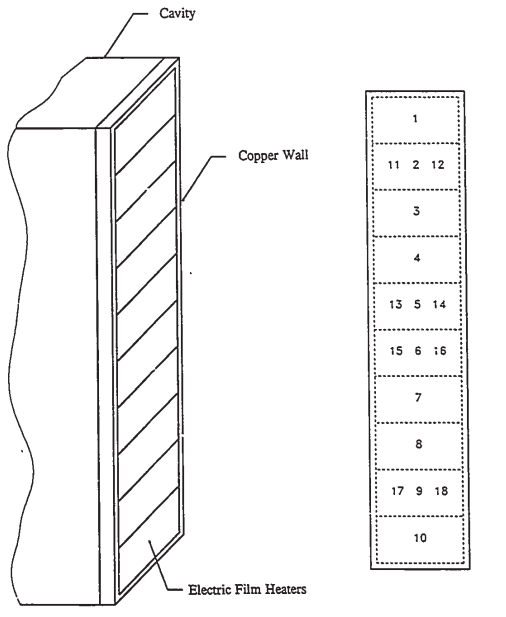


(a) Heater Locations (b) Thermocouple Locations

Figure 3.2: The Heated Wall

### 3.2.2 The Test Loop

The flow cell is placed in the flow loop as shown in Figure 3.3. Water flows from the head tank to the inlet of a centrifugal pump (Little Giant model 3E-12NRT). The outlet of the pump is connected to a flow control valve where the water may flow into a flowmeter (Brooks Rotameter A-8M-25-4) or it may flow in a bypass loop back to the pump inlet. From the flow meter the water flows into the test cell where it is heated by the electric film heaters. After leaving the cavity, the water enters a return line and flows to a counterflow heat exchanger where it is cooled and then returns to the head tank. Coolant water to the heat exchanger is provided by cold tap water and is controlled by a control valve.

## 3.3 Flow Visualization

For a qualitative description of the flow field, flow visualization was carried out using two different methods. These techniques provide insight into the overall flow field and give an indication of the two-dimensionality of the flow. In addition, the location of the separation point adjacent to the heated wall may be identified. The motion of the flow field in a plane is observed by illuminating a foreign material that has been introduced into the test cavity. The motion of the material, and hence the motion of the fluid, is recorded with a camera.

The first procedure is referred to as particle streak flow visualization. With this technique, the flow loop is seeded with particles which are illuminated by a plane of light. Selection of the particle size, density and shape are important as the particles may or may not follow the flow. It is required that the particles be able to follow the turbulent fluctuations. The time scale of the turbulent fluctuations is estimated by the Kolmogorov time scale.



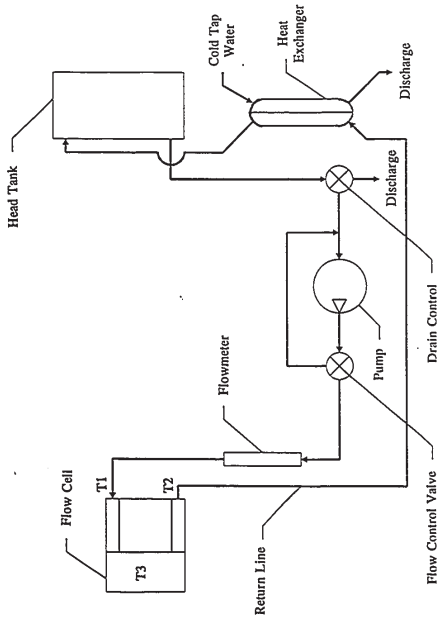


Figure 3.3: The Flow Loop



$$\tau_k = \left[\frac{\nu_L}{\varepsilon}\right]^{\frac{1}{2}} \tag{3.1}$$

The maximum value of dissipation of turbulent kinetic energy is used to calculate the smallest time scale. The value of this variable is not easily measured so it is estimated by the simulations.

The particle time scale is calculated as recommended by Buchave et al. [60].

$$\tau = \frac{d_p^2}{36\nu_L}\left[2\frac{\rho_{particle}}{\rho_{fluid}} + 1\right] \tag{3.2}$$

For the 100 the $\mu$m polystyrene particles ($\rho_{particle} \approx 1.03$ g/cm$^3$) used in this study, the Buchave time scale is within the Kolmogorov requirement.

A sheet of light is produced by directing the beam of a 15 mW Helium Neon Laser (Spectra Physics Model 120) into a 9.5 mm diameter glass rod. As the particles enter this plane of light, the flow field is observed as streaks of light which are photographed. A sketch of the apparatus is shown in Figure 3.4).

The second procedure is laser induced fluorescence. In this technique, a soluble fluorescing dye is injected in the entrance of the cavity. The dye must be soluble in the working fluid and it must not be visible under normal lighting. However, the dye may be excited as it comes into contact with certain types of light. A sheet of laser light is produced to fluoresce the dye in planes of interest. In the present work, a saturated solution of fluorescein and distilled water is injected at the entrance of the inlet developing length. The sheet of light is created by directing the beam of a 15 mW Argon Ion laser (Toshiba) into a rotating mirror. A sketch of the apparatus is shown in Figure 3.5).



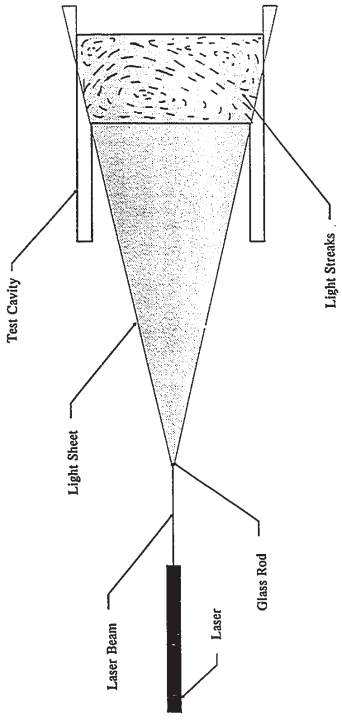


Figure 3.4: Particle Streak Flow Visualization

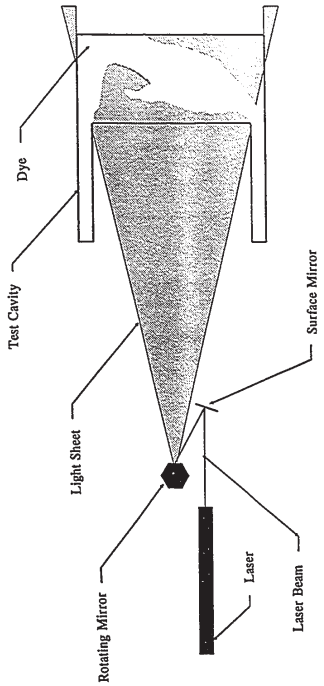


Figure 3.5: Laser Induced Fluorescence Flow Visualization



### 3.4 Velocity Measurement

The laser doppler anemometer (LDA) is used to qualitatively study the flow in the cavity. A brief description of the theory is presented in section 3.4.1. A complete discussion of the theory and method of the LDA is presented in reference [58]. A description of the LDA apparatus is presented in section 3.4.2 and a discussion of the counter processor is found in section 3.4.3.

#### 3.4.1 Theory of Laser Doppler Anemometry

Laser doppler anemometry is an optical technique used for the measurement of velocity. This technique has many advantages as discussed in section 3.1.

The LDA technique requires a highly focused monochromatic beam of light. A laser is an ideal light source as it satisfies three requirements

(i) it is monochromatic,

(ii) it is coherent, and

(iii) it is collimated.

Two beams of equal intensity polarized laser light are focused at the measuring volume to be examined. The superposition principle of waves states that the net intensity of light is the algebraic sum of the intensity of each light wave. Thus where the intensity of each beam is maximum, the net intensity is maximum (a light band). Conversely, where the intensity of light of each beam is minimum the net intensity will be minimum (a dark band). This interference may be thought to result in fringes which are stationary in space. The spacing of these fringes is constant and is a function of the light wavelength and the focusing lens half angle. The fringe spacing is calculated by



$$d_f = \frac{\lambda}{2\sin\Theta} \tag{3.3}$$

where $\lambda$ is the light wavelength and $\Theta$ is the half angle between the beams.

As the fluid moves through the measurement volume it carries seeding particles at the same velocity. A photomultiplier detects the frequency of scattered light. This doppler frequency is related to the particle velocity normal to the fringes and the fringe spacing by

$$f_D = \frac{V_{particle}}{d_f} \tag{3.4}$$

Since the fringes are stationary in space, only the magnitude of velocity can be determined as the doppler frequency is independent of direction. Frequency shifting one of the beams results in the fringes moving with a velocity proportional to the frequency shift. The flow direction can be determined with this technique. Thus, for a given velocity magnitude, a particle moving in the same direction of the fringes will create a lower doppler frequency than a particle moving in the opposite direction.

#### 3.4.2 Laser Doppler Apparatus

The Laser Doppler Anemometer (LDA) determines the velocity at a small measuring volume by detecting the Doppler shift of light scattered from a moving particle.

A single component LDA system is used to measure the velocity and turbulence fields in the cavity. A Dantec 55X LDA system operating in forward scatter mode is used for the velocity measurements. A block diagram of the LDA apparatus is shown in Figure 3.6. A 35 mW Helium Neon laser (Spectra Physics model 127) of wavelength 632 nm, provides the light source for the LDA. The beam is polarized and split into two beams 35.05 mm apart. A Bragg



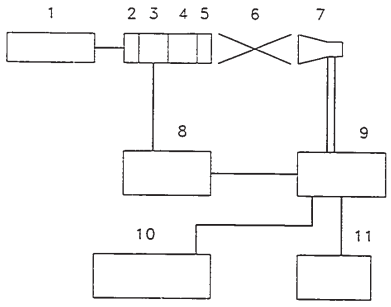


1 Laser
2 Polarization Lens
3 Bragg Cell
4 Beam Expander
5 Transmitting Lens
6 Measurement Volume
7 Receiving Lens and Photomultiplier
8 Frequency Selector
9 Photomultiplier Supply and Counter
10 Computer
11 Oscilloscope

Figure 3.6: LDA Components

cell is used to shift the frequency of one of the beams to allow direction discrimination. The last component of the transmitting optics is a focusing lens with a focal length of 80 mm. The entire transmitting optics can be rotated to measure the desired component of velocity. The measurement volume is located at the intersection of these beams. The receiving optics consist of receiving lens of focal length 80 mm and a photomultiplier to convert the light signal to a voltage. This voltage is analyzed in a Dantec 55L90 LDA Counter Processor.

### 3.4.3 Counter Processor

The counter processor determines the time in which a particle crosses a known number of fringes. The time and distance give an instantaneous velocity of the particle.

The signal which arrives at the processor contains the Doppler burst, a low frequency Doppler pedestal, and noise. Filters are used to remove the background noise (high and low pass) and the Doppler pedestal (low pass).

Once the undesirable frequencies are removed from the signal, the signal is amplified and triggers a Schmitt trigger. The output of the Schmitt trigger is fed to two counters. The first timer determines the time required for a particle to pass through 5 fringes (low count) while the other timer determines the time required for the particle to pass through 8 fringes (high count). The results of the high count and low count are compared. If the results are within a specified comparator accuracy they are considered valid and are stored. Otherwise the results are considered invalid.



## 3.4 Temperature Measurement

In the present work, three temperatures are measured as shown in Figure 3.3. These include the inlet and outlet temperatures (T1 and T2 respectively) and the temperature distribution in the cavity (T3).

The inlet and outlet temperatures are measured with a 3.2 mm thermocouple probe assembly (Chromel/Alumel with stainless steel sheath). In the case of the inlet temperature, the thermocouple is placed at the inlet of the flow development length as shown in Figure 3.3. For the outlet, it is placed at the exit of the flow development length. These thermocouple signals are monitored with a digital readout. The heat transfer to the fluid may be calculated using these temperatures and the mass flowrate of the fluid. This may be compared to the energy input from the heaters which will give an overall energy balance of the cavity.

As previously mentioned, the thermocouples in the cavity must give good accuracy, spatial resolution, and frequency response. In addition, the probe must disturb the flow as little as possible and the thermocouple must have a reasonable life. In a recent study [41], the temperature field in a cavity heated by natural convection was obtained. In this study, 0.001 inch and 0.003 inch copper/constantan and chromel/alumel thermocouples were considered. The results of the tests concluded that there were no significant differences in the measured temperatures using either size thermocouples. However, the copper/constantan thermocouples deteriorated over time in a water environment. Thus 0.003 inch chromel/alumel thermocouples are used for measuring the temperature field. The voltage to temperature conversions, the frequency of sampling and the sampling period are accomplished by way of Labtech Notebook software.

Two types of probes have been used in the present work. The horizontal temperature profile adjacent to the heated wall is measured using a 1.3 mm stainless steel probe. These



probes enter the cavity horizontally at three locations in the vertical wall opposite the heated wall. The fine wire thermocouples extend out of the end of the probes approximately 9 mm. The probe can be moved horizontally and is located with a dial indicator. The vertical temperature profiles are measured with an "L" shaped probe. The probe enters the cavity from the top and can be moved in the vertical direction. This vertical leg of the probe is constructed from 0.125 stainless steel tubing and the horizontal leg is constructed from 3.2 mm acrylic to reduce conduction near the measurement location. Four thermocouples run down through the vertical leg and adjacent to the horizontal leg. At four different distances from the heated wall a thermocouple extends from the probe approximately 9 mm.

# CHAPTER 4

# EXPERIMENTAL PROCEDURE

## 4.1 Introduction

Approximately three to four hours is required for the system to reach steady state. Velocity measurements required approximately two weeks of data collection for each case considered. To obtain the same flow and temperature fields, each day the velocity and temperature boundary conditions had to be nearly identical. As a result, a set of general operating procedures are required to be followed. A summary of these procedures is presented. Refer to Figure 3.3 for a schematic of the flow loop.

(1) Turn on the cold tap water to the heat exchanger. Allow the warm water in the building piping system to purge.

(2) Turn on the pump and adjust the flow control valve to the required flowrate.

(3) Turn on the wall heaters and coarsely adjust the electrical input. Allow the system to stabilize for approximately 10 minutes.

(4) Repeat step 3 until the wall temperatures are near the required temperatures.

(5) Adjust the cold water flowrate into the heat exchanger to obtain the required inlet temperature.

(6) Finely adjust the power to each of the heaters until the required wall temperature is achieved.

(7) Finely adjust the flow control valve to the required flowrate.

(8) Go to step 5 until the required thermal and velocity boundary conditions are established.

(9) Leave the system for approximately three hours to allow the system to attain steady state.

In the above adjustments, the wall temperature was considered uniform when the difference between the maximum and minimum measured temperatures was less than 0.5°C.

A summary of the specific procedures for flow visualization, velocity measurement and temperature measurements is presented in this chapter.

### 4.2 Flow Visualization

The results of the flow visualization studies were recorded on a Nikon FE2 35 mm camera and a Sony V9 camcorder. An array of film types, shutter speeds, and fstop values were tested to obtain optimal results. More specifically, Kodak Kodachrome 100, 200 and 400 ASA and Ektachrome 1600 ASA film were tested using an f-stop of 2.8 and 5.6 and shutter opening of ½, 1, 2 and 4 seconds. Preliminary tests suggested that Ektachrome 1600 ASA film with an f-stop of 2.8 and a shutter openings of either 2 or 4 seconds yielded optimal results.

### 4.3 Velocity Measurements

The test cavity was mounted on a xyz traversing table. The x and z traverses are Daedal traverses with a repeatability of 0.004 μm/mm. The y traverse (Thompson) is capable of supporting a higher load but only has a repeatability of 16 μm/mm. A MC5000 controller board and PC21 controller code is used for control of the traversing table.

The diameter and length of the measurement volume are given by



$$d_m = \frac{4F_A\lambda}{\pi D_{e^{-2}}} \qquad l_m = \frac{d_m}{\tan\Theta} \tag{4.1}$$

where $F_A$ is the apparent focal length,

$\lambda$ is the laser light wavelength,

$D_{e-2}$ is the diameter of the laser beam, and

$\Theta$ is the half angle of intersection

For the present setup, the diameter and length of the measurement probe are calculated to be 0.053 mm and 0.245 mm respectively. The fringe spacing is calculated to be 1.48 μm.

The counter processor settings are summarized in Table 4.1

**Table 4.1: Counter Processor Settings**

| | |
|---|---|
| Frequency Shift | 1000 kHz |
| Comparator Accuracy | 3% |
| Low Pass Filter | 2 MHz |
| High Pass Filter | 256 kHz |

The quality of the velocity data can be estimated from indicators on the counter processor. The rate of validated data is reflected by the data rate. This parameter varied from a low of .3 kHz to a high of 5 kHz. The region adjacent to the heated wall suffered from low data rates as the changes in temperature in this region change the index of refraction of water. The data rate for the majority of the work fell between 1 kHz and 3 kHz. The percentage of



validated data, or validation rate, is the second important parameter. This parameter rarely fell below 60% and was typically above 80%. Again the validation rate was low in the region of the heated wall. Edwards [61] criteria suggests that this is an intermediate data density.

For each of the cases considered, two components of velocity (u and v) are measured in various planes. All references to x, y and z are based on the coordinate system defined in Figure 3.1. The velocity components u, v and w correspond the coordinates x, y and z respectively.

A summary of the location of the velocity measurements is presented in Tables 4.2 to 4.6. The entire flow field was measured in the plane of symmetry (z = 0). The flow field in this plane shows the overall "two-dimensional" results in the cavity. These velocities were measured on a 19 by 29 rectangular grid. The specific x and y grid locations are summarized in Table 4.2

**Table 4.2: Velocity Measurement Locations in the Plane of Symmetry**

| Location | x (mm) | y (mm) | | Location | x (mm) | y (mm) | | Location | y (mm) |
|---|---|---|---|---|---|---|---|---|---|
| 1 | 8 | 2 | | 11 | 128 | 70 | | 21 | 265 |
| 2 | 18 | 3 | | 12 | 133 | 90 | | 22 | 275 |
| 3 | 28 | 4 | | 13 | 138 | 110 | | 23 | 280 |
| 4 | 48 | 6 | | 14 | 140 | 130 | | 24 | 283 |
| 5 | 68 | 9 | | 15 | 142 | 147 | | 25 | 286 |
| 6 | 88 | 12 | | 16 | 143 | 165 | | 26 | 289 |
| 7 | 98 | 15 | | 17 | 144 | 185 | | 27 | 291 |
| 8 | 108 | 20 | | 18 | 145 | 205 | | 28 | 292 |
| 9 | 118 | 30 | | 19 | 146 | 225 | | 29 | 293 |
| 10 | 123 | 50 | | 20 | | 245 | | | |



In addition to the entire flow field, areas of specific interest are studied in more detail. These include the separation region adjacent to the heated wall and the exit flow. The exit region gives an indication of the exit boundary conditions required for the numerical modelling. For both the exit region and the separation region, measurements were obtained on a 7 by 7 grid. The specific grid for the separation and exit regions are shown in Tables 4.3 and 4.4 respectively. In Table 4.3, the coordinate, $\gamma$, is the distance from the separation height and is defined as

$$\gamma = y - y_{sep} \tag{4.2}$$

**Table 4.3: Velocity Measurement Locations in the Separation Region**

| Location | x(mm) | γ(mm) |
|---|---|---|
| 1 | 133 | -9 |
| 2 | 136 | -6 |
| 3 | 139 | -3 |
| 4 | 142 | 0 |
| 5 | 144 | 3 |
| 6 | 145 | 6 |
| 7 | 147 | 9 |

Table 4.4: Velocity Measurement Locations in the Exit Region

| Location | x(mm) | y(mm) |
|---|---|---|
| 1 | 8 | 2 |
| 2 | 11 | 5 |
| 3 | 14 | 8 |
| 4 | 17 | 11 |
| 5 | 20 | 14 |
| 6 | 23 | 17 |
| 7 | 26 | 20 |

The three-dimensionality of the flow is also studied by obtaining measurements in planes perpendicular to the plane of symmetry. The inlet and outlet jets are studied by taking measurements in the y = 293 mm and y = 4 mm planes respectively. The coordinates of these velocity measurements are shown in Table 4.5. In addition, the two-dimensionality in the region of the heated wall is studied by obtaining velocity measurements in a plane 4 mm from this boundary. The locations of these velocity measurements are shown in Table 4.6.

Table 4.5: Velocity Measurement Locations in the Inlet and Outlet Planes

| Location | x(mm) | z(mm) |
|---|---|---|
| 1 | 18.5 | -20 |
| 2 | 38.5 | -13.3 |
| 3 | 58.5 | -6.67 |
| 4 | 78.5 | 0 |
| 5 | 98.5 | 6.67 |
| 6 | 118.5 | 13.3 |
| 7 | 138.5 | 20 |



Table 4.6: Velocity Measurement Locations Adjacent to the Heated Wall

| Location | y(mm) | z(mm) |
|---|---|---|
| 1 | 10 | -20 |
| 2 | 30 | -13.3 |
| 3 | 50 | -6.67 |
| 4 | 70 | 0 |
| 5 | 90 | 6.67 |
| 6 | 110 | 13.3 |
| 7 | 130 | 20 |
| 8 | 148 | |
| 9 | 167 | |
| 10 | 187 | |
| 11 | 207 | |
| 12 | 227 | |
| 13 | 247 | |
| 14 | 267 | |
| 15 | 287 | |

### 4.4 Temperature Measurements

The horizontal temperature profiles were measured at 80, 140 and 200 mm heights. The 140 and 200 mm heights correspond to the separation height in two of the cases considered. The location of the temperature measurements is given in Table 4.7. The variable, $\eta$, is defined as the distance from the heated wall. The zero location is defined as the point at which no temperature increase is found by bringing the thermocouple closer to the wall. Labtech Notebook software is used for data acquisition. Initial analysis of the flow field suggested that a sampling



period of 200 seconds is required to compute the average temperature. The sampling frequency is 10 Hz.

The vertical temperature profiles are measured at 2, 4, 10 and 75 mm from the heated wall. The temperatures are measured in 1.5 cm increments from a height of 1.5 to 28.5 cm. The same sampling frequency and data rate are used for the vertical profiles.

Table 4.7: Horizontal Temperature Measurement Locations

| Location | $\eta$(mm) | | Location | $\eta$(mm) |
|---|---|---|---|---|
| 1 | 0 | | 13 | 4.5 |
| 2 | 0.1 | | 14 | 5.1 |
| 3 | 0.2 | | 15 | 6.4 |
| 4 | 0.3 | | 16 | 7.6 |
| 5 | 0.6 | | 17 | 10.2 |
| 6 | 0.9 | | 18 | 12.7 |
| 7 | 1.3 | | 19 | 17.8 |
| 8 | 1.7 | | 20 | 25.4 |
| 9 | 2.0 | | 21 | 38.1 |
| 10 | 2.5 | | 22 | 50.8 |
| 11 | 3.2 | | 23 | 63.5 |
| 12 | 3.8 | | 24 | 76.2 |

## CHAPTER 5

## MATHEMATICAL FORMULATION

### 5.1 Introduction

The conservation equations that govern the velocity, temperature and turbulence fields in the cavity are presented in section 5.2 while the boundary conditions are presented in section 5.3. The conservation equations are written in terms of primitive variables and diffusion terms are in the fully conservative form. The following assumptions have been made

(i) the flow in the cavity is two-dimensional,

(ii) the fluid is Newtonian,

(iii) temperature change due to viscous dissipation is negligible, and

(iv) the density of the fluid is considered constant except in the buoyancy force term. This approximation is commonly referred to as the Boussinesq approximation [62] and the validity of this assumption will be considered in Chapter 7.

### 5.2 Governing Equations

#### 5.2.1 Dimensional Governing Equations

The instantaneous form of the governing equations are used to predict laminar flow in the cavity. The continuity, x-momentum, y-momentum and energy equations are

*Continuity*

$$\frac{\partial u}{\partial x} + \frac{\partial v}{\partial y} = 0 \qquad (5.1)$$

*X-Momentum*

$$\frac{\partial u}{\partial t} + u\frac{\partial u}{\partial x} + v\frac{\partial u}{\partial y} = -\frac{1}{\rho}\frac{\partial p}{\partial x} + \frac{\partial}{\partial y}\left[\nu_L \frac{\partial u}{\partial x}\right] + \frac{\partial}{\partial y}\left[\nu_L \frac{\partial u}{\partial y}\right] + g_x\beta(T - T_R) \quad (5.2)$$

*Y-Momentum*

$$\frac{\partial v}{\partial t} + u\frac{\partial v}{\partial x} + v\frac{\partial v}{\partial y} = -\frac{1}{\rho}\frac{\partial p}{\partial y} + \frac{\partial}{\partial x}\left[\nu_L \frac{\partial v}{\partial x}\right] + \frac{\partial}{\partial y}\left[\nu_L \frac{\partial v}{\partial y}\right] + g_y\beta(T - T_R) \quad (5.3)$$

*Energy*

$$\frac{\partial T}{\partial t} + u\frac{\partial T}{\partial x} + v\frac{\partial T}{\partial y} = \alpha_L\left[\frac{\partial^2 T}{\partial x^2} + \frac{\partial^2 T}{\partial y^2}\right] \quad (5.4)$$

For the Boussinesq approximation (used in equations (5.2) and (5.3)), the thermophysical properties are computed at the reference temperature given by

$$T_R = \frac{(T_W + T_J)}{2} \quad (5.5)$$

The equations used to compute the thermophysical properties are cited by Giel [41] and are presented in section 5.4 of the present work.

The governing equations for turbulent flow are based on the low Reynolds number, k-ε, turbulence model. The momentum equation is obtained by substituting equation (2.15) for the turbulent Reynolds stress into the time-averaged versions of equations (5.2) and (5.3) while the energy equation is obtained by substituting equation (2.18) for the turbulent heat flux into the time-averaged form of equation (5.4). The conservation equations for turbulent flow in cartesian coordinates are then:

*Continuity*

$$\frac{\partial u}{\partial x} + \frac{\partial v}{\partial y} = 0 \quad (5.6)$$



*X-Momentum*

$$\frac{\partial u}{\partial t} + u\frac{\partial u}{\partial x} + v\frac{\partial u}{\partial y} = -\frac{1}{\rho}\frac{\partial p}{\partial x} + \frac{\partial}{\partial x}\left[(\nu_L + \nu_T)\frac{\partial u}{\partial x}\right] + \frac{\partial}{\partial y}\left[(\nu_L + \nu_T)\frac{\partial u}{\partial y}\right] + \frac{\partial}{\partial x}\left[(\nu_L + \nu_T)\frac{\partial u}{\partial x}\right] + \frac{\partial}{\partial y}\left[(\nu_L + \nu_T)\frac{\partial v}{\partial x}\right] + g_x\beta(T - T_R) - \frac{2}{3}\frac{\partial k}{\partial x} \quad (5.7)$$

*Y-Momentum*

$$\frac{\partial v}{\partial t} + u\frac{\partial v}{\partial x} + v\frac{\partial v}{\partial y} = -\frac{1}{\rho}\frac{\partial p}{\partial y} + \frac{\partial}{\partial x}\left[(\nu_L + \nu_T)\frac{\partial v}{\partial x}\right] + \frac{\partial}{\partial y}\left[(\nu_L + \nu_T)\frac{\partial v}{\partial y}\right] + \frac{\partial}{\partial x}\left[(\nu_L + \nu_T)\frac{\partial u}{\partial y}\right] + \frac{\partial}{\partial y}\left[(\nu_L + \nu_T)\frac{\partial v}{\partial y}\right] + g_y\beta(T - T_R) - \frac{2}{3}\frac{\partial k}{\partial y} \quad (5.8)$$

where the turbulent dynamic viscosity, $\nu_T$, is

$$\nu_T = C_\mu f_\mu \frac{k^2}{\varepsilon} \quad (5.9)$$

*Energy*

$$\frac{\partial T}{\partial t} + u\frac{\partial T}{\partial x} + v\frac{\partial T}{\partial y} = \frac{\partial}{\partial x}\left[(\alpha_L + \alpha_T)\frac{\partial T}{\partial x}\right] + \frac{\partial}{\partial y}\left[(\alpha_L + \alpha_T)\frac{\partial T}{\partial y}\right] \quad (5.10)$$

where the turbulent thermal diffusivity, $\alpha_T$, is

$$\alpha_T = \frac{\nu_T}{\sigma_T} \quad (5.11)$$

*Turbulent Kinetic Energy*

$$\frac{\partial k}{\partial t} + u\frac{\partial k}{\partial x} + v\frac{\partial k}{\partial y} = \frac{\partial}{\partial x}\left[\left(\nu_L + \frac{\nu_T}{\sigma_k}\right)\frac{\partial k}{\partial x}\right] + \frac{\partial}{\partial y}\left[\left(\nu_L + \frac{\nu_T}{\sigma_k}\right)\frac{\partial k}{\partial y}\right] + G - \bar{\varepsilon} - g_x\beta\frac{\nu_T}{\sigma_T}\frac{\partial T}{\partial x} - g_y\beta\frac{\nu_T}{\sigma_T}\frac{\partial T}{\partial y} - D \quad (5.12)$$



*Rate of Dissipation of Kinetic Energy*

$$\frac{\partial \bar{\varepsilon}}{\partial t} + u\frac{\partial \bar{\varepsilon}}{\partial x} + v\frac{\partial \bar{\varepsilon}}{\partial y} = \frac{\partial}{\partial x}\left[\left(\nu_L + \frac{\nu_T}{\sigma_\varepsilon}\right)\frac{\partial \bar{\varepsilon}}{\partial x}\right] + \frac{\partial}{\partial y}\left[\left(\nu_L + \frac{\nu_T}{\sigma_\varepsilon}\right)\frac{\partial \bar{\varepsilon}}{\partial y}\right] + C_1 f_1 \frac{\bar{\varepsilon}}{k} G - C_2 f_2 \frac{\bar{\varepsilon}^2}{k} - C_3 f_3 g_x \beta \frac{\bar{\varepsilon}}{k}\frac{\nu_T}{\sigma_T}\frac{\partial T}{\partial x} - C_3 f_3 g_y \beta \frac{\bar{\varepsilon}}{k}\frac{\nu_T}{\sigma_T}\frac{\partial T}{\partial y} + \hat{E} \quad (5.13)$$

where the generation of turbulence, G, is

$$G = \nu_T\left[2\left[\frac{\partial u}{\partial x}\right]^2 + 2\left[\frac{\partial v}{\partial y}\right]^2 + \left[\frac{\partial u}{\partial y} + \frac{\partial v}{\partial x}\right]^2\right] \quad (5.14)$$

The terms Ð and Ê, in equations 5.12 and 5.13 respectively, are used for low Reynolds number modelling as discussed in section 2.4.2.

### 5.2.2 Dimensionless Variables

The governing equations may be cast in terms of the relevant dimensionless parameters described in section 2.1. This may be accomplished by non-dimensionalizing the variables as follows

*Dimensionless Coordinate*

$$X = \frac{x}{H} \qquad Y = \frac{y}{H} \quad (5.15)$$

where H, is the height of the enclosure.

*Dimensionless Velocity*

$$U = \frac{u}{u_J} \qquad V = \frac{v}{u_J} \quad (5.16)$$



where $u_j$, is the volumetric averaged inlet jet velocity.

*Dimensionless Temperature*

$$\theta = \frac{(T - T_J)}{(T_W - T_J)} \quad (5.17)$$

*Dimensionless Pressure*

$$P = \frac{p}{\rho u_J^2} \quad (5.18)$$

*Dimensionless Turbulent Kinetic Energy*

$$k^* = \frac{k}{u_J^2} \quad (5.19)$$

*Dimensionless Dissipation of Turbulent Kinetic Energy*

$$\varepsilon^* = \frac{\varepsilon H}{u_J^3} \quad (5.20)$$

### 5.2.3 Dimensionless Governing Equations

The non-dimensional form of the governing equations used to predict laminar flow in the cavity are

*Dimensionless Continuity*

$$\frac{\partial U}{\partial Y} + \frac{\partial V}{\partial Y} = 0 \quad (5.21)$$

*Dimensionless X-Momentum*

$$U\frac{\partial U}{\partial X} + V\frac{\partial U}{\partial Y} = -\frac{\partial P}{\partial X} + \frac{\partial}{\partial X}\left[\frac{a}{Re_L}\frac{\partial U}{\partial X}\right] + \frac{\partial}{\partial Y}\left[\frac{a}{Re_L}\frac{\partial U}{\partial Y}\right] + \frac{Gr_x a^2}{Re_L^2}\theta \qquad (5.22)$$

*Dimensionless Y-Momentum*

$$U\frac{\partial V}{\partial X} + V\frac{\partial V}{\partial Y} = -\frac{\partial P}{\partial Y} + \frac{\partial}{\partial X}\left[\frac{a}{Re_L}\frac{\partial V}{\partial X}\right] + \frac{\partial}{\partial Y}\left[\frac{a}{Re_L}\frac{\partial V}{\partial Y}\right] + \frac{Gr_y a^2}{Re_L^2}\theta \qquad (5.23)$$

*Dimensionless Energy*

$$U\frac{\partial \theta}{\partial X} + V\frac{\partial \theta}{\partial Y} = \frac{\partial}{\partial X}\left[\frac{a}{Re_L Pr_L}\frac{\partial \theta}{\partial X}\right] + \frac{\partial}{\partial Y}\left[\frac{a}{Re_L Pr_L}\frac{\partial \theta}{\partial Y}\right] \qquad (5.24)$$

In these equations the dimensionless parameters $Pr_L$, a, $Re_L$ and Gr are defined by equations 2.1, 2.2, 2.4 and 2.5 respectively. The subscript, L, refers to the dimensionless parameter based on the laminar properties. The temperatures at which these properties are computed are discussed in section 5.4.

The non-dimensional conservation equations for turbulent flow in cartesian coordinates are then:

*Dimensionless Continuity*

$$\frac{\partial U}{\partial X} + \frac{\partial V}{\partial Y} = 0 \qquad (5.25)$$



*Dimensionless X-Momentum*

$$U\frac{\partial U}{\partial X} + V\frac{\partial U}{\partial Y} = -\frac{\partial P}{\partial X} + \frac{\partial}{\partial X}\left[\left[\frac{a}{Re_L} + \frac{a}{Re_T}\right]\frac{\partial U}{\partial X}\right] + \frac{\partial}{\partial Y}\left[\left[\frac{a}{Re_L} + \frac{a}{Re_T}\right]\frac{\partial U}{\partial Y}\right] + \frac{\partial}{\partial X}\left[\left[\frac{a}{Re_L} + \frac{a}{Re_T}\right]\frac{\partial U}{\partial X}\right] + \frac{\partial}{\partial Y}\left[\left[\frac{a}{Re_L} + \frac{a}{Re_T}\right]\frac{\partial V}{\partial X}\right] + \frac{Gr_x a^2}{Re_L^2}\theta - \frac{2}{3}\frac{\partial k^*}{\partial X} \qquad (5.26)$$

*Dimensionless Y-Momentum*

$$U\frac{\partial V}{\partial X} + V\frac{\partial V}{\partial Y} = -\frac{\partial P}{\partial Y} + \frac{\partial}{\partial X}\left[\left[\frac{a}{Re_L} + \frac{a}{Re_T}\right]\frac{\partial V}{\partial X}\right] + \frac{\partial}{\partial Y}\left[\left[\frac{a}{Re_L} + \frac{a}{Re_T}\right]\frac{\partial V}{\partial Y}\right] + \frac{\partial}{\partial X}\left[\left[\frac{a}{Re_L} + \frac{a}{Re_T}\right]\frac{\partial U}{\partial Y}\right] + \frac{\partial}{\partial Y}\left[\left[\frac{a}{Re_L} + \frac{a}{Re_T}\right]\frac{\partial V}{\partial Y}\right] + \frac{Gr_y a^2}{Re_L^2}\theta - \frac{2}{3}\frac{\partial k^*}{\partial Y} \qquad (5.27)$$

where the Reynolds number based on turbulent viscosity, $Re_T$, is

$$Re_T = \frac{u_J D}{\nu_T} = \frac{a\,\bar{\varepsilon}^*}{f_\mu C_\mu k^{*2}} \qquad (5.28)$$

*Dimensionless Energy*

$$U\frac{\partial \theta}{\partial X} + V\frac{\partial \theta}{\partial Y} = \frac{\partial}{\partial X}\left[\left[\frac{a}{Re_L Pr_L} + \frac{a}{Re_T \sigma_T}\right]\frac{\partial \theta}{\partial X}\right] + \frac{\partial}{\partial Y}\left[\left[\frac{a}{Re_L Pr_L} + \frac{a}{Re_T \sigma_T}\right]\frac{\partial \theta}{\partial Y}\right] \qquad (5.29)$$



*Dimensionless Turbulent Kinetic Energy*

$$U\frac{\partial k^*}{\partial X} + V\frac{\partial k^*}{\partial Y} = \frac{\partial}{\partial X}\left[\left[\frac{a}{Re_L} + \frac{a}{\sigma_k Re_T}\right]\frac{\partial k^*}{\partial X}\right] + \frac{\partial}{\partial Y}\left[\left[\frac{a}{Re_L} + \frac{a}{\sigma_k Re_T}\right]\frac{\partial k^*}{\partial Y}\right] + G^* - \bar{\varepsilon}^* - \frac{a^3 (Gr_x)_T}{\sigma_T Re_T^3}\frac{\partial \theta}{\partial X} - \frac{a^3 (Gr_y)_T}{\sigma_T Re_T^3}\frac{\partial \theta}{\partial Y} - D^* \qquad (5.30)$$

*Dimensionless Rate of Dissipation of Kinetic Energy*

$$U\frac{\partial \bar{\varepsilon}^*}{\partial X} + V\frac{\partial \bar{\varepsilon}^*}{\partial Y} = \frac{\partial}{\partial X}\left[\left[\frac{a}{Re} + \frac{a}{\sigma_\varepsilon Re_T}\right]\frac{\partial \bar{\varepsilon}^*}{\partial X}\right] + \frac{\partial}{\partial Y}\left[\left[\frac{a}{Re} + \frac{a}{\sigma_\varepsilon Re_T}\right]\frac{\partial \bar{\varepsilon}^*}{\partial Y}\right] + C_y f_1 \frac{\bar{\varepsilon}^*}{k^*} G^* - C_y f_2 \frac{\bar{\varepsilon}^{*2}}{k^*} - C_y f_3 \frac{\bar{\varepsilon}^*}{k^*}\frac{a^3 (Gr_x)_T}{\sigma_T Re_T^3}\frac{\partial \theta}{\partial X} - C_y f_3 \frac{\bar{\varepsilon}^*}{k^*}\frac{a^3 (Gr_y)_T}{\sigma_T Re_T^3}\frac{\partial \theta}{\partial X} + E^* \qquad (5.31)$$

where the generation of turbulence, $G^*$, is

$$G^* = \frac{a}{Re_T}\left[2\left[\frac{\partial U}{\partial X}\right]^2 + 2\left[\frac{\partial V}{\partial Y}\right]^2 + \left[\frac{\partial U}{\partial Y} + \frac{\partial V}{\partial X}\right]^2\right] \qquad (5.32)$$

and the Grashof number based on turbulent viscosity is

$$(Gr_i)_T = \frac{g_i \beta (T_w - T_j) H^3}{\nu_T^3} \qquad (5.33)$$



## 5.3 Boundary Conditions

### 5.3.1 Laminar Flow

For the present laminar case studies, the program simulates a variety of velocity and temperature boundary conditions. These include the following boundary conditions: no slip walls, inflow, outflow, adiabatic and isothermal temperature. As an example, for the lower horizontal wall in a cavity these boundary conditions are formulated as follows:

*No Slip Wall:*

The no-slip boundary condition is set by prescribing both the U and V velocity to be zero at the wall.

$$U|_{y=0} = 0$$
$$V|_{y=0} = 0 \qquad (5.34)$$

*Adiabatic Wall:*

The adiabatic boundary condition is set by specifying the temperature gradient such that the heat flux is zero at the wall.

$$\left.\frac{\partial \theta}{\partial Y}\right|_{y=0} = 0 \qquad (5.35)$$

*Isothermal Wall*

The isothermal wall boundary condition is set by specifying the wall temperature.

$$\theta|_{y=0} = \theta_W \qquad (5.36)$$

*Outflow Boundary*

The outflow boundary condition is set by specifying the tangential velocity to zero and the gradient of all remaining variables to be zero at the wall.

$$U_{Tang}\big]_{y=0} \quad \text{and} \quad \left.\frac{\partial \phi}{\partial Y}\right|_{y=0} = 0 \tag{5.37}$$

*Inflow Boundary*

The inflow boundary condition is set by specifying the normal velocity to have a specified velocity, a parabolic profile or a one seventh power law profile. The tangential velocity is set to zero while the scalar variables are set to a specified value.

### 5.3.2 Turbulent Flow

The boundary conditions for turbulent flow are imposed in the same manner as the laminar flow case. In addition to this, the equations governing turbulent flow (equations 5.26 to 5.33) must account for the viscous effects in the vicinity of the walls. As previously mentioned in the literature review these equations are valid only for fully turbulent flow. Thus the governing equations must either be modified or additional theory must be introduced. The low Reynolds number methods employed in the present work are Giel's [41] modification to the Jones and Launder model [38] and Davidson's [42] modification of the Lam and Bremhorst model [39]. The boundary condition for the turbulent kinetic energy next to a solid boundary is

$$k^*|_{y=0} = 0 \tag{5.38}$$

For an inflow boundary, the turbulent kinetic energy is computed from equation (2.46) and is defined as



$$k_{in}^* = \frac{3}{2}\psi^2 \overline{U_j}^2 \tag{5.39}$$

This inlet kinetic energy is based on the turbulent intensity, $\psi$ (taken to be 10%) and the mean volumetric velocity of the inlet, $\overline{U_j}$. The inlet dissipation of kinetic energy is calculated from

$$\varepsilon_{in}^* = C_\mu^{3/4}\frac{k_{in}^{*3/2}}{l} \tag{5.40}$$

The length scale, $l$ is equal to 0.007 times an equivalent radius based on the area of the inlet. This method is based on turbulent flow in a pipe and has been used in a commercial computational fluid dynamics program [63]. The solution was relatively insensitive to the inlet turbulent kinetic energy and dissipation. This insensitivity is consistent with other researchers [4,6,59].

The Jones and Launder low Reynolds number model [38] has been modified as described by Giel [41]. A summary of the dimensionless form follows. The modified Lam and Bremhorst model (see Table 2.2) may be nondimensionalized in a similar manner. The "f" functions or damping coefficients in equation (5.31) are shown in equations (5.41-5.44)

$$f_\mu = \exp\left[\frac{-2.5}{1 + Re_t/50}\right] \tag{5.41}$$

$$f_1 = 1. \tag{5.42}$$

$$f_2 = [1. - 0.3\exp(-Re_t^2)] \tag{5.43}$$



$$f_3 = 1. \tag{5.44}$$

where the turbulent Reynolds number, $Re_t$ is

$$Re_t = \frac{Re_L\, k^{*2}}{a\,\bar{\varepsilon}^*} \tag{5.45}$$

The extra term in the turbulent kinetic energy equation (equation 5.30) is given by

$$D^* = -2\frac{a}{Re_L}\left[\left(\frac{\partial k^{*1/2}}{\partial X}\right)^2 + \left(\frac{\partial k^{*1/2}}{\partial Y}\right)^2\right] \tag{5.46}$$

The advantage of using this extra term in the kinetic energy equation is that it allows the dissipation to be set to zero at the boundaries.

$$\bar{\varepsilon}^*|_{y=0} = 0 \tag{5.47}$$

Jones and Launder [38] also included the extra term, $E^*$, in the dissipation equation (equation 5.31). Giel [41] cites Launder as noting that the physical justification of this term is not settled. Several researchers [41,51,64] have dropped this term. In the present work, this term has been incorporated.

$$E^* = 2\frac{a}{Re_L}\frac{a}{Re_T}\left[\left(\frac{\partial^2 U}{\partial X^2}\right)^2 + \left(\frac{\partial^2 U}{\partial Y^2}\right)^2 + \left(\frac{\partial^2 V}{\partial X^2}\right)^2 + \left(\frac{\partial^2 V}{\partial Y^2}\right)^2\right] \tag{5.48}$$



## 5.4 Calculation of Thermophysical Properties

The effect of temperature on the thermophysical properties of water has been investigated. The properties of water are given by equations (5.49) to (5.53). When the constant property model is used, the fluid properties are evaluated at the reference temperature given by equation (5.5). The Reynolds, Grashof, and Prandtl numbers used in the dimensionless governing equations are computed based on these reference properties. For the variable property model, the thermophysical properties and hence the above dimensionless parameters, are based on the local time-averaged temperature.

*Density (kg/m$^3$) [65]*

$$\rho = \frac{\rho_0 + \rho_1 T_\rho + \rho_2 T_\rho^2 + \rho_3 T_\rho^3 + \rho_4 T_\rho^4 + \rho_5 T_\rho^5}{1 + \rho_6 T_\rho}$$

where $\rho_0$ = 999.8396, $\rho_1$ = 18.224944, $\rho_2$ = -7.9221E-3, $\rho_3$ = -5.544846E-5, $\rho_4$ = 1.497562E-7, $\rho_5$ = -3.932952E-10, $\rho_6$ = 1.8159725E-2

*and* $T_\rho = T\,(^\circ C)$

maximum deviation = 0.004% at 12 °C, standard deviation = 0.002% (5.49)

*Dynamic Viscosity (kg/m s) [66]*

$$\mu = \frac{10^{-3}}{[\mu_1\{T_\mu + (T_\mu^2 + \mu_2)^{1/2}\} - \mu_3]}$$

where $\mu_0$ = 8.435, $\mu_1$ = 0.021482, $\mu_2$ = 8078.4, $\mu_3$ = 1.2

$T_\mu = T\,(^\circ C) - \mu_0$

maximum deviation = -0.51% at 98 °C, standard deviation = 0.37% (5.50)

*Thermal Conductivity (W/m K) [41]*

$$K = K_0 + K_1 T_K + K_2 T_K^2 + K_3 T_K^3 + K_4 T_K^4$$

where $K_0 = 5.8506541$ $K_1 = -20.397946$ (5.51)
$K_2 = 27.762115$ $K_3 = -16.023208$
$K_4 = 3.3692098$ $T_K = [T(°C) + 273.15]/273.15$
maximum deviation = 0.02% at 2 °C, standard deviation = 0.009%

*Specific Heat (J/kg K) [41]*

$$C_p = C_{P3}(C_{P0} + C_{P1} T_{C_p} + C_{P2} T_{C_p}^2)$$

where $C_{P0} = 1.2753249$ $C_{P1} = -1.7479235E{-}3$ (5.52)
$C_{P2} = 2.7572590E{-}6$ $C_{P3} = 4186.8$
$T_{C_p} = T(°C) + 273.15$
maximum deviation = 0.33% at 2 °C, standard deviation = 0.07%

The coefficient of thermal expansion is calculated by numerical differentiation of the density equation with respect to temperature. By definition this variable is defined by

$$\beta = -\frac{1}{\rho}\left[\frac{\partial \rho}{\partial T}\right]_p \qquad (5.53)$$

### 5.5 Variation of Turbulent Prandtl Number

Kays and Crawford [67] state the variation of turbulent Prandtl number in the boundary layer is difficult to measure accurately. However it is known that the turbulent Prandtl number is large adjacent to the boundary and decreases asymptotically to a value of about unity in the law of the wall region. This high value of turbulent Prandtl number suggests that momentum



diffusion is greater than heat diffusion adjacent to the wall. Kays and Crawford [67] compute the turbulent Prandtl number based on the turbulent Peclet number, an experimental constant, c, and the value of turbulent Prandtl number far from the wall, $\sigma_{T\infty}$.

$$\sigma_T = \frac{1}{\frac{1}{2\sigma_{T\infty}} + cPe_T\sqrt{\frac{1}{\sigma_{T\infty}} - (cPe_T)^2\left[1 - \exp\left(-\frac{1}{cPe_T\sqrt{\sigma_{T\infty}}}\right)\right]}} \qquad (5.54)$$

where

$$Pe_T = \left(\frac{\nu_T}{\nu}\right)Pr_L\,,$$
$$\sigma_{T\infty} = 0.86 \qquad (5.55)$$
$$c = 0.2$$

In the present work, the results from a constant turbulent Prandtl number model are compared with the results from the model of Kays and Crawford and will be discussed in section 7.4.4.2



# CHAPTER 6

# NUMERICAL FORMULATION

### 6.1 Introduction

The solution technique is based on the Semi-Implicit Method for Pressure Linked Equations Revised (SIMPLER) algorithm of Patankar [68,69]. A brief background of the procedure as cited by Patankar [69] follows.

In 1972, Patankar and Spalding described a calculation procedure for three-dimensional parabolic flow. A three-dimensional parabolic flow procedure contains within it a procedure for two-dimensional elliptic flows. The resulting two-dimensional procedure has been employed in many applications. The particular technique by which the pressure-velocity linkage is handled in this procedure has been given the name Semi-Implicit Method for Pressure Linked Equations (SIMPLE). Since the original development of the SIMPLE procedure, many changes in the original procedure have been incorporated. A major change was the development of SIMPLER (SIMPLE-Revised). With this procedure, a converged solution is obtained with fewer iterations. A saving of computer time of 30-50% is commonly achieved with this procedure. Thus the SIMPLER procedure has been adopted with the present work [69].

In addition to the SIMPLER scheme, many other procedures have been derived from the SIMPLE algorithm. Some of the enhancements that have been incorporated in the present computer code will be discussed later in the chapter. A description and a comparison of these enhancements may be found in the papers of Van Doormal and Raithby [70], Latimer and Pollard [71] and Jang et al. [72].



All results obtained were computed on a SUN SPARC 1+ workstation. The code was written in FORTRAN-77. A commercial graphics package (TECPLOT) has been used to display the results.

### 6.2 The Control Volume Method

The conservation equations described in Chapter 5 are solved numerically using the control volume integral approach with the SIMPLER algorithm. With this approach the calculation domain is divided into a two-dimensional array of control volume cells (see Figure 6.1) of variable dimensions $\Delta x_{ij}$ and $\Delta y_{ij}$. A non-uniform grid is incorporated in the present work to resolve the steep gradients of the dependent variables in the vicinity of the walls.

The staggered grid concept is used for locating flow variables. The velocities are located at points on the faces of the scalar control volumes while the scalar variables (P, $\Theta$, $k^*$ and $\varepsilon^*$) are located at control volume centres. If values are required at any other points in the grid they are calculated using simple linear interpolation. An advantage of the staggered grid technique is that the pressure difference between two cell centres becomes the driving force for the velocity component located between the cell centres. Another approach to describing the staggered grid concept is to consider the computational domain divided into three overlapping types of control volumes: the U velocity control volumes are staggered from the scalar volumes in the X direction while the V velocity control volumes are staggered in the Y direction as shown in Figure 6.1.

The solution technique used is Eulerian as the cells do not change in size or position and the flow variables are calculated for each cell at any point in time.

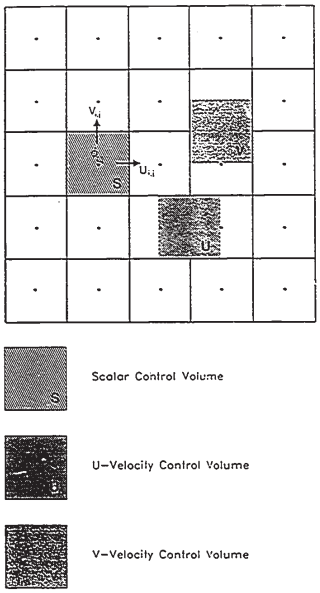


**Figure 6.1: Control Volume Orientation**



## 6.3 Discretization Equation

For a two-dimensional, Cartesian coordinate system, a general conservation equation may be written

$$\frac{\partial(\rho\phi)}{\partial t} + \frac{\partial(\rho u\phi)}{\partial x} + \frac{\partial(\rho v\phi)}{\partial y} = \frac{\partial}{\partial x}\left[\Gamma\frac{\partial\phi}{\partial x}\right] + \frac{\partial}{\partial y}\left[\Gamma\frac{\partial\phi}{\partial y}\right] + S \qquad (6.1)$$

where $\phi$ is a general transport variable (U, V, P, $\Theta$, $k^*$ or $\varepsilon^*$),

$\rho$ is the fluid density,

$\Gamma$ is the diffusion coefficient and

S is the source term.

The first term on the left hand side of equation 6.1 is the temporal term and represents the rate of change of $\phi$ per unit volume. The remaining terms on the left hand side account for the flux of $\phi$ convected by the flowrate and are called the convection terms. The bracketed terms on the right hand side are the diffusion terms modelled using a gradient mechanism. The last term in the equation is the volumetric generation of $\phi$ and is referred to the source term.

A general finite difference equation may be derived for equation 6.1 as described by Patankar [68]. As the formulation is Eulerian, the transport equation may be integrated over its corresponding control volume. The flux across the face of the control volume is

$$J_i = \rho u_i\phi - \Gamma\frac{\partial\phi}{\partial x_i} \qquad (6.2)$$

where i represents the north, south, east, and west faces as shown in Figure 6.2. Substitution of equation 6.2 into 6.1 and subsequent integration over the control volume yields



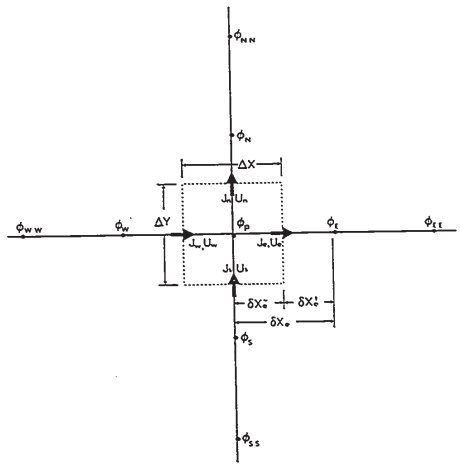


**Figure 6.2: Typical Control Volume**



$$\frac{\left(\rho_P\phi_P - \rho_P^\circ\phi_P^\circ\right)}{\Delta t} + J_wA_w - J_eA_e + J_sA_s - J_nA_n + \bar{S}\Delta V = 0 \qquad (6.3)$$

where $A_i$ is the area of the north, south, east and west faces,

$\bar{S}$ is the averaged source term over the control volume,

$\Delta V$ is the volume of the control volume and

the superscript $^\circ$ refers to the previous time step.

From this flux equation, Patankar [68] has derived a discretization equation of the form

$$a_P\phi_P = a_E\phi_E + a_W\phi_W + a_N\phi_N + a_S\phi_S + a_b \qquad (6.4)$$

or

$$a_P\phi_P = \sum a_{nb}\phi_{nb} + a_b \qquad (6.5)$$

where the subscripts P, E, W, S, and nb refer to the point, east, west, north, south and neighbouring points respectively. The discretization coefficients, a, are

$$a_P = a_E + a_W + a_N + a_S + a_P^\circ - S_p\,\Delta x\,\Delta y \qquad (6.6)$$

$$a_E = D_eA(|P_e|) + MAX[-F_e, 0] \qquad (6.7)$$

$$a_W = D_wA(|P_w|) + MAX[F_w, 0] \qquad (6.8)$$

$$a_N = D_nA(|P_n|) + MAX[-F_n, 0] \qquad (6.9)$$

$$a_S = D_sA(|P_s|) + MAX[F_s, 0] \qquad (6.10)$$

$$a_P^\circ = \frac{\rho^\circ\Delta x\,\Delta y}{\Delta t} \qquad (6.11)$$

$$a_b = S_C \Delta x \Delta y + a_P^o \phi_P^o \tag{6.12}$$

Here the source term, $\bar{S}$, has been linearized in the form

$$\bar{S} = S_P \phi + S_C \tag{6.13}$$

This linearization of the source term will be discussed in greater detail in section 6.6. The conductances, D, are defined by

$$D_e = A_e \left[ \frac{\delta x_e^-}{\Gamma_P} + \frac{\delta x_e^+}{\Gamma_E} \right] \tag{6.14}$$

the mass flow rates by

$$F_e = (\rho u)_e \Delta y \tag{6.15}$$

and the Peclet numbers by

$$P_e = \frac{F_e}{D_e} \tag{6.16}$$

Similar equations may be written for the north, south, and west faces.

The function, A( | P | ), accounts for the discretization of the convection terms in the governing equations. Expressions for A( | P | ) are listed in Table 6.1 for various first order schemes [68]. Patankar [69] suggests using the power law scheme.



Table 6.1 The Function A( | P | ) for Different Schemes

| Scheme | Formula for A( \| P \| ) |
|---|---|
| Central Difference | 1 - 0.5 \| P \| |
| Upwind | 1 |
| Hybrid | MAX [0, 1 - 0.5 \| P \| ] |
| Power Law | MAX [0, (1 - 0.1 \| P \| $^5$] |
| Exponential (exact) | \| P \| /{exp ( \| P \| ) - 1} |

## 6.4 QUICK Differencing

For multidimensional convection-diffusion formulations, false diffusion can be generated by the numerical scheme. False diffusion occurs when the flow is skewed to the computational grid and is a result of assuming each control volume face is locally one-dimensional [68]. Techniques can be adopted to decrease the false diffusion to an insignificant amount in comparison with the real diffusion. Two common techniques are the use of a finer grid and orienting the grid in the direction of the flow [68]. Another technique that has been incorporated into the present computer code is the use of a higher order differencing scheme.

Leschziner [73] recently reviewed the performance of two higher order schemes and one skew scheme. These include the second order upwind scheme (HOUS) [74], the quadratic upstream-weighted interpolation scheme (QUICK) [75] and the skew upwind differencing scheme (SUDS) [76]. From a review of modelling recirculating turbulent flows, Leschziner found that overall, QUICK provides the best performance. Patankar [77] suggests that lower order schemes



introduce false diffusion but are stable while higher order schemes such as QUICK reduce false diffusion but lead to overshoots and undershoots and often have difficulty with numerical stability.

In the present work, the QUICK scheme was implemented using the approach described in Giel [41] and is considered as a correction to the hybrid scheme. The first order schemes use a five point computational molecule ($\phi_P$, $\phi_N$, $\phi_S$, $\phi_E$, and $\phi_W$) while QUICK uses a nine point molecule ($\phi_P$, $\phi_N$, $\phi_{NN}$, $\phi_S$, $\phi_{SS}$, $\phi_E$, $\phi_{EE}$, $\phi_W$, and $\phi_{WW}$). The correction is in the form of an additional source term in equation 6.4. This "QUICK" source term is

$$\begin{aligned} S_{QU}^{\phi} = {} & (a_n^Q - a_n^H)\phi_N + (a_S^Q - a_S^H)\phi_S + \\ & (a_E^Q - a_E^H)\phi_E + (a_W^Q - a_W^H)\phi_W + S_P^Q \phi_P + S_C^Q \end{aligned} \tag{6.17}$$

The superscript, H, refers to the hybrid scheme and the coefficients are calculated from equations 6.6-6.12 and Table 6.1. The superscripts, Q, refer to the QUICK scheme and these coefficients are calculated from

$$a_E^Q = F_e B_{2e} (0.5 + S_e) + F_e B_{2e} (0.5 - S_e) + F_w B_{3w} (0.5 - S_w) + D_e \tag{6.18}$$

$$a_W^Q = F_w B_{1w} (0.5 + S_w) + F_w B_{2w} (0.5 - S_w) + F_P B_{3e} (0.5 - S_e) + D_w \tag{6.19}$$

$$a_N^Q = F_n B_{2n} (0.5 + S_n) + F_n B_{2n} (0.5 - S_n) + F_P B_{3s} (0.5 - S_s) + D_n \tag{6.20}$$

$$a_S^Q = F_P B_{1s} (0.5 + S_s) + F_P B_{1s} (0.5 - S_s) + F_n B_{3n} (0.5 - S_n) + D_s \tag{6.21}$$

$$a_P^Q = a_E^Q + a_W^Q + a_N^Q + a_S^Q \tag{6.22}$$



$$\begin{aligned} a_{EE}^Q &= -F_e B_{3e} (0.5 - S_e) & a_{NN}^Q &= -F_n B_{3n} (0.5 - S_n) \\ a_{EE}^Q &= -F_e B_{3e} (0.5 - S_e) & a_{NN}^Q &= -F_n B_3 n (0.5 - S_n) \end{aligned} \tag{6.23}$$

$$S_C^Q = a_{EE}^Q \phi_{EE} + a_{WW}^Q \phi_{WW} + a_{NN}^Q \phi_{NN} + a_{ss}^Q \phi_{ss} \tag{6.24}$$

$$S_P^Q = -a_{EE}^Q + a_{WW}^Q + a_{NN}^Q + a_{SS}^Q \tag{6.25}$$

The variables $S_n$, $S_s$, $S_e$, and $S_w$ account for the sign of the velocity at the north, south, east and west faces respectively and are defined as

$$\begin{aligned} S_n &= sign(0.5, F_n) & S_e &= sign(0.5, F_e) \\ S_s &= sign(0.5, F_s) & S_w &= sign(0.5, F_w) \end{aligned} \tag{6.26}$$

where the function, sign, is defined as

$$sign(a,b) = \begin{cases} a \text{ if } b \geq 0. \\ -a \text{ if } b < 0. \end{cases} \tag{6.27}$$

The "B" variables or grid coefficients in equations 6.18-6.23 are only dependent on the grid spacing. These variables are implemented as described by Yap [43] and are derived in Appendix A.

## 6.5 Boundary Conditions

All of the boundary conditions presented in section 5.3 may be categorized into two categories: prescribed value or prescribed flux. The boundary conditions have been applied as

described by Raithby and Schneider [78]. Figure 6.3 shows a boundary cell with the following general boundary condition imposed on it.

$$c_1\phi + c_2\frac{\partial\phi}{\partial Y} = c_3 \tag{6.28}$$

A general discretized boundary condition equation for a node on the bottom boundary of the computational domain is

$$a_P(i,1)\ \phi_{i,1} = a_N(i,1)\ \phi_{i,2} + a_b(i,1) \tag{6.29}$$

$$a_S(i,1) = a_E(i,1) = a_W(i,1) = 0 \tag{6.30}$$

The coefficients for the boundary node, $\phi(i,1)$ are

$$a_P(i,1) = c_1 + \frac{c_2}{Y_1} \tag{6.31}$$

$$a_N(i,1) = \frac{c_2}{Y_1} \tag{6.32}$$

$$a_b(i,1) = c_1 c_3 - c_2 c_3 \tag{6.33}$$

$$a_S(i,1) = 0. \qquad a_e(i,1) = 0. \qquad a_w(i,1) = 0. \tag{6.34}$$

Raithby and Schneider [78] suggest the that the boundary condition equation be absorbed into the adjacent interior equation. This is accomplished using

$$\left[a_P(i,2)\right]^{NEW} = \left[a_P(i,2)\right]^{OLD} - \frac{a_S(i,2)\ a_n(i,1)}{a_P(i,1)} \tag{6.35}$$



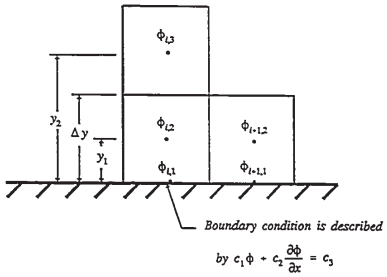


**Figure 6.3: Boundary Nodes with Typical Control Volume**



$$\left[a_b(i,2)\right]^{NEW} = \left[a_b(i,2)\right]^{OLD} + \frac{a_S(i,2)\ a_b(i,1)}{a_P(i,1)} \tag{6.36}$$

$$\left[a_S(i,2)\right]^{NEW} = 0 \tag{6.37}$$

## 6.6 Linearization of Source Terms

The dimensionless governing equations (eqns. 5.25-5.31) may be written in terms of the generalized conservation equation (eqn. 6.1) using the values in Table 6.2. The generalized discretization equation (eqn. 6.4) is derived in terms of a linearized source term as shown in equation 6.13. Patankar [68] states that, for a stable solution the source term must be linearized with a negative slope. In other words the value of $S_p$ must be less than or equal to zero. The source terms for each equation are linearized as follows.

*Dimensionless X-Momentum*

All of the source term components are placed in the constant portion of the source term since none of these components are explicit functions of U.

$$S_C^U = \frac{\partial}{\partial X}\left[\left[\frac{a}{Re_L} + \frac{a}{Re_T}\right]\frac{\partial U}{\partial X}\right] + \frac{\partial}{\partial Y}\left[\left[\frac{a}{Re_L} + \frac{a}{Re_T}\right]\frac{\partial V}{\partial X}\right] + \frac{(Gr_x)_L\ a^2}{Re_L^2}\theta - \frac{2}{3}\frac{\partial k^*}{\partial X} + S_{QU}^U \tag{6.38}$$

$$S_C^U = S_{VIS}^U + S_{BUOY}^U + S_{TUR}^U + S_{QU}^U$$



**Table 6.2: Summary of the Dimensionless Governing Equations**

| $\phi$ | $\rho$ | $\Gamma^\phi$ | $\bar{S}^\phi$ |
|---|---|---|---|
| U | 1 | $\left[\frac{a}{Re_L} + \frac{a}{Re_T}\right]$ | $\frac{\partial}{\partial X}\left[\left[\frac{a}{Re_L} + \frac{a}{Re_T}\right]\frac{\partial U}{\partial X}\right] + \frac{\partial}{\partial Y}\left[\left[\frac{a}{Re_L} + \frac{a}{Re_T}\right]\frac{\partial V}{\partial X}\right] + \frac{(Gr_x)_L\ a^2}{Re_L^2}\theta - \frac{2}{3}\frac{\partial k^*}{\partial X} + S_{QU}^U$ |
| V | 1 | $\left[\frac{a}{Re_L} + \frac{a}{Re_T}\right]$ | $\frac{\partial}{\partial X}\left[\left[\frac{a}{Re_L} + \frac{a}{Re_T}\right]\frac{\partial U}{\partial Y}\right] + \frac{\partial}{\partial Y}\left[\left[\frac{a}{Re_L} + \frac{a}{Re_T}\right]\frac{\partial V}{\partial Y}\right] + \frac{(Gr_y)_L a^2}{Re_L^2}\theta - \frac{2}{3}\frac{\partial k^*}{\partial Y} + S_{QU}^V$ |
| $\theta$ | 1 | $\left[\frac{a}{Re_L Pr_T} + \frac{a}{Re_T \sigma_T}\right]$ | $S_{QU}^\theta$ |
| $k^*$ | 1 | $\left[\frac{a}{Re_L} + \frac{a}{\sigma_k Re_T}\right]$ | $G^* - \bar{\varepsilon}^* - \frac{a^3(Gr_x)_T}{\sigma_T Re_T^2}\frac{\partial\theta}{\partial X} - \frac{a^3(Gr_y)_T}{\sigma_T Re_T^2}\frac{\partial\theta}{\partial Y} - D^* + S_{QU}^{k^*}$ |
| $\bar{\varepsilon}^*$ | 1 | $\left[\frac{a}{Re_L} + \frac{a}{\sigma_\varepsilon Re_T}\right]$ | $C_{f_1}\frac{\bar{\varepsilon}^*}{k^*}G^* - C_{f_2}\frac{\bar{\varepsilon}^{*2}}{k^*} - C_{f_3}\frac{\bar{\varepsilon}^*}{k^*}\frac{a^3(Gr)_T}{\sigma_T Re_T^2}\frac{\partial\theta}{\partial X_i} + E^* + S_{QU}^{\bar{\varepsilon}^*}$ |

*Dimensionless Y-Momentum*

Similarly, all of the source components of the Y-Momentum equation are placed in the constant portion of the source term.

$$S_C^V = \frac{\partial}{\partial X}\left[\left[\frac{a}{Re_L}+\frac{a}{Re_T}\right]\frac{\partial U}{\partial Y}\right] + \frac{\partial}{\partial Y}\left[\left[\frac{a}{Re_L}+\frac{a}{Re_T}\right]\frac{\partial V}{\partial Y}\right] + \frac{(Gr_y)_L a^2}{Re_L^2}\theta - \frac{2}{3}\frac{\partial k^*}{\partial y} + S_{QU}^V$$
$$S_C^V + S_{VIS}^V + S_{BUOY}^V + S_{TUR}^V + S_{QU}^V \qquad (6.39)$$

*Dimensionless Energy*

Similarly the QUICK component is placed in the constant part of the source term.

$$S_C^\theta = S_{QU}^\theta \qquad (6.40)$$

*Dimensionless Turbulent Kinetic Energy*

Neither the generation term,

$$S_{GEN}^{k^*} = G^*, \qquad (6.41)$$

or the QUICK correction, $S_{QU}^{k^*}$, are explicit functions of turbulent kinetic energy and are therefore placed in the constant part of the source term.

The dissipation term is not explicitly a function of $k^*$. Due to the strong coupling of $k^*$ and $\varepsilon^*$, this term may cause stability problems. To add stability to the calculations, the



dissipation term is written in terms of the Reynolds number based on turbulent viscosity (eqn. 5.28) and is added to the variable part of the source term.

$$S_{DIS}^{k^*} = \frac{1}{k^*}\left[-\varepsilon^*\right] = -\frac{f_\mu C_\mu k^* Re_T}{a} \qquad (6.42)$$

The buoyancy term,

$$S_{BUOY}^{k^*} = \frac{a^3 (Gr_x)_T}{\sigma_T Re_T^3}\frac{\partial \theta}{\partial X} - \frac{a^3 (Gr_y)_T}{\sigma_T Re_T^3}\frac{\partial \theta}{\partial Y} \qquad (6.43)$$

can be either positive or negative depending on the temperature gradients. If this term is positive it is added to the constant part of the source term. If it is negative, it is linearized using the definition of turbulent Reynolds number (eqn. 5.28) and is added to $S_P^k$.

$$k_{LIN}^* = \left[\frac{a\,\bar{\varepsilon}^*}{f_\mu C_\mu Re_T}\right]^{1/2} \qquad (6.44)$$

The extra term, $-D^*$, is always negative for the Jones-Launder low Reynolds number approach as shown by

$$S_{LR}^{k^*} = -D^* = -2\frac{a}{Re_L}\left[\left[\frac{\partial k^{*1/2}}{\partial X}\right]^2 + \left[\frac{\partial k^{*1/2}}{\partial Y}\right]^2\right] \qquad (6.45)$$

This term is also linearized and added to the variable source term.



*Dimensionless Dissipation of Turbulent Kinetic Energy*

The source terms in the dissipation equation are linearized in a similar manner to that of the turbulent kinetic energy equation . In each of the source terms (with the exception of the QUICK and Yap corrections) the term, $\frac{\bar{\varepsilon}^*}{k^*}$, appears. This term is calculated from the definition of the Reynolds number based on turbulent viscosity (eqn. 5.28).

$$\left[\frac{\bar{\varepsilon}^*}{k^*}\right] = \frac{f_\mu C_\mu Re_T k^*}{a} \qquad (6.46)$$

The generation term is not explicitly a function of $\bar{\varepsilon}^*$, and is added to the $S_C$ portion of the source term

$$S_{GEN}^{\bar{\varepsilon}^*} = C_1 f_1 G^*\left[\frac{f_\mu C_\mu Re_T k^*}{a}\right] \qquad (6.47)$$

The dissipation term is added to the variable part of the source term as it is always negative.

$$S_{DIS}^{\bar{\varepsilon}^*} = C_2 f_2\left[\frac{f_\mu C_\mu Re_T k^*}{a}\right] \qquad (6.48)$$

As in the case of the turbulent kinetic energy, the buoyancy term may be either positive or negative depending on the temperature gradient. For a positive buoyancy term, it is added to the constant part of the source term.



$$S_{BUOY}^{\bar{\varepsilon}^*} = -C_3 f_3 \frac{a^3 (Gr_x)_T}{\sigma_T Re_T^3}\left[\frac{f_\mu C_\mu Re_T k^*}{a}\right]\frac{\partial \theta}{\partial X} - C_3 f_3 \frac{a^3 (Gr_y)_T}{\sigma_T Re_T^3}\left[\frac{f_\mu C_\mu Re_T k^*}{a}\right]\frac{\partial \theta}{\partial Y} \qquad (6.49)$$

If the buoyancy term is negative, it is linearized using equation 6.50 and is added to $S_P$.

$$\bar{\varepsilon}_{LIN}^* = \frac{f_\mu C_\mu k^{*2} Re_T}{a} \qquad (6.50)$$

Since the QUICK correction is not explicitly a function of $\bar{\varepsilon}^*$, it is added to $S_C$.

A summary of the linearization of the source terms is presented in Table 6.3.

**Table 6.3: Summary of Source Term Linearization**

| $\phi$ | $S_C^\phi$ | $S_P^\phi$ |
|---|---|---|
| U | $S_{VIS}^U + S_{BUOY}^U + S_{TUR}^U + S_{QU}^U$ | 0. |
| V | $S_{VIS}^V + S_{BUOY}^V + S_{TUR}^V + S_{QU}^V$ | 0. |
| $\theta$ | $S_{QU}^\theta$ | 0. |
| $k^*$ | $S_{GEN}^{k^*} + \max(0., S_{BUOY}^{k^*}) + S_{QU}^{k^*}$ | $\frac{S_{DIS}^{k^*}}{k^*} + \frac{\min(0., S_{BUOY}^{k^*}) + S_{LR}^{k^*}}{k_{LIN}^*}$ |
| $\bar{\varepsilon}^*$ | $S_{GEN}^{\bar{\varepsilon}^*} + \max(0., S_{BUOY}^{\bar{\varepsilon}^*}) + S_{QU}^{\bar{\varepsilon}^*} + S_{YAP}^{\bar{\varepsilon}^*}$ | $\frac{S_{DIS}^{\bar{\varepsilon}^*}}{\bar{\varepsilon}^*} + \frac{\min(0., S_{BUOY}^{\bar{\varepsilon}^*}) + S_{LR}^{\bar{\varepsilon}^*}}{\bar{\varepsilon}_{LIN}^*}$ |

### 6.7 Variable Property Model

When the variable property option is selected, the local Reynolds, Prandtl and Grashof numbers are computed based on the local thermophysical properties. In addition the Boussinesq approximation is corrected by calculating the dimensional buoyancy term as, $-\rho g$. This correction is in the form of an additional source term in equation 6.4. For the dimensionless y-momentum equation, this "variable property" source term is

$$S_{VP}^{v} = \frac{-g(\rho - \rho_R)}{\rho_R}\frac{H}{u_j^2} - S_{BUOY}^{v} \tag{6.51}$$

The effect of using a constant property model with the Boussinesq approximation or using a variable property model with equation 6.51 will be discussed in section 7.4.4.

### 6.8 Pressure-Velocity Coupling

The main difficulty when solving the governing equations is that the velocities cannot be directly computed from the momentum equations (eqns. 5.22 & 5.23). These equations contain the pressure gradient which is not expressible in terms of velocities. The continuity equation (eqn. 5.21) indirectly determines the pressure field. The SIMPLER algorithm is used to couple the pressure and velocity fields. This algorithm is described in this section as cited by Patankar [68].

The discretized momentum equations may be written as

$$a_e u_e = \sum a_{nb} u_{nb} + b + A_e(p_P - p_E) \tag{6.52}$$

The coefficient expressions for $a_{nb}$, $a_e$, and b are given in equations (eqns. 6.6-6.12). As stated above it is not possible to directly solve for the velocities using the discretized momentum



equation as the pressure field is not known. It is however, possible to solve the momentum equations for a given pressure field. Let $u^*$ denote the velocity field based on an estimated pressure field $p^*$. Thus

$$a_e u_e^* = \sum a_{nb} u_{nb}^* + b + A_e(p_P^* - p_E^*) \tag{6.53}$$

In general, this estimated pressure and velocity field will not satisfy the continuity equation. Thus these values must be corrected using

$$p = p^* + p' \tag{6.54}$$

$$u = u^* + u' \tag{6.55}$$

$$v = v^* + v' \tag{6.56}$$

where the asterisk refers to the estimated component and the prime denotes the correction.

A discretized equation for the pressure correction may be derived and cast into the form

$$a_P p_P' = a_E p_E' + a_W p_W' + a_N p_N' + a_S p_S' + a_b \tag{6.57}$$

$$a_E = \rho_e d_e \Delta y \tag{6.58}$$

$$a_W = \rho_w d_w \Delta y \tag{6.59}$$

$$a_N = \rho_n d_n \Delta x \tag{6.60}$$

$$a_S = \rho_s d_s \Delta x \tag{6.61}$$

$$a_P = a_E + a_W + a_N + a_S \tag{6.62}$$



$$a_b = \frac{(\rho_P^0 - \rho_P)\,\Delta x\,\Delta y}{\Delta T} + \left[(\rho u^*)_w - (\rho u^*)_e\right]\Delta y + \left[(\rho v^*)_n - (\rho v^*)_s\right]\Delta x \tag{6.63}$$

where the pressure coefficient, d, is defined as

$$d_e = \frac{A_e}{a_e} \qquad d_w = \frac{A_w}{a_w}$$

$$d_n = \frac{A_n}{a_n} \qquad d_s = \frac{A_s}{a_s} \tag{6.64}$$

The velocities may then be corrected using

$$u_e = u_e^* + d_e(p_P' - p_E') \tag{6.65}$$

$$v_n = v_N^* + d_n(p_P' - p_N') \tag{6.66}$$

Once the velocities are corrected, the temperatures may be calculated using Equations (6.5 - 6.12).

### 6.9 Summary of Steps in a Computational Cycle

The following are the steps in a cycle as cited by Patankar [68,69].

1. Start with a guessed velocity field.
2. Calculate the coefficients for the momentum equations and hence calculate $\hat{u}$, $\hat{v}$ from the momentum equations such as equation (6.52) by substituting the values of the neighbour velocities. Note that this is simply a substitution; no simultaneous equations are involved.



3. Calculate the coefficients for the pressure equation (6.53), and solve it to obtain the pressure field. The simultaneous equations are solved with the use of Gauss-Seidel.
4. Treating this pressure field as $p^*$, solve the momentum equations to obtain $u^*$ and $v^*$. These velocities are calculated using a method described in section 6.8.
5. Calculate the mass source b from equation (6.63) and hence solve the p′ equation (6.56). The simultaneous equations are solved with the use of Gauss-Seidel.
6. Solve the discretized equations for temperature, turbulent kinetic energy, and dissipation of turbulent kinetic energy using Equation (6.4). These variables are also solved using a method described in section 6.10.
7. Return to step 2.

### 6.10 Solution of Algebraic Equations

The application of the finite difference method previously described leads to a system of equations that must be solved. These equations, written in matrix form, are of the form

$$[A]\{\phi\} = \{b\} \tag{6.67}$$

where the coefficient matrix, [A] is pentadiagonal, $\{\phi\}$ is the unknown, and {b} is a matrix of constants. In the present work, the solution of this matrix equation has been implemented using three procedures: the Alternating Direction Implicit (ADI) procedure of Peaceman and Rachford [79], the Strongly Implicit Procedure (SIP) of Stone [80], and the Modified Strongly Implicit Procedure (MSI) of Schneider and Zedan [81]. For a comparison of these solution methods, several case studies were investigated. The results of these case studies indicated that each method yielded identical results with a maximum difference of CPU time of 4.6%. While all of the solution procedures are available in the computer code, the MSI procedure has been adopted in most cases as this procedure was found to be most stable.

### 6.11 Description of FLUENT Software

Two and three-dimensional solutions have been obtained with the commercial software package, FLUENT [63]. These results were obtained on a Silicon Graphics workstation and were displayed with the commercial graphics package, TECPLOT. FLUENT is a general purpose software package capable of predicting many types of flow. The discretization is based on a finite control volume approach and the pressure-velocity coupling is a SIMPLE family algorithm. The present solutions are obtained using a first order differencing scheme, a variable property model and a standard k-ε turbulence model with wall functions. Low Reynolds number turbulence models are not available in FLUENT.

# CHAPTER 7

# RESULTS AND DISCUSSION

### 7.1 Introduction

The interaction of buoyancy and inertia in the cavity described in Figure 3.1 has been investigated in the present work. Four cases are considered and the specific parameters are summarized in Table 7.1.

Table 7.1: Summary of Cases

| Case | 1 | 2 | 3 | 4 |
|---|---|---|---|---|
| a | 0.027 | 0.027 | 0.027 | 0.027 |
| A | 2 | 2 | 2 | 2 |
| $u_i$ (m/s) | .123 | .124 | .063 | .063 |
| $T_w$ (° C) | 20.0 | 42.5 | 63.0 | 80.6 |
| $T_i$ (° C) | 20.0 | 22.3 | 24.0 | 25.9 |
| Pr | 7.03 | 5.14 | 4.05 | 3.36 |
| $Re_D$ | 973. | 1283. | 808. | 950. |
| $Re_H$ ($10^4$) | 3.61 | 4.76 | 3.00 | 3.53 |
| $Gr_H$($10^9$) | 0 | 2.87 | 10.7 | 24.2 |
| $Ra_H$ ($10^{10}$) | 0 | 1.48 | 4.33 | 8.13 |
| $Ri_H$ | 0 | 1.27 | 11.9 | 19.4 |

The first case is purely turbulent recirculating flow as this case is isothermal. The remaining cases have increasing amounts of heat transfer. These cases are selected as they cover the entire range from interia dominated flows to buoyancy dominated flows. In other words, case 1 is





completely dominated by inertia and case 4 is buoyancy dominated. The remaining two cases represent intermediate degrees of buoyancy and inertia. Although case 1 is isothermal, the right vertical wall of the cavity is referred to as the "heated wall". The fluid properties are computed from equations 5.49 to 5.53 and are evaluated at a reference temperature given by equation 5.5.

The Richardson number is a dimensionless parameter and is defined as the ratio of the buoyancy to inertial forces. It is derived from the dimensionless buoyancy term in the momentum equation and is calculated from

$$Ri = a^2 \frac{Gr_H}{Re_D^2} \tag{7.1}$$

The scaling factor, $a^2$, is present as the Grashof and Reynolds numbers are based on different length scales.

The experimental results are shown in sections 7.2.1, 7.2.2 and 7.2.3. These include the flow visualization, LDA measurements and the temperature results respectively. The numerical results are presented in sections 7.3 to 7.5. A comparison of the experimental and numerical results is presented in section 7.6.

### 7.2 Experimental Results

Although the flow in the cavity is observed to oscillate, the experimental data can be taken as reliable since high Rayleigh number convective flows are by nature unsteady. Le Quéré [82] used direct numerical simulations of turbulent flows to investigate natural convection in vertical rectangular enclosures. Le Quéré [82] observed that if the Rayleigh number exceed some critical value, the flow was unsteady. For a water filled cavity with an aspect ratio of 10, the critical Rayleigh number was found to be between 8 X $10^9$ and 9 X $10^9$. Henkes and



Hoogendoorn [83] studied natural convection in water filled vertical square cavities and found the critical Rayleigh number to be between 4 X $10^9$ and 5 X $10^9$. Le Quéré [82] attributes this instability to the interaction of travelling waves in the vertical boundary layers and thermal instabilities along the horizontal walls. For case 2, 3 and 4 of the present work, the flow is expected to be unsteady since the Rayleigh number for these cases exceeds the critical values cited. It must be noted that the magnitude of the oscillations is small in comparison to the large scale fluid motion. As an example, the separation location (defined in section 7.2.1) is observed to oscillate within a 5 mm band. However, the size of the large scale flow cells are at least an order of magnitude higher. Thus the time-averaged governing equations would apply to the flow field.

An uncertainty analysis for the measured data is presented in Appendix B.

#### 7.2.1 Flow Visualization

Although two methods of flow visualization are presented in Chapters 3 and 4, only the results of the laser induced fluorescence technique is presented. The quality of the results of the particle streak technique are substandard when reproduced from a slide. Neither technique could be recorded on the camcorder due to insufficient light. In the plane of symmetry (x-y plane), the results of the flow visualization suggest that, for the heated wall cases, two flow regimes are possible. These two flow regimes are shown schematically in Figure 7.1. The shaded region shows the region of illumination in the cavity. Unless otherwise specified, the coordinate system used throughout this chapter is defined in Figure 3.1.

The first regime is referred to as "separated flow" and is shown schematically in Figure 7.1 (a). The inlet jet enters the cavity and flows along the top boundary. When the heated wall

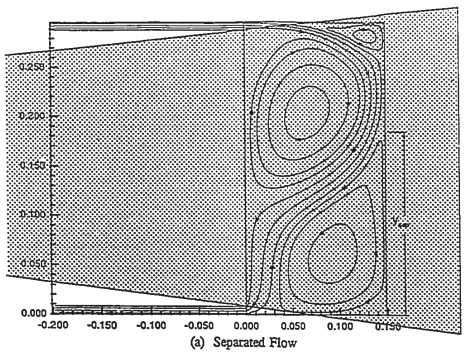


(a) Separated Flow

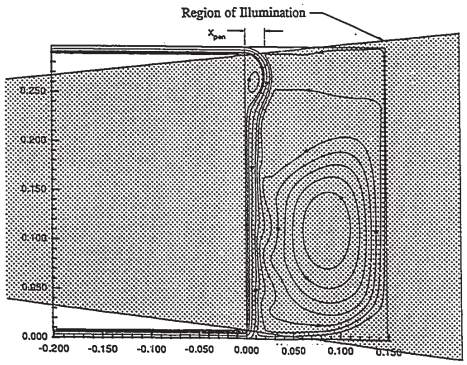


(b) Buoyancy dominated

**Figure 7.1:** Observed Flow Regimes



is reached, the flow turns downward. However at some point, this inertia driven flow meets an upward flow due to buoyancy or recirculation and the flow separates at the wall. This separation height, $y_{sep}$, is shown in Figure 7.1(a) and is defined as the distance from the separation point to the bottom of the cavity. The fluid then flows toward the exit of the cavity. This flow regime is characterized with three recirculation regions. The first recirculation cell is a clockwise rotating cell due to the inlet jet. The second is a counterclockwise cell located in the bottom corner adjacent to the heated wall. The size of these two rotating cells is dependent on the Richardson number. A small counterclockwise rotating cell is also observed in the top corner adjacent to the heated wall.

The second regime is referred to as "buoyancy dominated flow" and is shown schematically in Figure 7.1 (b). The inlet jet enters the cavity and begins to flow along the top boundary. However the buoyancy cell dominates the flow and the inlet jet separates along the top boundary. The distance from this separation point to the inlet is referred to as the "penetration depth", $x_{pen}$. This regime has a large counterclockwise cell due to buoyancy. A small clockwise rotating cell may be observed below the inlet adjacent to the adiabatic vertical wall.

The separated flow regime is observed in the isothermal and low Richardson number cases (Cases 1 to 3) as shown in Figures 7.2 (a) to 7.4 (a). The penetration of fresh water into the cavity is shown by green dye in these figures. As the relative magnitude of buoyancy is increased (and hence the Richardson number), the clockwise inertially driven cell decreases in size and the counterclockwise buoyancy driven cell enlarges. As a result of the changing of size of cells, the separation height increases. If the Richardson number is high enough, buoyancy will dominate the flow and the separation location will move up the heated wall and across the top



(b) Wall Plane

(a) Plane of Symmetry

**Figure 7.2:** Case 1-Flow Visualization



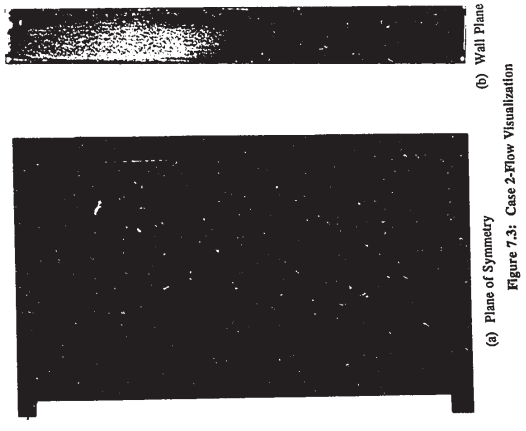

(b) Wall Plane

(a) Plane of Symmetry

**Figure 7.3:** Case 2-Flow Visualization

(b) Wall Plane

(a) Plane of Symmetry

Figure 7.4: Case 3-Flow Visualization



(a) Plane of Symmetry

Figure 7.5: Case 4-Flow Visualization



of the cavity. This is observed in the highest Richardson number case (see Figure 7.5 (a)). Thus the buoyancy dominated flow regime may be considered a special case of the separated regime.

Although the scope of the present work deals with the steady state solutions, the separation location was observed to oscillate with an amplitude of about 5 mm. The frequency of this oscillation will be discussed in section 7.2.3.

The two dimensionality of the flow is also studied with flow visualization. The flow field in a plane 4 mm from the heated wall (hereafter referred to as the "wall plane") is presented in Figures 7.2 (b) to 7.4 (b). Although the dye is injected at the entrance of the developing length, the dye is not visible at the inlet of the cavity as the laser light is blocked out by the entrance channel (see Figure 7.1). The separation height may be quantified by measuring the height of downward penetration of green dye adjacent to the heated wall in the plane of symmetry. In addition, the separation height profile in the y-z plane is studied by observing the flow visualization in the wall plane. In this plane the separation height is a maximum near the symmetry plane and a minimum near the faces of the cavity. Although the flow visualization for the plane of symmetry and the wall plane was performed at least a week apart, the separation heights in the plane of symmetry appear to be consistent with the separation heights in the wall plane. This suggests the work is repeatable. In Figure 7.5, the penetration depth cannot be quantified as this point is not in the illuminated region of the cavity (see Figure 7.1 (b). A summary of the dimensionless separation heights is presented in Table 7.2.



Table 7.2: Summary of Dimensionless Separation Heights from Flow Visualization

| Case | Ri | $Y_{sep}$ | |
|---|---|---|---|
| | | Symmetry Plane | Wall Plane |
| 1 | 0 | .37 | .34 |
| 2 | 1.27 | .54 | .53 |
| 3 | 11.9 | .73 | .66 |

### 7.2.2 Velocity Measurements

The results of the laser Doppler anemometer measurements are presented in Figures 7.6 to 7.9.). In each of these figures, the results are shown in the inlet plane (y = 293 mm), the plane of symmetry (z =0), the wall plane (x = 144.5 mm) and the exit plane (y = 4 mm). Only the u component of velocity is measured in the inlet and exit planes and only the v velocity component is measured in the wall plane as these components of velocity are dominant and because of difficulties in measuring velocities close to a wall. The time-averaged and fluctuating components of velocity (u, u', v, and v') are presented on a floppy disk in Appendix C.

The isothermal case is shown in Figure 7.6. The velocity measurements in the plane of symmetry are consistent with the flow visualization presented in Figure 7.2. The flow in the bulk of the cavity is dominated by one large clockwise rotating cell. Small secondary counter clockwise cells are located in each of the corners adjacent to the heated wall. The flow regime is separated flow and the separation height is approximately 70 mm or 0.24 in dimensionless units.

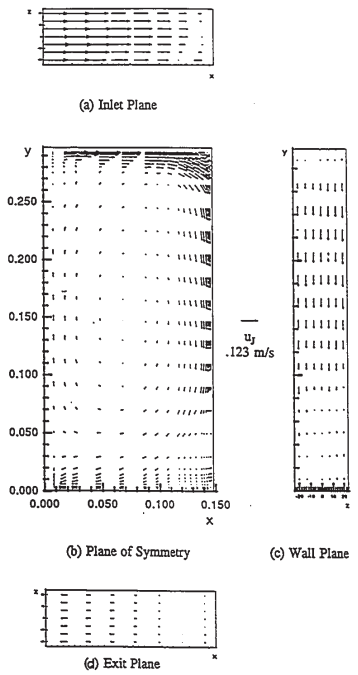


**Figure 7.6: Case 1-LDA Results**



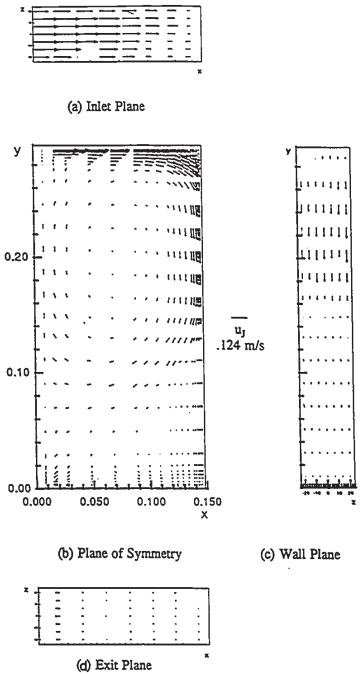


**Figure 7.7: Case 2-LDA Results**



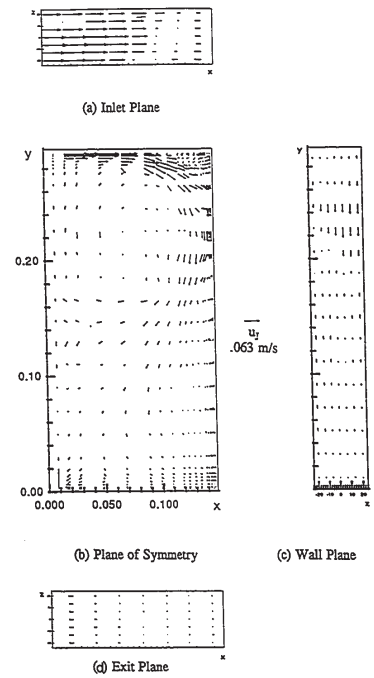


**Figure 7.8: Case 3-LDA Results**



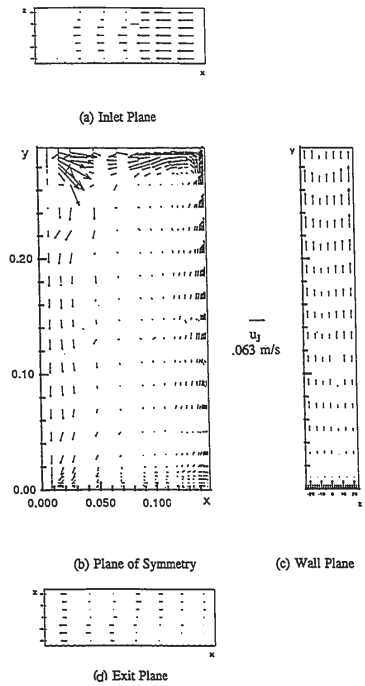


**Figure 7.9: Case 4-LDA Results**

The inlet plane shows the fluid enters the cavity with a flat velocity profile. As the jet moves across the top of the cavity, the velocity profile is less uniform as the velocity is a maximum in the plane of symmetry and slowly curves to zero at the faces of the cavity. In the vicinity of the heated wall, small regions of backflow are shown in the corners.

Above the separation height (approximately 70 mm or 0.24 dimensionless units), the downward flow adjacent to the heated wall (the wall plane) has a nearly uniform velocity distribution. The flow appears to lack two-dimensionality at the separation height and at the top and bottom corners of the cavity.

The velocity has a uniform distribution in the exit plane and hence appears to be two-dimensional in this region.

The measurements for case 2 are presented in Figure 7.7. In the plane of symmetry the results are again consistent with the flow visualization observations. When compared with the measurements for Case 1 (Figure 7.6(b)), the large inertially driven cell has decreased in size. The counter clockwise rotating cells adjacent to the heated wall have increased in size due to higher vertical momentum as heat is transferred from the wall to the fluid. The flow regime is separated flow and the separation height is 120 mm or 0.4 dimensionless units.

At the entrance of the cavity, the flow has a reasonably flat profile as shown in the inlet plane. However, the boundary layers adjacent to the two faces ($z = \pm$ 24 mm) appear to be thicker than in the preceding case. For x greater than 0.1 m, the flow is influenced by the counterclockwise cell in the top corner adjacent to the heated wall and lacks two-dimensionality.

In the wall plane, the flow is two-dimensional everywhere except in the top corner. The separation height in this plane is shown to be approximately 0.15 m or 0.5 dimensionless units. The velocity is also shown to be much higher above the separation point.



The velocity measurements for Case 3 are shown in Figure 7.8. In the plane of symmetry the overall flow field and location of separation agree with the flow visualization results of Figure 7.4. The clockwise rotating cell has decreased in size to approximately the upper half of the cavity. Both of the counter clockwise rotating cells adjacent to the heated wall have increased in size and strength. The separation on the heated wall occurs at approximately 190 mm or 0.64 dimensionless units.

In the inlet plane the flow is similar to the previous case. However the counter clockwise cell in the upper corner is stronger and hence more backflow exists. In the region of backflow the flow is not two-dimensional.

The velocity vectors in the wall plane suggest that the flow is nearly two-dimensional in this plane with the exception of the region near separation. In this plane, the separation height is 190 mm or 0.64 dimensionless units.

The velocity measurements for case 4 are presented in Figure 7.9. In the plane of symmetry the flow in the bulk of the cavity is driven by buoyancy. The water adjacent to the heated wall rises as the fluid is heated. When this upward motion meets the top boundary, the fluid turns toward the entrance until it meets the incoming jet. At this location both the buoyancy driven flow and the incoming flow turn towards the bottom of the cavity. As the fluid reaches the bottom boundary, the fluid divides with some turning towards the heated wall and the remainder leaving the cavity.

The velocity vectors in the wall plane show the fluid is nearly two-dimensional in this plane. At the bottom of the cavity the velocity profile is flat but as the fluid moves up the wall, the velocity vectors are slightly larger at the faces of the cavity.



The velocity vectors in the inlet plane suggest that the buoyant flow is two-dimensional when it starts to flow along the top boundary. However as the flow approaches the incoming jet, it lacks two-dimensionality. This plane shows the penetration depth to be approximately 25 mm or 0.084 dimensionless units.

In the exit plane the flow lacks two-dimensionality everywhere except in the vicinity of the cavity exit.

For each of the cases, detailed velocity measurements of the separation regions are shown in Figure 7.10. The location of separation is summarized in Table 7.3 and is compared with the measured separation locations from the previous figures. For each of the cases, the time required to collect the velocity data for the plane of symmetry was of the order of a week. In each of the figures presented thus far, comparison of the separation heights would suggest that the experiment is fairly repeatable as the separation heights differ only slightly between figures.

The flow in the exit region is important to understand as the correct boundary conditions are not known apriori when modelling the flow. It may be possible to assume the flow is a fully developed outlet ($\partial\Phi/\partial X = 0$) or the flow may not be fully developed and the outlet channel may have to be modelled. For each case, the exit region is shown in Figure 7.11. The velocity vectors in this figure suggest that in the exit region the flow is not fully developed for any case. Thus an outlet channel must be modelled and the fully developed flow boundary condition can be applied at the exit of this channel. In general the higher the Richardson number, the steeper the slope of the velocity vectors at the exit. For the buoyancy dominated flow case, the vectors are almost vertical.



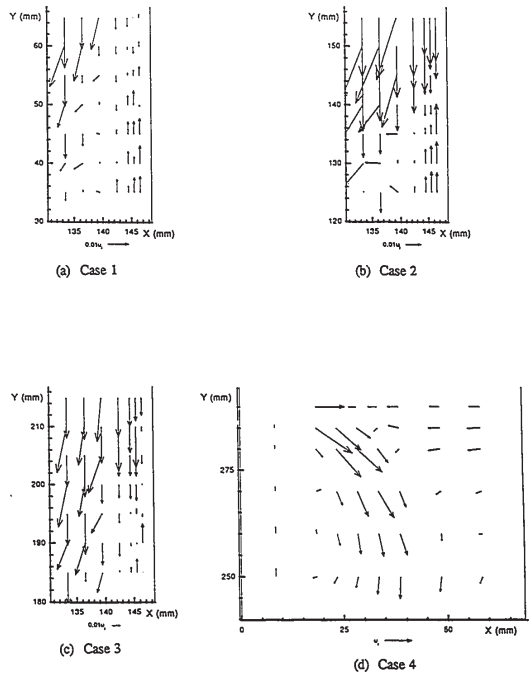


**Figure 7.10: LDA Measurements in Separation Region**

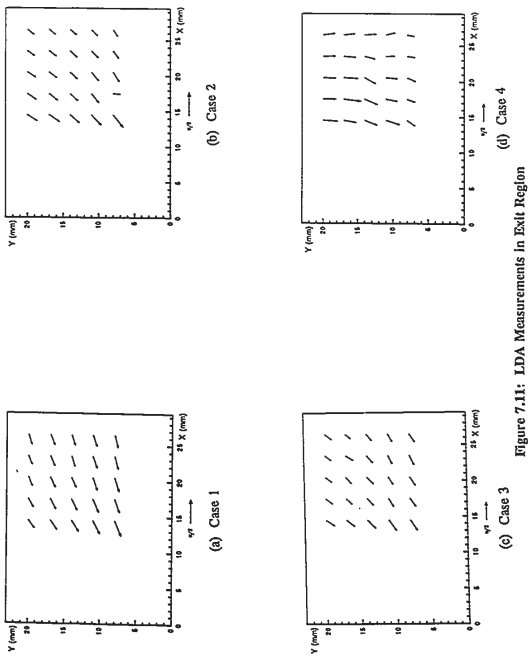


Figure 7.11: LDA Measurements in Exit Region



Table 7.3: Summary of Dimensionless Experimental Separation Locations

| | | $Y_{sep}$ | | | $X_{pen}$ |
|---|---|---|---|---|---|
| Case | | 1 | 2 | 3 | 4 |
| Ri | | 0 | 1.27 | 11.9 | 19.4 |
| Plane | Figures | | | | |
| Flow Visualization Symmetry Plane | 7.2(a)-7.5(a) | .37 | .54 | .53 | - |
| Flow Visualization Wall Plane | 7.2(a)-7.4(a) | .34 | .53 | .66 | - |
| LDA Symmetry Plane | 7.6(b)-7.9(b) | .24 | .4 | .64 | - |
| LDA Wall/Inlet Plane | 7.6(c)-7.8(c), 7.9(a) | .24 | .5 | .64 | .083 |
| LDA Separation Region | Figure 7.10 | .24 | .46 | .65 | .083 |

### 7.2.3 Temperature Measurements

Typical thermocouple outputs are shown in Figure 7.12 for Case 2. For the temperature measurements, the sampling period was 200 seconds and the sampling frequency was 10 Hz as described in section 4.4. The measurements shown in Figure 7.12 are approximately 0.4 mm from the heated wall at heights of 200, 140 and 80 mm. These heights correspond to typical data above, at and below the separation location respectively.

Above the separation location, the time-averaged dimensionless temperature is 0.27 and the temperature fluctuates between 0.05 and 0.65. In this region the fluid has recently entered the cavity, yet, the temperature has already risen to 27% of the total temperature difference in the cavity. The main modes of heat transfer to this water is due to two mechanisms. Firstly,



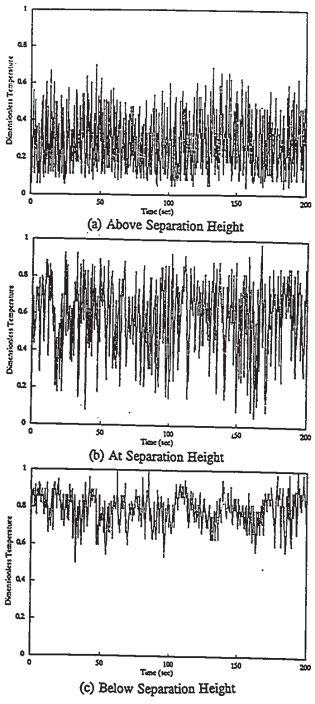


Figure 7.12: Typical Temperature Traces



the warm water that is rising along the vertical boundary opposite the heated wall (see Figure 7.7) mixes with the incoming jet. Secondly, at the top of the cavity, the rate of heat transfer is high adjacent to the heated wall as the cold jet impinges directly on a hot surface.

At the separation height, the time-averaged temperature was found to be 0.55. At this location the temperature fluctuates almost the entire temperature range in the cavity (between dimensionless temperatures of 0.05 and 0.98). In dimensional terms, this corresponds to temperature fluctuations between 23.3 and 42.1 °C. This large fluctuation is due to the oscillations in the separation height as observed in the flow visualization. When the separation location oscillates below the thermocouple, the thermocouples detects relatively cool water as described in the preceding paragraph. However, when the separation location moves above the thermocouple, the thermocouple detects hot water as will be described in the next paragraph.

Below the separation height, the time-averaged temperature was 0.79 and the temperature fluctuates between 0.55 and 1. The temperature of the water is high in this region as the fluid is recirculating in a counter clockwise cell adjacent to the heated wall. Cooling of this cell is due to the interaction of this cell with the downward flowing warm water after it separates from the heated wall.

Fast fourier transforms of several typical thermocouple outputs were performed. The results of the FFT analysis suggests that no specific frequencies were found to be dominant in the temperature traces.

For each of the cases, the temperature profiles at three heights are shown in Figure 7.13. For all cases the thermal boundary layer is approximately 3 mm thick. The temperature gradient at the wall was highest for case 4. Outside of the boundary layer, case 2 shows a slight temperature dependence on height. For this case the lower the measurement location, the higher

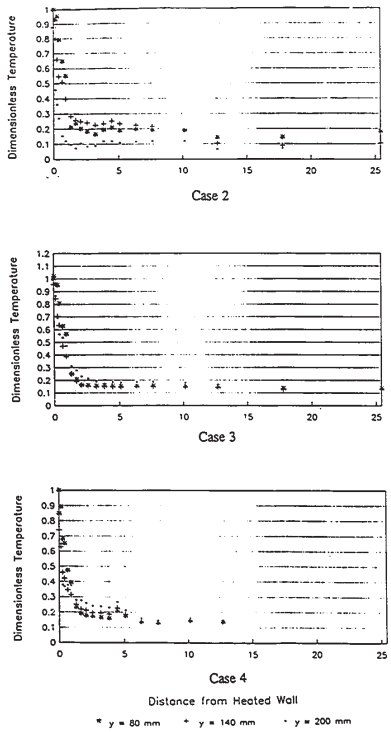


**Figure 7.13: Horizontal Temperature Profiles**



the temperature. This observation is consistent with the flow field as shown by comparison of the 80 and 200 mm height profiles. At the 80 mm height, the profile height is below the separation location and the liquid is warm because it is in the buoyancy dominated recirculation region. In addition, the temperature gradient at the wall is lower at this height because the difference between the isothermal wall temperature and the local bulk fluid temperature is small resulting in a lower heat flux. The profile at the 200 mm height is above the separation location and the fluid is colder adjacent to wall because the fluid motion is driven by the cold inlet jet. Since the temperature difference between the wall and local bulk temperature is higher, the heat flux in this location is higher resulting in a steeper temperature gradient at the wall.

In cases 3 and 4, the temperature outside of the boundary layer is independent of height as all the profiles become asymptotic to a dimensionless temperature of approximately 0.15. The measurements at the three elevations are similar because they are all in the buoyancy dominated region.

The temperature profiles along the vertical centreline are shown in Figure 7.14. At heights greater than 8 cm, case 2 and case 3 have almost identical profiles but differ below this height. Comparison of Figures 7.7(b) and 7.8(b) shows a difference in the size and shape of the counter clockwise cell in the bottom corner for these cases. In case 2 the cell is shorter but is wider then the cell in case 3. The cell extends beyond the vertical centreline in case 2 but it roughly ends at the vertical centreline in case 3. Since this cell is in contact with the heated wall, the fluid in the cell would be at an elevated temperature. Thus the temperature profile below a height of 8 cm should be higher for case 2. The temperature profile for case 4 has a similar slope as the other cases but is offset by 0.1 dimensionless temperature units. This elevated temperature is due to the fact that the buoyancy driven counter clockwise cell occupies the entire



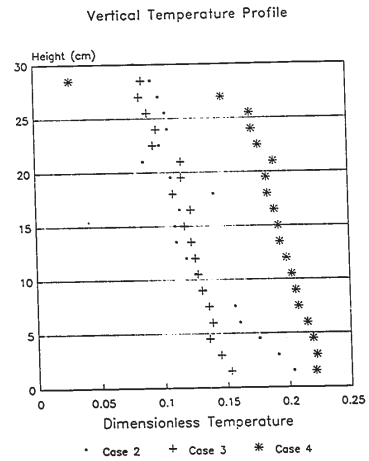


**Figure 7.14: Vertical Temperature Profile**



height of the cavity.

## 7.3 Verification of the Computer Code

Since there are no detailed studies of turbulent mixed convection in rectangular enclosures, verification of the current computer program is accomplished by studying different aspects of the program. Three case studies are modelled. These include laminar natural convection, laminar mixed convection, and turbulent natural convection. These case studies are described in detail in sections 7.3.1 to 7.3.3. For all of the numerical predictions presented in this chapter, a solution is assumed to be converged if the sum of the temperature residuals is less than $10^{-6}$ and the sum of the residuals for each of the other variables is less than $10^{-3}$.

### 7.3.1 Verification Study 1-Laminar Natural Convection

The first verification study is laminar natural convection in a right vertical square cavity. This study is shown schematically in Figure 2.2 and has been discussed in section 2.2.3 of the present work. This is a relevant study as natural convection may be considered a limiting case of mixed convection and Ostrach [16] states that this type of cavity contains all of the physics relevant to all confined natural convection problems. The specific problem described by de Vahl Davis and Jones [19,20] was selected for a test case as accurate solutions are available in the form of a bench mark solution. The motivation for providing the bench mark solution was to have something to compare with for the validation of computer programs.

Although contributions for Rayleigh numbers of $10^3$, $10^4$, $10^5$, and $10^6$ were requested, only two cases are shown in the present verification. The cases considered are Rayleigh numbers of $10^3$ and $10^6$. These cases were selected as the mechanism for heat transfer is dominated by

conduction in the low Rayleigh number case (isotherms are nearly vertical) while the high Rayleigh number case is dominated by convection. The cavity aspect ratio is 1 and the fluid Prandtl number is 0.71 which corresponds to air.

The contour plots of stream function, horizontal velocity, vertical velocity, and temperature, for both the present work and the bench mark solution, are presented in Figures 7.15 to 7.18. The streamline plots are not labelled as the purpose of these plots is to show the overall flow patterns in the cavity. The remaining contour plots are not labelled but the contour values are equally spaced. As an example, the temperature contours in Figure 7.18 may be written as

$$\theta = 0(0.1)1 \tag{7.2}$$

This indicates that the minimum contour value (at the right wall) has a value of 0 and the maximum contour value (at the left wall) has a value of 1. The remaining contours are presented in increments of 0.1. Comparison of the contours suggest that, qualitatively, the present work has excellent agreement with the bench mark solution. In addition, the temperature and velocity fields appear to be consistent with each other. A complete discussion on this topic and on the flow field may be found in reference [84].

A summary of the important flow variables is presented in Table 7.4. These flow variables are the maximum horizontal velocity on the vertical midplane and its location, the maximum vertical velocity on the horizontal midplane and its location, the average Nusselt number on the heated wall and the maximum and minimum Nusselt numbers on the heated wall and their locations. The variables are in dimensionless form as described by reference [19].



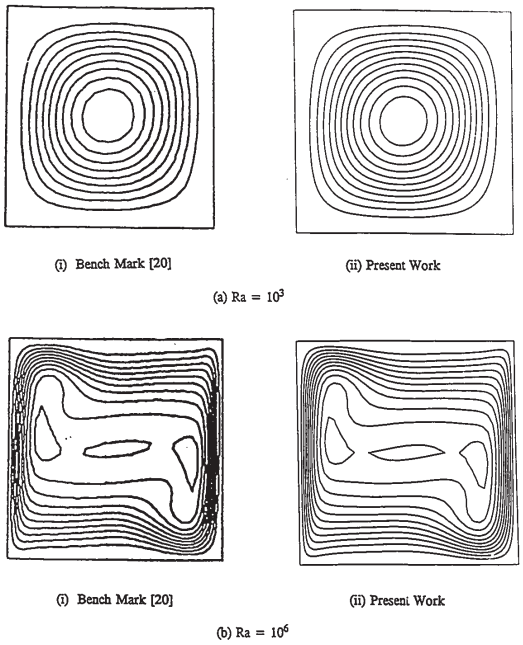

(i) Bench Mark [20] (ii) Present Work

(a) Ra = $10^3$

(i) Bench Mark [20] (ii) Present Work

(b) Ra = $10^6$

**Figure 7.15: Verification Study 1-Streamlines**



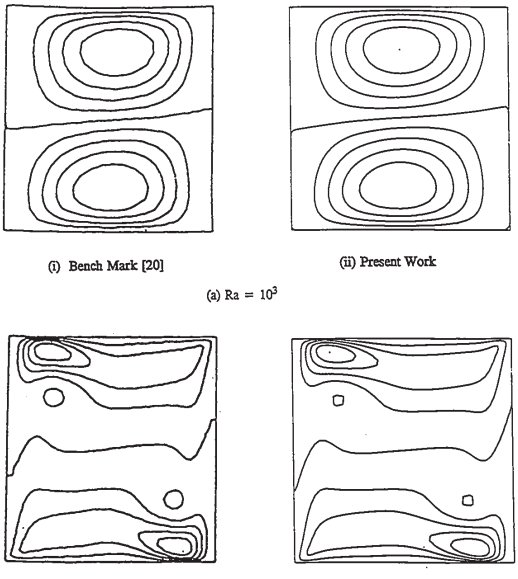

(i) Bench Mark [20] (ii) Present Work

(a) Ra = $10^3$

(i) Bench Mark [20] (ii) Present Work

(b) Ra = $10^6$

**Figure 7.16: Verification Study 1-U Velocity Contours**



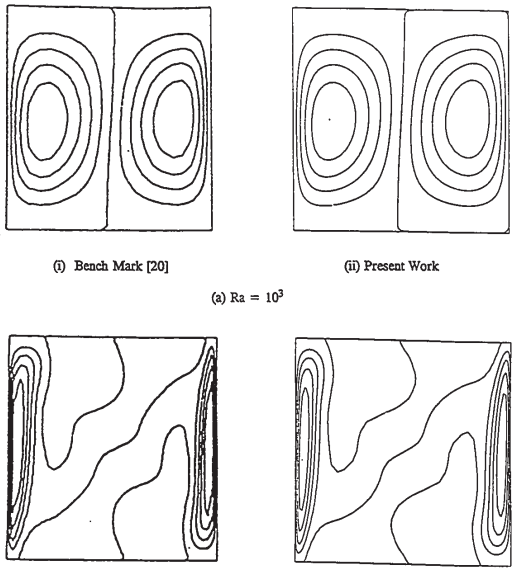

(i) Bench Mark [20] (ii) Present Work

(a) Ra = $10^3$

(i) Bench Mark [20] (ii) Present Work

(b) Ra = $10^6$

**Figure 7.17: Verification Study 1-V Velocity Contours**

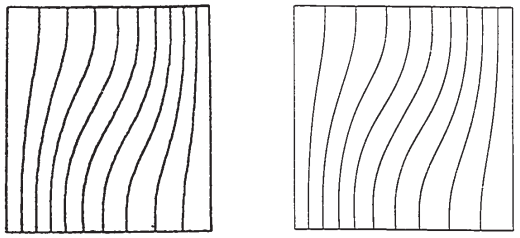

(i) Bench Mark [20] (ii) Present Work

(a) Ra = $10^3$

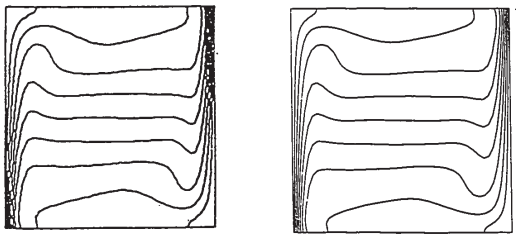

(i) Bench Mark [20] (ii) Present Work

(b) Ra = $10^6$

**Figure 7.18: Verification Study 1-Temperature Contours**



**Table 7.4: Verification Study 1-Summary of Important Flow Variables**

| Ra | $10^3$ | $10^3$ | $10^6$ | $10^6$ |
|---|---|---|---|---|
| | Bench Mark | Present Work | Bench Mark | Present Work |
| $U_{max}$ Y | 3.649 0.813 | 3.643 0.804 | 63.64 0.850 | 64.81 0.853 |
| $V_{max}$ X | 3.697 0.178 | 3.693 0.171 | 219.4 0.038 | 220.5 0.033 |
| Nu | 1.117 | 1.118 | 8.817 | 8.831 |
| $Nu_{max}$ Y | 1.505 0.092 | 1.507 0.083 | 17.93 0.039 | 17.78 0.033 |
| $Nu_{min}$ Y | 0.692 1.000 | 0.691 1.000 | 0.989 1.000 | 1.044 1.000 |

Small differences between the bench mark solution and the present work exist. Some difference is attributed to the method in which the maxima were determined. In the present work the maxima (and their position) are determined from the grid point values only while the bench mark used interpolation to obtain the maxima. This table indicates that agreement between the present work and the bench mark is good. However slight differences at $10^6$ suggest that a finer mesh may have to be used for better agreement at this Rayleigh number.

In both the table of important flow variables and the contour plots, the present predictions are excellent when compared with the bench mark solution. This would suggest that the computer code is capable of predicting laminar turbulent buoyant flow. In other words, the horizontal velocity, vertical velocity, pressure and temperature are coupled correctly. In addition the mathematical models for these variables and the numerical formulation are also adequate.



### 7.3.2 Verification Case Study 2-Laminar Mixed Convection

The fluid motion in the preceding case study is due solely to buoyancy. However, in mixed convection problems the fluid motion is due to a combination of inertia and buoyancy. In addition, the inlet and outlet boundary conditions must also be tested. The second verification problem is laminar mixed convection in a rectangular enclosure.

The problem is shown schematically in Figure 7.19 and may be described as a vertical rectangular cavity. The horizontal walls are adiabatic and the left and right walls are maintained at $T_C$ and $T_H$ respectively. The fluid enters the cavity horizontally at the bottom left corner and leaves the cavity horizontally at the upper left corner. Oosthuizen and Paul [9] modelled this flow using a finite element stream function-vorticity formulation.

Three cases are considered for comparison. These cases are summarized in Figure 7.19 and have an aspect ratio of 2 and Richardson numbers of 0, 1 and 10 which are comparable to cases 1, 2 and 3 of the present work.

Streamlines are shown in Figure 7.20. For each case, the streamline legend corresponds to both the prediction of Oosthuizen and Paul [9] and the present prediction. Overall, the present solutions compare well with the previously published solutions. The streamlines of the present work are smoother than the contours of Oosthuizen and Paul. This difference is likely attributed to the difference in mesh size. In the present work, the results of a 45 by 45 mesh are presented. Solutions obtained with a 21 by 21 grid yielded almost identical solutions to the published solutions. The present solution predicts a small clockwise rotating cell in the upper right hand corner of the cavity which is not predicted by Oosthuizen and Paul [9]. This difference is also attributed to the difference in mesh size as a coarse mesh is unable to resolve this cell.



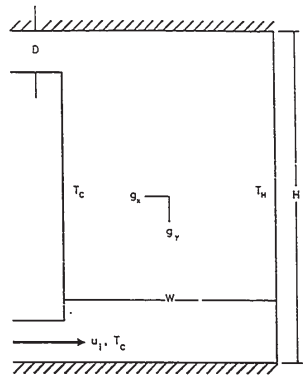


$$Gr = \frac{g\beta(T_H - T_C)H^3}{\nu^2} = 0, -10^4, -10^5$$

$$Re = \frac{u_i H}{\nu} = 100$$

$$Pr = \frac{\nu}{\alpha} = 0.7$$

$$A = \frac{H}{W} = 2$$

$$a = \frac{D}{H} = 0.2$$

**Figure 7.19: Verification Study 2-Laminar Mixed Convection**

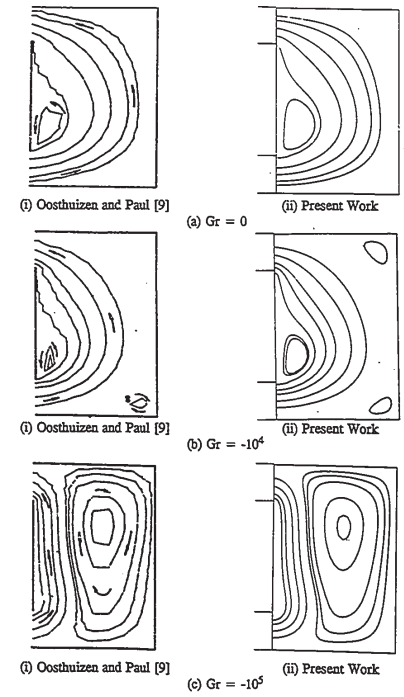


**Figure 7.20: Verification Study 2-Streamlines**



In both predictions, the flow is buoyancy dominated at a Grashof number of $-10^5$ (see Figure 7.20 (c)) which corresponds to a Richardson number of 10. This buoyancy domination is not observed in the lower Richardson numbers cases.

The present computer code is compared with a completely independent computer code based on different mathematical variables (stream function-vorticity) and a different numerical formulation (finite elements). The present predictions compare well with the predictions of Oosthuizen and Paul [9]. The differences in the flow field have been discussed and are attributed to differences in mesh size. This verification study suggests that the present code is capable of predicting laminar flow with both interia and buoyant forces present. In addition, the inlet and outlet boundary conditions appear to be modelled correctly.

### 7.3.3 Verification Case Study 3-Turbulent Natural Convection in an Enclosure

In the preceding two verification cases the flow was assumed to be laminar. In this case a turbulent flow is modelled. The cavity is similar to the first verification case (see Figure 2.2). However, for this case the aspect ratio is 5, the Rayleigh number is $4X10^{10}$ and the Prandtl number corresponds to air. The case was studied experimentally by Cheesewright et. al. [52] and computationally by Davidson [42,53]. In all of the figures of this section the data points correspond to the experimental results of Cheesewright [52], the solid line corresponds to the predictions of Davidson [42] and the dotted lines corresponds to the present predictions.

The vertical velocity profile along the horizontal centreline is presented in Figure 7.21. The present solutions have good agreement with both the experimental results and the predictions of Davidson. The present solutions are symmetric while the experimental data and the predictions of Davidson are asymmetric. This difference is due to variation of the thermophysical



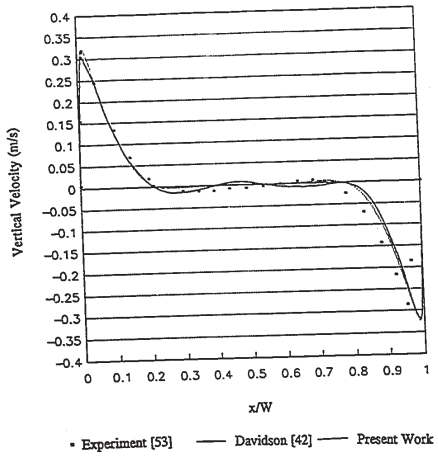


**Figure 7.21: Verification Study 3-Vertical Velocity Profile**



properties as the present model does not have a variable property model for air. In the core of the cavity, the experimental profile and the present profile are flat but the Davidson's predictions are sinusoidal. Davidson [42] attributes this to his overprediction of the strength of secondary vortices in the cavity.

The dimensionless temperature profile along the vertical centreline is presented in Figure 7.22. The present predictions agree well with the predictions of Davidson but differ from the experimental data. The predictions are symmetric as defined in equation 7.3

$$(1 - \theta)|_Y = \theta|_{(1-Y)} \qquad (7.3)$$

Davidson [42] attributes the asymmetry in the experimental data to heat losses through the side walls.

The heat flux profile along the vertical walls is shown in Figure 7.23. Both the present predictions and the predictions of Davidson agree well with the experimental data. At the hot wall, the experimental heat flux is slightly higher than the predicted heat fluxes. In contrast to this, the experimental heat flux is lower than the predicted heat fluxes at the cold wall. Davidson [42] attributes these differences to heat losses through the side walls of the experiment.

The profiles of turbulence parameters along the horizontal centreline is presented in Figure 7.24. As expected the present predictions are symmetric. The experimental data is skewed toward the heated wall and the predictions of Davidson are skewed toward the cold wall. For $x/W > 0.5$, the present predictions are in excellent agreement with the experimental data. In the core of the cavity, the present model prediction of the minimum turbulent fluctuation is comparable to the experimental data ($\sqrt{k} \approx 0.006$ m/s) while Davidson predicts higher turbulence levels in this region. Adjacent to the vertical walls, the predicted peak values are

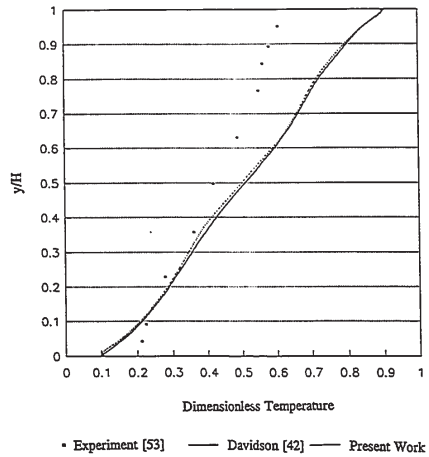


**Figure 7.22: Verification Study 3-Temperature Profile on Vertical Centreline**



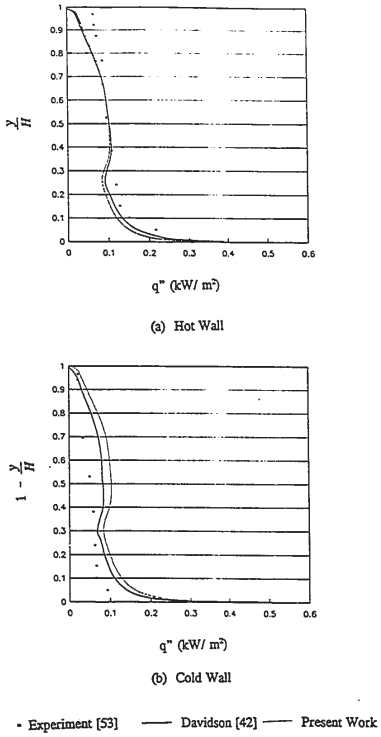


**Figure 7.23: Verification Study 3-Profiles of Heat Flux along the Vertical Walls**



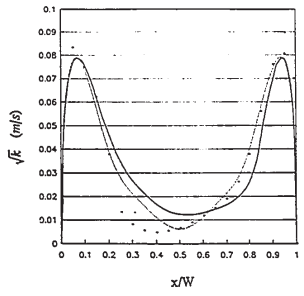


**Figure 7.24: Verification Study 3-Profiles of Turbulence Parameters on Horizontal Centreline**



slightly less than the experimental values. The profile of the damping function, $f_\mu$, along the horizontal midplane is shown in Figure 7.24 (b). For $x/W < 0.4$, the present predictions and the Davidson predictions are in excellent agreement. In the core of the cavity, Davidson's predictions differ from the present predictions. Close to the cold wall ($x/W > 0.9$) the predictions are also in excellent agreement. Tne differences are due to the variation of thermophysical properties. For the present predictions, a constant thermophysical property model is used and hence the solutions are symmetric. Davidson's predictions are based on a model which allows the fluid properties to vary with temperature and hence the profiles are asymmetric.

The profiles of turbulent viscosity at various cavity heights are shown in Figure 7.25. At all cavity heights the present predictions agree well with the predictions of Davidson. In general, the agreement is excellent close to the walls but the present model tends to predict a higher value of turbulent viscosity in the core region. This observation is explained by Figure 7.24(b). Adjacent to the walls, the predictions of $f_\mu$ is comparable, but in the core of the cavity the present prediction of $f_\mu$ is typically lower than Davidson's prediction. Comparison of Figures 7.25 (a) and 7.25 (d) show that the present solutions are again symmetric while the predictions of Davidson are asymmetric.

For the velocities, temperature and turbulence quantities, the present predictions agree well with both the experimental results of Cheesewright [52] and the predictions of Davidson [42]. The differences between the present predictions and the predictions of Davidson are most likely due to the variation of fluid properties. The experimental data differs from the predictions because of heat losses in the experiment. The results of this study suggest that the turbulence is modelled correctly and is coupled to the velocities, temperature and pressure fields properly. In addition, a low Reynolds number $k-\varepsilon$ model is adequate for buoyancy dominated flows.

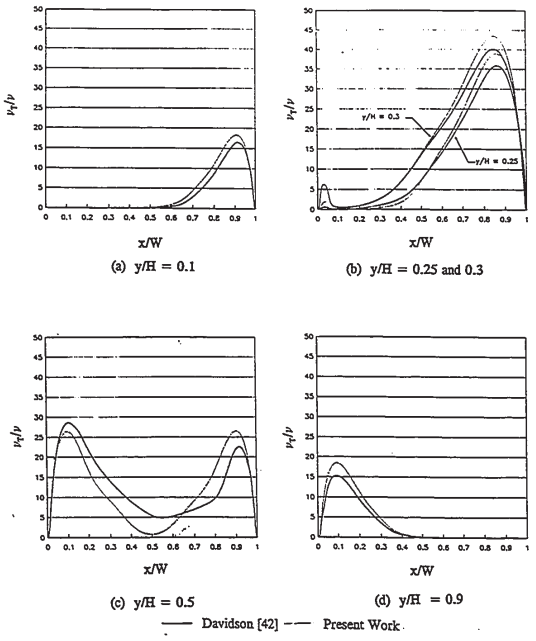


**Figure 7.25: Verification Study 3-Horizontal Profiles of Viscosity Ratio**



## 7.4 Preliminary Testing of the Code for Mixed Convective Flows

### 7.4.1 Introduction

In applying the computer code to the present problem of turbulent mixed convection in enclosures, different aspects of modelling have been considered. These include the effect of temperature on thermophysical properties and the validity of the Boussinesq approximation, QUICK differencing, the effect of different low Reynolds number k-ε turbulence models, and the inclusion of the Yap correction term. These aspects have been considered in sections 7.4.3 and 7.4.4.

The solution procedure described in Chapter 6 is iterative in nature and under-relaxation is implemented to minimize the chance of divergence [69]. The under-relaxation was implemented using the approach described by Patankar [69]. The discretization equation is written as

$$\phi_P = \phi_P^* + \alpha_R \left[ \frac{\sum a_{nb}\phi_{n_b} + b}{a_P} - \phi_P^* \right] \tag{7.4}$$

where $\alpha_R$ is the under-relaxation factor (a number between 0 and 1) and

$\phi_P^*$ is the value of $\phi_P$ from the previous iteration.

Solutions independent of initial conditions and the under-relaxation factor used in the iterative scheme have been obtained for all cases with the exception of case 2. In this case, two solutions were possible depending on the under-relaxation factor used for the velocities. If the velocity under-relaxation factors are greater than or equal to approximately 0.25, one solution was obtained with the predicted separation below the experimental separation location. For a velocity under-relaxation factor less than this value a second solution was obtained. This solution predicted the separation above the experimentally observed value. For two-dimensional natural



convection in a rectangular square cavity, Henkes et al. [55] state that nonunique solutions can be obtained in the laminar turbulent transitions. Although it is possible that nonunique solutions exist for this case, it is more likely that the solution scheme is unstable for high under-relaxation parameters. This conclusion is drawn from the fact that the predicted separation height (using high under-relaxation) for case 2 is lower than the predicted separation height for the isothermal case. Physically, this trend is not expected as discussed in sections 7.2.1 and 7.2.2. In addition, the solution obtained with the low under-relaxation factor is considered correct as it is consistent with the predictions for the other intermediate case (to be discussed in section 7.5.1).

### 7.4.2 Grid Independence Study

A grid independence test was completed on case 4 as this case has the steepest temperature gradient at the heated wall as shown in Figure 7.13. In addition, it is well known that the higher the Grashof number, a finer mesh is required to resolve the narrower boundary layers adjacent to the walls. Solutions have been obtained on 51 by 51, 61 by 61 and 81 by 81 grids for this case. The number of grid points refers to the number of grids within the cavity itself and the grid points in the developing lengths are not accounted for in these numbers. The grid spacing is nonuniform and uses a distribution of the form $x^n$. The distribution is given by Abrous [47] and is shown by equation 7.5.

$$\chi = \frac{(2x)^n}{2} \text{ for } x < 0.5$$
$$\chi = \left[ -(2-2x)^n + 2 \right]/2 \text{ for } x \geq 0.5 \tag{7.5}$$



where x is the grid location based on a uniform grid,

n is the grid exponent and

$\chi$ is the grid location based on a non uniform grid.

If the exponent, n, is equal to unity a uniform grid is generated. As the value of n is increased, the number of nodes in the vicinity of the wall is increased and the number of nodes in the core of the cavity is decreased. Additional grid points are also inserted adjacent to the heated wall to resolve the steep temperature gradient in this vicinity.

For all of the grids, the vertical velocity and temperature profiles along the horizontal midplane are presented in Figures 7.26 and 7.27 respectively. In the velocity boundary layers, the width and peak velocities for the 51X51 grid differ considerably from the 61X61 and 81X81 grids. In the core of the cavity, all of the computational meshes predict the flow to be nearly stagnant. The core temperature for the 51X51 grid differs from the other grids.

The horizontal component of velocity and temperature profiles along the vertical centreline is presented in Figures 7.28 and 7.29 respectively. These figures also show the 61X61 and 81X81 grids to give almost identical predictions while the 51X51 grid gives significantly different predictions.

The profiles shown in Figures 7.26 to 7.29 suggest that nearly grid independent solutions are obtained for the 61X61 grid. The velocity and temperature gradients at the heated wall are important as this is the only boundary at which heat is transferred to the fluid. In order to model the flow adequately, it is important that there are enough computational nodes in this region. For the 61X61 grid used in Figures 7.26 and 7.27, there are approximately 13 computational nodes between the heated wall and the peak velocity of the boundary layer. For the temperature profile, there are approximately 10 computational nodes in the nearly vertical portion of thermal boundary

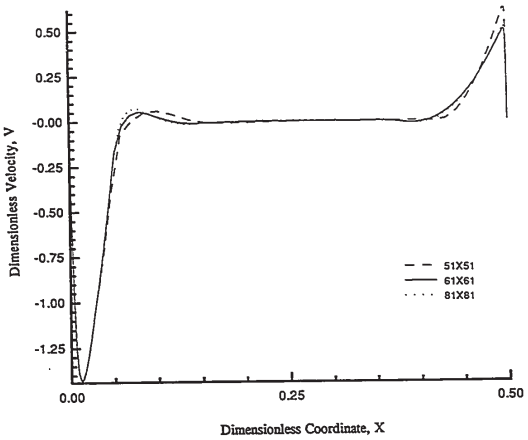


Figure 7.26: Grid Dependence Study-Vertical Velocity Profile along Horizontal Centreline



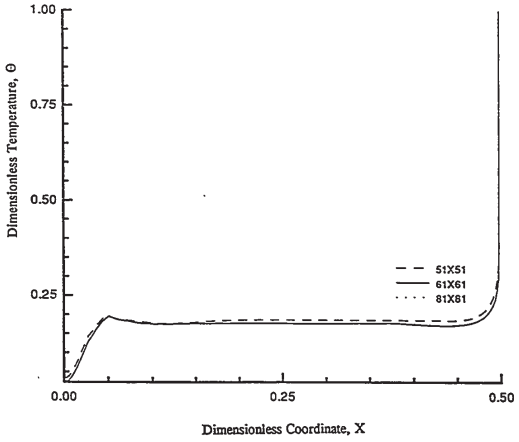


Figure 7.27: Grid Dependence Study-Temperature Profile along Horizontal Centreline



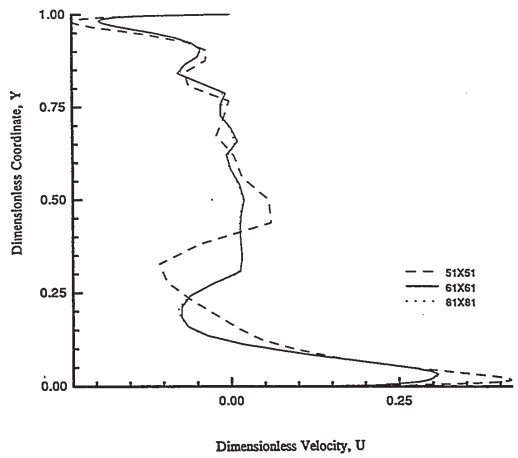


Figure 7.28: Grid Dependence Study-Horizontal Velocity Profile along Vertical Centreline



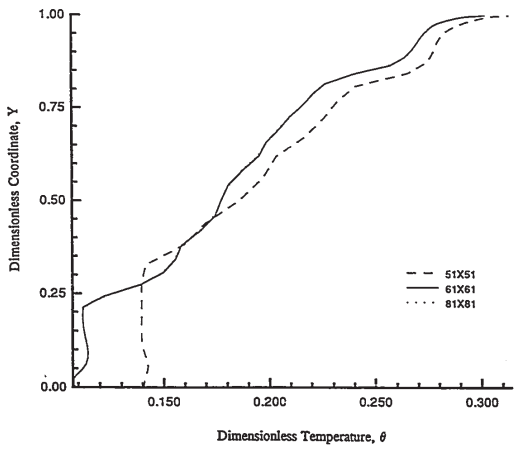


Figure 7.29: Grid Dependence Study-Temperature Profile along Vertical Centreline

layer adjacent to the heated wall. With this number of nodes, the steep gradients in this region should be adequately resolved.

The identical grid was used to obtain a solution for the third verification study. This study had a Grashof number based on the height of the enclosure of approximately $6X10^{10}$ which is larger than the Grashof number for any of the cases in the present work. Since the flow field in the verification study has similar relevant physics and the solutions obtained are in excellent agreement with experimental results and independent predictions, it would suggest that the grid is adequate for predicting the present cases.

### 7.4.3 Turbulence Model Study

For cases 1, 2 and 3 results have been obtained using a laminar flow model, a modified form of the Jones and Launder model [41] and a modified form of the Lam and Bremhorst model [42]. In addition, the commercial computational package FLUENT has been used to predict the results with a standard k-ε model with wall functions. Refer to section 7.5.2 for a complete discussion of the predictions of FLUENT.

For case 2, the vertical velocity component along the horizontal midplane is presented in Figure 7.30. Adjacent to the heated wall, the laminar flow model predicts the peak velocity well but the boundary layer is too thick resulting in the peak velocity being too far from the wall. As expected the boundary layers predicted by both turbulence models are narrower than the laminar prediction. These models also predict the peak velocity to be much higher than the experimental results. In the core region of the cavity, both the modified forms of the Jones and Launder model [41] and the Lam and Bremhorst model [42] predict the flow close to the experimental data while the laminar model predicts the velocity too low. Adjacent to the



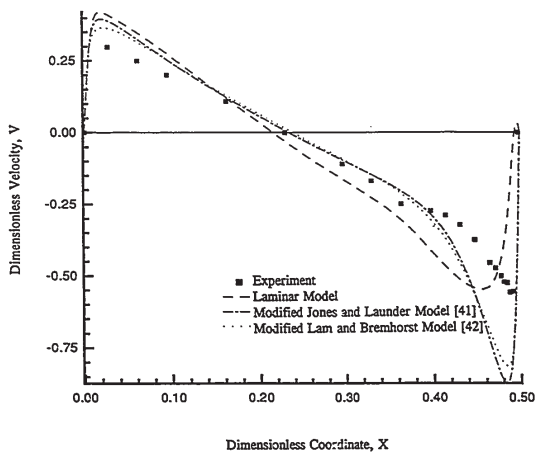


**Figure 7.30: Turbulence Model Study-Vertical Velocity Profile along Horizontal Centreline**



insulated vertical wall, all three models slightly overpredict the peak velocity. However, the width and shape of the predictions at this boundary are reasonably close to the measured boundary layer.

The horizontal component of velocity along the vertical midplane is shown in Figure 7.31. In this plane, the laminar model predicts the peak velocity of the inlet jet well but the boundary layer is wider than the measurement. Both of the turbulence models overpredict the maximum jet velocity and underpredict the boundary layer thickness. In the core region of the cavity, the turbulence models have good agreement with the experimental data. The laminar model has poor prediction in this region as the shape of the profile is considerably different from the experimental points. At the bottom of the cavity both the turbulence models overpredict the fluid velocity but are similar in shape to the measurements. In this region the laminar flow model has poor agreement with the experiment as this model predicts positive values of velocity at the bottom of the cavity while the measurements show the velocities to be negative. In other words the laminar model is predicting the counter clockwise rotating cell at the bottom of the cavity to be too wide.

The laminar model adequately predicts the peak velocity in the boundary layers along the heated wall and at the top of the cavity. However, it predicts these boundary layers to be too wide and has poor agreement in the core of the cavity and at the bottom of the cavity. Qualitatively, the performance of both turbulence models were comparable. However the modified Lam and Bremhorst model [42] gave slightly better predictions in the boundary layers forming on the left, right and bottom walls. For cases 1 and 3, the modified form of the Lam and Bremhorst model [42] also gave slightly better predictions than the modified form of the Jones and Launder model [41]. This study suggests that the laminar model is inadequate and the



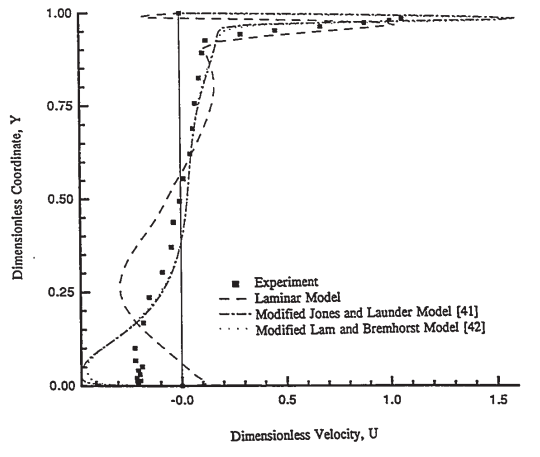


**Figure 7.31: Turbulence Model Study-Horizontal Velocity Profile along Vertical Centreline**

modified Lam and Bremhorst low Reynolds number model has slightly better agreement than the modified Jones and Launder model when applied to mixed convective flows. The modified Lam and Bremhorst model has been used for all remaining low Reynolds number turbulence model simulations.

### 7.4.4 Secondary Model Study

The selection and use of secondary models for the prediction of fluid flow and heat transfer is problem dependent. The use of these models may enhance the predictions and thus it is important to study which models have an effect on the predictions for this particular class of flow problems. In the present work, the effects of a variable property model for the fluid properties, a variable $\sigma_T$ model, the use of QUICK differencing and the use of the Yap correction have been studied to determine the effect of these models on this class of flow.

The effect of temperature on the thermophysical properties of water has been investigated. The properties of water are given by equations 5.49 to 5.53. For the constant property model, the reference fluid properties are evaluated at a dimensionless temperature of 0.5 and a solution is obtained using these properties throughout the cavity. However, some of these properties are strongly dependent on temperature. The variation of these thermophysical properties with temperature is shown graphically in Figure 7.32. The vertical axis on this figure is the percentage change from the reference property and is calculated from

$$\% \text{ Change from Reference} = \frac{\phi|_\theta - \phi|_{REF}}{\phi|_\theta} \qquad (7.6)$$

where $\phi|_\theta$ is a fluid property evaluated at a dimensionless temperature, $\theta$, and

$\phi|_{REF}$ is the same fluid property evaluated at the reference temperature (equation 5.5)



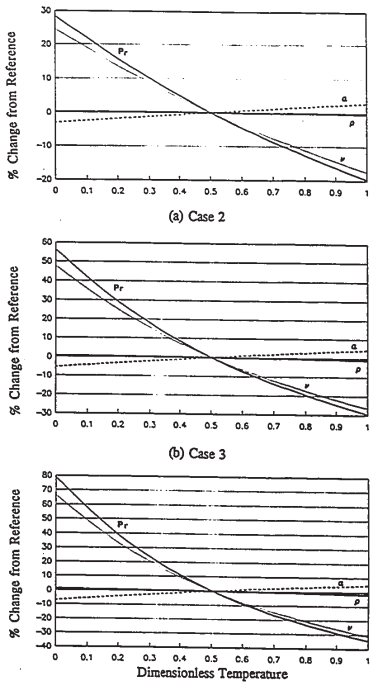


**Figure 7.32: Variation of Thermophysical Properties**



The fluid density is almost a constant and the thermal diffusivity is only a weak function of temperature. The kinematic viscosity and Prandtl number are strongly dependent on temperature as these properties differ from the reference value by up to 75% and 80% respectively.

The dimensionless buoyancy source term (in the V momentum equation) is also presented as a function of temperature in Figure 7.33. The narrow solid line refers to the Boussinesq approximation. This approximation assumes the buoyancy term in the momentum equation to vary linearly with temperature as shown by a straight line in this figure. In all of the cases, the variation is not linear as shown by the nonlinear curves. At both low and high temperatures, the buoyancy term in the momentum equations is higher than predicted by the Boussinesq approximation. At a dimensionless temperature of 0.5, the buoyancy source term is zero for the Boussinesq approximation and for the nonlinear calculation. The Boussinesq approximation has the best agreement for this source term for case 2 and the worst agreement for case 4. As expected, the higher the difference between the wall and jet temperatures, the worse the estimation when using the Boussinesq approximation.

These figures suggest the use of a variable fluid property model may be required to model the flow. The use of this model and the models presented in the introductory paragraph of this section have been investigated in the present work. A brief summary of the other models tested is presented.

As discussed in section 5.5, Kays and Crawford [67] state the turbulent Prandtl number, $\sigma_T$, is large adjacent to a boundary and decreases asymptotically to a value of about unity in the law of the wall region. This suggests the momentum diffusion is greater than the heat diffusion near the wall. Thus the rate of heat transfer may be slightly inhibited in this region using this model.



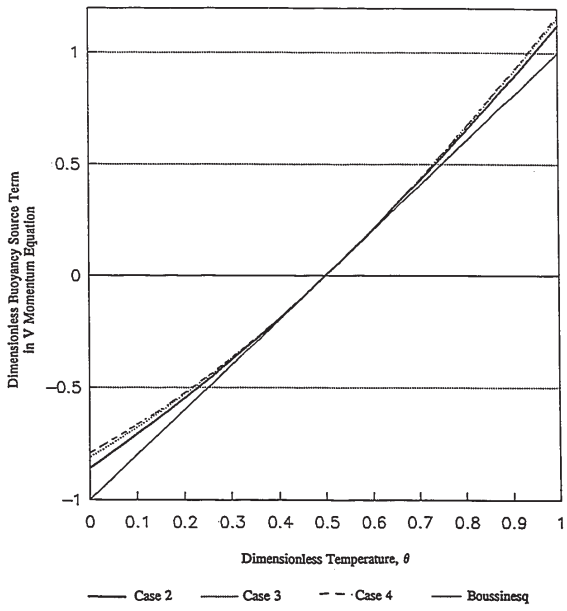


**Figure 7.33: Variation of Dimensionless Buoyancy Term**

As shown in Figures 7.2 to 7.6, the flow field is skewed to the computational grid in many areas in the flow domain. With this skewed flow, numerical diffusion may be introduced into the calculations. In an effort to reduce this numerical diffusion, QUICK differencing [75] is incorporated in the present computer code as described in section 6.4. This differencing technique has been incorporated in the momentum and energy equations and neglected in the turbulent kinetic energy and dissipation of turbulent kinetic energy equations as this differencing scheme often leads to overshoots in peak values [77]. Solutions have been obtained using either the hybrid scheme or QUICK differencing for the momentum and energy equations.

Ince and Launder [44] suggest the addition of the "Yap" source term to the conservation of dissipation of turbulent kinetic energy equation. For separating and reattaching flows the predicted heat transfer rates in this vicinity have been found to be inconsistent with experimental results when using a low Reynolds number turbulence model. Yap suggests, the addition of equation 2.54 to the dissipation of turbulent kinetic energy equation brings the heat transfer coefficient comparable to experimental results. The use of this term is also studied in the present work.

In the computer code, each of these secondary models can be turned off or on. A detailed study has been completed to determine which models have an effect on the flow. For case 3, a solution has been obtained with all of these secondary models turned off. Using this solution for initial conditions, a solution was then obtained with the variable fluid property model switched on and the remaining models turned off. This procedure was repeated for each of the secondary models. A final solution was obtained with all of the models switched on. None of the models significantly affected the overall flow field or the location of flow separation on the



heated wall. The effect of each of the models is discussed with respect to velocity profiles along the centrelines of the cavity.

The vertical component of velocity along the horizontal centreline is shown in Figure 7.34. The legend for the figures in this section is shown in Table 7.5.

**Table 7.5: Summary of Secondary Models**

| Legend Number | Variable Property Model | Variable $\sigma_T$ Model | QUICK Differencing | Yap Correction | Symbol or Line |
|---|---|---|---|---|---|
| 1 | Off | Off | Off | Off | ——— |
| 2 | On | Off | Off | Off | △ |
| 3 | On | On | Off | Off | ◇ |
| 4 | Off | Off | On | Off | ▽ |
| 5 | Off | Off | Off | On | ○ |
| 6 | On | On | On | On | — — |

Although it is a standard convention to use symbols for experimental data and lines for computational or theoretical results, symbols have been used for some of the predictions for clarity as some of the profiles coincide. Thus hollow symbols have been used for some of the predictions.

In this figure, the solid line corresponds to prediction of the basic model with all of the secondary models switched off. The profile is significantly affected by the variable property model as shown by the triangles. Adjacent to the vertical walls, the magnitude of the peak velocity is lower with inclusion of this model. The diamonds correspond to a model that incorporates both the variable property and variable turbulent Prandtl number secondary models.



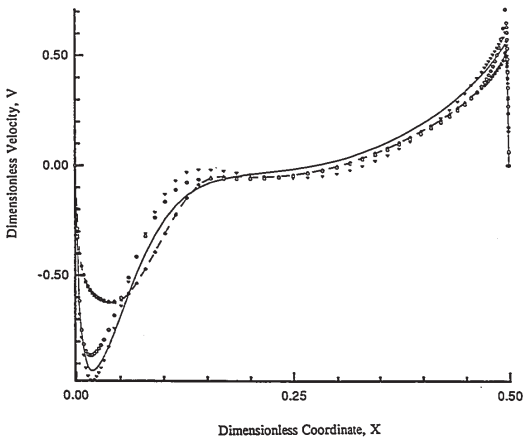


**Figure 7.34: Secondary Model Study-Vertical Velocity along Horizontal Centreline**



Since the triangles and the diamonds almost exactly coincide, this model offers no significant improvement over the variable property model. This suggests that the variable $\sigma_T$ model has little effect on the predicted flow field. The inverted triangles correspond to a model that incorporates only the QUICK differencing secondary model. As expected, this model overemphasizes the peak velocities in the boundary layers adjacent to the vertical walls. A model that includes only the Yap correction is shown by circles on this figure. This profile differs from the basic model slightly but not to the same extent as the variable property model. This model accentuates buoyancy as the peak velocity adjacent to the heated boundary is larger than the other models. The dashed line corresponds to a model that includes all of the secondary models. Since this line appears to almost exactly coincide with the triangles, it suggests that the variable property model has the largest effect on the predicted flow field.

The horizontal component of velocity along the vertical centreline is shown in Figure 7.35. All of the models slightly change the predicted profile of horizontal velocity. A discussion similar to that for the vertical velocity could be formulated from this figure but is neglected for the sake of brevity.

As previously mentioned, none of the models had a significant effect on the prediction of the overall flow field or the location of separation. The variable property model altered the flow the most. While none of the models adequately predicted the flow, the intent of this section was to determine which secondary models has the greatest influence on the predictions. Reasons for the discrepancy between the predicted and the measured profiles will be discussed in section 7.6.

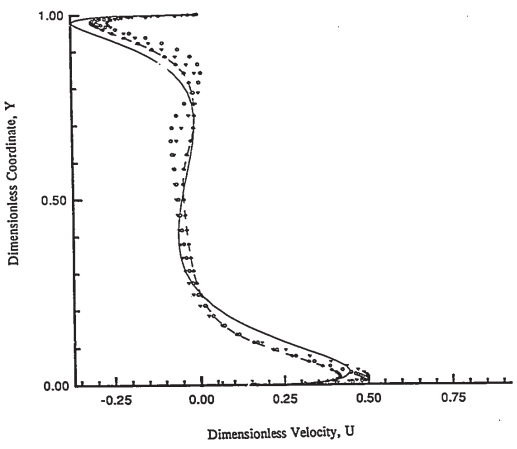


Figure 7.35: Secondary Model Study-Horizontal Velocity along Vertical Centreline



## 7.5 Numerical Predictions of Turbulent Mixed Convection Cavity Flows

### 7.5.1 Low Reynolds Number Turbulence Model Predictions

For all of the predictions presented in this section, all of the secondary models discussed in the previous section were included in the calculations. The velocity vector prediction for case 1 is presented in Figure 7.36. The predicted flow regime is separated flow (see Figure 7.1) as the bulk of the flow is in a large clockwise rotating cell. Two small counterclockwise cells are observed in the corners adjacent to the heated wall. The predicted separation height is 0.31 dimensionless units.

The prediction for case 2 is shown in Figure 7.37. The flow regime is also separated flow but the buoyancy in the cavity is increased compared to case 1 as shown by the large counterclockwise rotating cell in the bottom half of the cavity. The clockwise rotating cell is reduced in size to approximately the upper half of the cavity. The changing sizes of these cells moves the predicted dimensionless separation height to 0.76 dimensionless units up the heated wall.

The predicted velocity vectors for case 3 are shown in Figure 7.38. This flow regime is referred to as buoyancy dominated flow as the flow in the cavity is dominated by a large counterclockwise cell. As described in section 7.2.1, the change to this flow regime is due to the growth of the buoyancy driven cell in the bottom of the cavity. This cell grows large enough to encompass nearly the entire cavity. The inertially driven clockwise rotating cell is reduced in size and is observed just below the entrance of the cavity. The predicted penetration depth of 0.025 dimensionless units.

The velocity vector prediction for case 4 is shown in Figure 7.39. The flow regime is also buoyancy dominated flow and the buoyancy driven cell is stronger than in the preceding



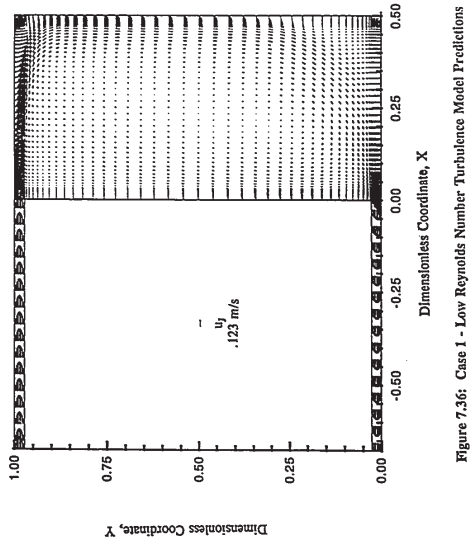


Figure 7.36: Case 1 - Low Reynolds Number Turbulence Model Predictions



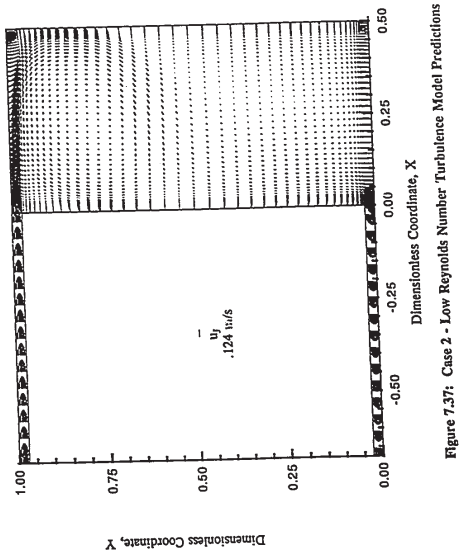


Figure 7.37: Case 2 - Low Reynolds Number Turbulence Model Predictions

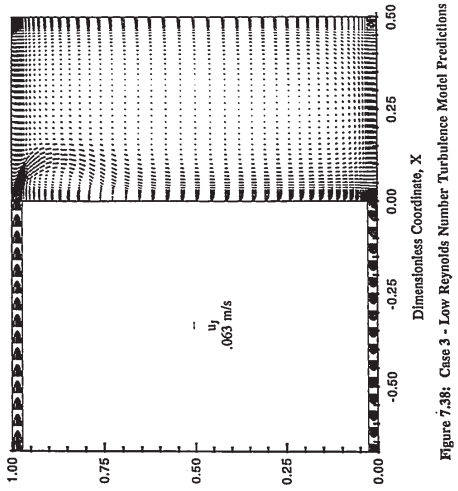


Figure 7.38: Case 3 - Low Reynolds Number Turbulence Model Predictions



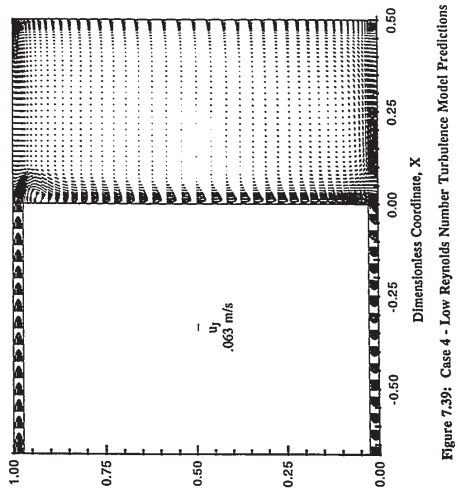


Figure 7.39: Case 4 - Low Reynolds Number Turbulence Model Predictions



case. The velocity in the boundary layer adjacent to the adiabatic vertical wall is much higher and the boundary layer is thinner in this case. The maximum penetration of the inlet jet into the cavity is approximately 0.08 units for this case and 0.15 units for case 3. It must be noted that the fluid separates on the top wall at X = 0.025 for both cases.

A summary of the dimensionless separation locations for the present predictions is presented in Table 7.6.

Table 7.6: Summary of Dimensionless Separation Locations for the Low Reynolds Number Turbulence Model

| Case | $Y_{sep}$ | $X_{pen}$ |
|---|---|---|
| 1 | 0.31 | - |
| 2 | 0.76 | - |
| 3 | - | 0.025 |
| 4 | - | 0.025 |

### 7.5.2 FLUENT Predictions

For all cases considered, solutions are obtained with the commercial computational fluid dynamics package, FLUENT [63]. This analysis allows the two-dimensionality of the flow to be studied as both two-dimensional and three-dimensional solutions can be obtained with this package. In addition, the effect of turbulence modelling can be investigated as a standard k-ε turbulence model with wall functions is used in the FLUENT software.

For the two-dimensional cases, the computational domain and grid are nearly identical to the predictions of section 7.5.1. Since the FLUENT package uses wall functions, the grid



points adjacent to the solid boundaries were placed in the logarithmic region. For the three-dimensional case, a solution is obtained for one half of the cavity, more specifically from the centreline of the cavity (Z = 0) to one of the faces. Along the centreline of the cavity, a plane of symmetry is specified as a boundary condition. In this plane the component of velocity in the Z direction is set to zero and the gradient of all the other variables is set to zero. Along the face of the cavity a no slip boundary is prescribed for the velocities and turbulence variables and an isothermal boundary condition is prescribed for the energy equation.

The two-dimensional solution for case 1 is presented in Figure 7.40. The flow field is similar to the predicted flow field in section 7.5.1 and the experiment as the flow is dominated by one large clockwise rotating cell due to inertia. The small counter clockwise rotating cells are also predicted in the corners adjacent to the heated boundary. For this case the predicted separation height is approximately 0.3 dimensionless units.

The two-dimensional FLUENT predictions for case 2 are shown in Figure 7.41. The overall flow field is similar to the previous case except the counterclockwise rotating cells have increased in size and the separation height is 0.5 dimensionless units.

Figure 7.42 shows the two-dimensional predictions for case 3. For this case, the flow is predicted to be dominated by buoyancy as the bulk of the flow is rotating counterclockwise. A small clockwise rotating cell is predicted below the entrance. The penetration depth is predicted to be 0.035 dimensionless units into the cavity.

The two-dimensional FLUENT predictions for case 4 is shown in Figure 7.43. FLUENT predicts the flow to be nearly identical to the previous case. The main difference is the size of the inertially driven cell below the entrance. This cell is slightly smaller in the present case. The dimensionless penetration depth is 0.025 for this case.

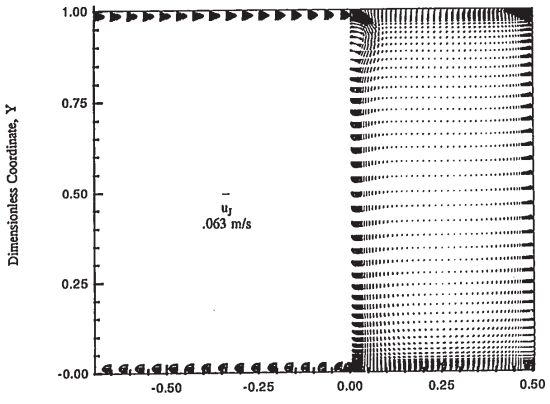


Figure 7.40: Case 1 - FLUENT Two Dimensional Prediction



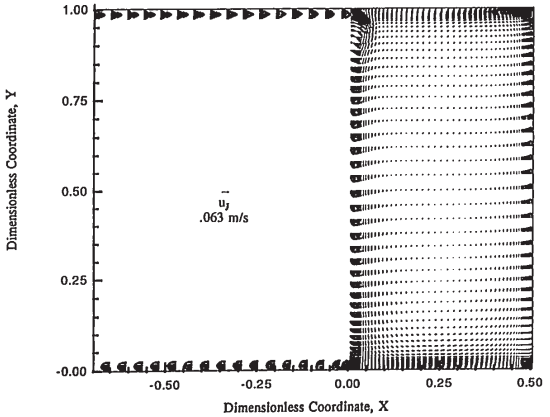


Figure 7.41: Case 2 - FLUENT Two Dimensional Prediction






Figure 7.42: Case 3 - FLUENT Two Dimensional Prediction






Figure 7.43: Case 4 - FLUENT Two Dimensional Prediction

Three-dimensional FLUENT predictions are presented for each of the cases in Figures 7.44 to 7.47. The velocity vectors are presented in a similar format as the experimental results. More specifically, velocity vectors are shown in the inlet plane, the plane of symmetry, the wall plane and the exit plane. The definition of these planes has been presented in the introductory paragraph of section 7.2.2. One difference between these figures and the figures showing the experimental results is that in the former, two components of velocity are plotted in all of the planes while in the latter only the dominant component of velocity is plotted in the inlet, wall and exit planes (W component of velocity is set to zero for the experimental vector plots). In general, the three-dimensional predictions are qualitatively similar to the two-dimensional predictions in the plane of symmetry. Thus the discussion for the three-dimensional results will be limited to the inlet, wall and exit planes. However, if there is a significant difference between the two and three-dimensional results, the discussion will include the plane of symmetry.

The predictions for case 1 are presented in Figure 7.44. For the FLUENT predictions, the horizontal component of velocity at the entrance of the inlet developing length is prescribed to have a uniform distribution (in the Z direction). The velocity vectors in the inlet developing length show the boundary layer to be fully developed by the third or fourth computational grid into the channel ($X \approx -0.6$). In the fully developed region of the inlet channel ($X \geq -0.6$), the velocity profile is uniform for Z less than approximately 0.07. The inlet plane also shows a region of backflow adjacent to the heated wall. As the inlet jet approaches the heated wall, the faster moving fluid at the plane of symmetry turns both downward and toward the face of the cavity. Thus, the region of backflow is smaller at the plane of symmetry ($Z = 0$) and is larger as the face of the cavity is approached.



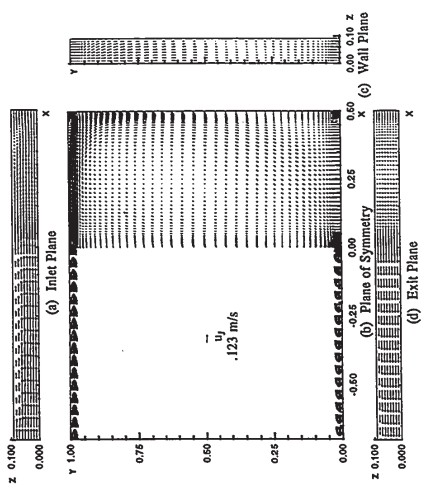


Figure 7.44: Case 1 - FLUENT Three Dimensional Prediction



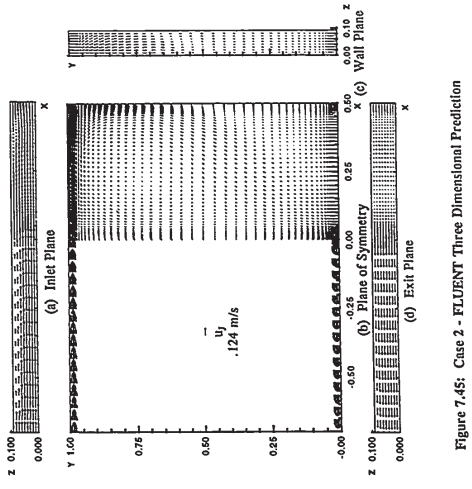


Figure 7.45: Case 2 - FLUENT Three Dimensional Prediction



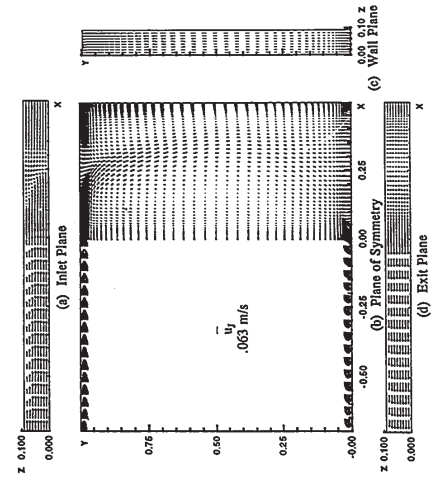


Figure 7.46: Case 3 - FLUENT Three Dimensional Prediction

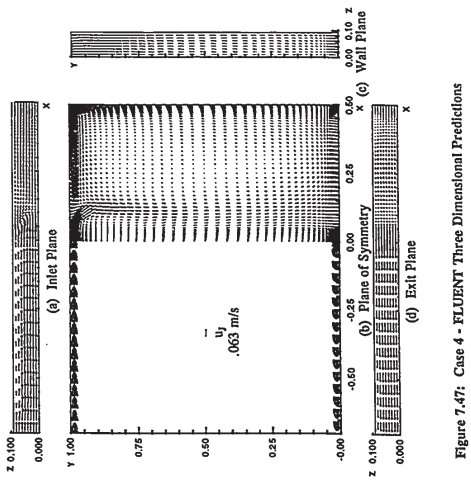


Figure 7.47: Case 4 - FLUENT Three Dimensional Predictions



A region of backflow is also observed at the top of the wall plane. In this plane, the region of backflow is also smaller at the plane of symmetry and larger at the face of the cavity. Once the boundary layer develops, the flow has a nearly uniform distribution above the separation region. At the face of the cavity the separation height is approximately 0.45 while at the plane of symmetry the separation height is 0.30 dimensionless units. At the face of the cavity, the downward moving fluid would have less inertia due to shear from the cavity face. Below the separation region, the flow has a uniform velocity distribution.

In the exit plane, the flow appears to be nearly two-dimensional as the vectors are similar in length across the cavity. The profile in the exit developing length is slightly flatter than the profile in the inlet developing length.

The three-dimensional FLUENT prediction for case 2 is presented in Figure 7.45. The flow in the inlet plane is almost identical to the previous case in terms of developing length, boundary layer thickness and region of backflow and will therefore not be discussed for brevity.

The flow in the wall plane is also similar to the preceding case but the separation location varies from 0.5 at the plane of symmetry to 0.63 at the cavity face. This variation in separation location is, again, due to shear at the cavity face. The buoyancy source term would almost be a constant across the cavity as the temperature distribution is nearly uniform. In the exit plane, the flow is also nearly identical to the flow in the exit plane of case 1.

The predictions for case 3 are presented in Figure 7.46. In the inlet developing length, the predicted flow field is similar to the preceding two cases. However, in the cavity, the flow lacks two-dimensionality in the region of separation. The velocity vectors in this plane suggests the penetration depth is approximately 0.10 at the cavity face and 0.2 at the plane of symmetry.



In the wall plane the flow appears to be nearly two-dimensional everywhere except at the top of the cavity. As the fluid approaches the top of the cavity, it turns toward the plane of symmetry. As in the previous cases, the flow in the wall plane is nearly two-dimensional.

The flow in the plane of symmetry differs significantly from the two-dimensional predictions (see Figure 7.42). Both solutions predict the flow to be buoyancy dominated, but the three-dimensional results predict the inlet jet to penetrate farther into the cavity. Thus, the inertially driven cell consumes approximately two thirds of the cavity for the three-dimensional model while the two-dimensional model predicts this cell to be very small. From the inlet plane, it appears that the flow separates from the top wall at $X \approx 0.3$. However this plane is 4 mm from the top of the cavity. Enlargement of this region in the plane of symmetry shows the flow actually separates from the top boundary at an X coordinate of 0.23 dimensionless units.

The three-dimensional FLUENT predictions for case 4 are presented in Figure 7.47. Qualitatively the observations for this case are similar as for the previous case in terms of two-dimensionality, variation of separation location and maximum inlet jet penetration.

The dimensionless separation location for both the two-dimensional and three-dimensional FLUENT predictions are presented in Table 7.7.



Table 7.7: Summary of Dimensionless Separation Locations for FLUENT Predictions

| | FLUENT 2D | | FLUENT 3D* | |
|---|---|---|---|---|
| Case | $Y_{sep}$ | $X_{rcn}$ | $Y_{sep}$ | $X_{rcn}$ |
| 1 | 0.3 | - | 0.27 | - |
| 2 | 0.58 | - | 0.53 | - |
| 3 | - | 0.035 | - | 0.23 |
| 4 | - | 0.025 | - | 0.08 |

* In the Plane of Symmetry

## 7.6 Comparison of Experimental and Numerical Results

Thus far, all of the predictions have been presented in terms of velocity vector plots with no detailed comparison with the experimental results. Comparison of each type of prediction and the experiment results give insight into the physical nature of the flow and the numerical models needed to successfully predict the flow. The main difference between the predictions of section 7.5.1 and the two-dimensional FLUENT predictions is the turbulence model as the predictions of section 7.5.1 uses a low Reynolds number k-ε model and FLUENT is based on a high Reynolds number k-ε model with wall functions. Comparison between the two-dimensional and three-dimensional predictions of FLUENT allows the two-dimensionality of the flow to be studied. The velocity and turbulence fields are studied in section 7.6.1 and the temperature and heat transfer profiles are studied in section 7.6.2.

### 7.6.1 Flow Field and Separation Height Comparison

For a quantitative comparison between each of the predictions and the experiment results, contour plots are used for the dimensionless stream function, turbulent kinetic energy and turbulent viscosity.

The dimensionless stream function, $\psi^*$, is computed from the dimensionless velocity fields using the definition

$$U = \frac{\partial \psi^*}{\partial Y} \quad \text{and} \quad V = -\frac{\partial \psi^*}{\partial X} \tag{7.7}$$

For case 1, contours of stream function are presented for the experimental data, the low Reynolds number turbulence model predictions, two-dimensional FLUENT predictions and three-dimensional FLUENT predictions in Figure 7.48. For the three-dimensional FLUENT predictions, the stream function is computed in the plane of symmetry using the horizontal and vertical velocity fields (U and V components of velocity). The single legend on this figure applies to the experimental measurements and all the predictions. Contour number 5 corresponds to a stream function value of zero and thus shows the division of the clockwise and counterclockwise rotating cells. For clockwise rotating fluid, the value of stream function is less than zero and for counterclockwise rotating fluid, the stream function value is greater than zero. The small cell at the top of the cavity adjacent to the heated wall appears to be approximately the same size for the experiment and all of the predictions. However, in the bottom corner adjacent to the heated wall, the counterclockwise cell is predicted in all of the predictions to be larger than the experimental results. The strength of the inertially driven cell is predicted well as contour numbers 1 and 2 are approximately the same size and shape for all simulations.



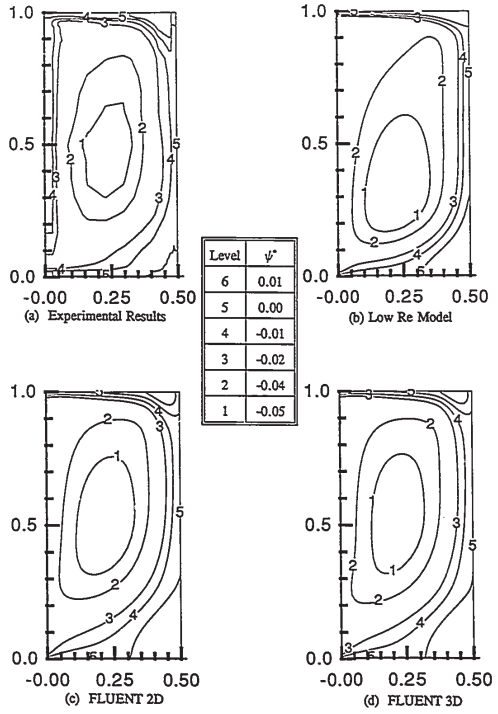


| Level | $\psi^*$ |
|---|---|
| 6 | 0.01 |
| 5 | 0.00 |
| 4 | -0.01 |
| 3 | -0.02 |
| 2 | -0.04 |
| 1 | -0.05 |

Figure 7.48: Case 1 - Streamline Comparison



The stream function contours for case 2 are shown in Figure 7.49. The strength of the inertially driven cell is about the same for the experiment and predictions as contour number 1 is about the same size in each of the plots. The strength of the buoyancy driven cell in the bottom corner adjacent to the heated wall is overpredicted for the two-dimensional simulations as the size of contour number 6 is much larger for these predictions and contour number 7 does not exist in the experimental plot. In fact, the strength of this cell in the low Reynolds Number model predictions is so powerful, it causes the separation location to be predicted high up the wall as compared to the experimental results. The three-dimensional solution has the best agreement with the experimental data as the separation location is predicted in the proper location and the strength of the buoyancy cell is only slightly overpredicted. Since the three-dimensional FLUENT streamline plot is in better agreement than the two-dimensional FLUENT plot, it suggests that three-dimensional effects are important in the prediction of the flow field.

Streamlines for case 3 are presented in Figure 7.50. The experimental data shows the inlet jet to flow across the top of the cavity, turn downward along the heated wall and separate at approximately two thirds the height of the cavity. All of the simulations predict the jet to separate from the top boundary after it enters the cavity. Contour number 5 has a stream function value of zero and thus shows the division between the cold inlet flow and the heated buoyancy induced flow. Figure 7.50 (b) show the maximum penetration of the cold jet to be $X \approx 0.15$ just after the jet enters the cavity. This jet flows down the vertical wall in the region of $X < 0.07$. The two-dimensional FLUENT predictions show inlet jet to always be in the region $X < 0.1$. The three-dimensional predictions show the inlet flow to penetrate up to $X \approx 0.35$. For this prediction, the resulting buoyant flow is restricted to a tall and narrow cell adjacent to the heated wall. All of the numerical models tested can neither quantitatively or qualitatively



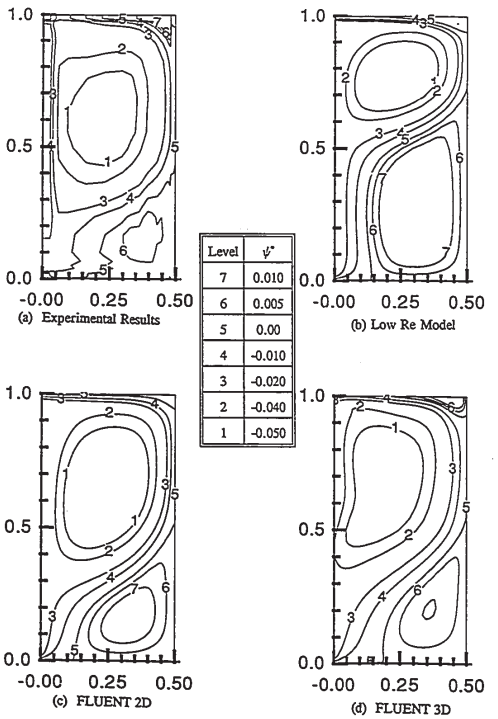


| Level | $\psi^*$ |
|---|---|
| 7 | 0.010 |
| 6 | 0.005 |
| 5 | 0.00 |
| 4 | -0.010 |
| 3 | -0.020 |
| 2 | -0.040 |
| 1 | -0.050 |

Figure 7.49: Case 2 - Streamline Comparison

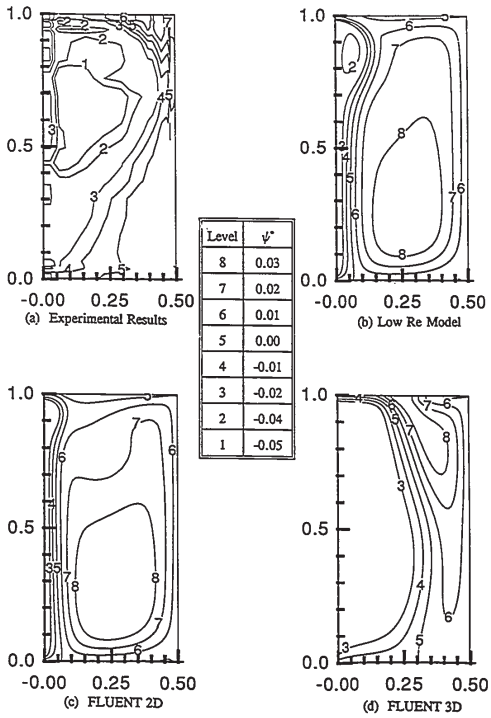


| Level | $\psi^*$ |
|---|---|
| 8 | 0.03 |
| 7 | 0.02 |
| 6 | 0.01 |
| 5 | 0.00 |
| 4 | -0.01 |
| 3 | -0.02 |
| 2 | -0.04 |
| 1 | -0.05 |

Figure 7.50: Case 3 - Streamline Comparison



predict the flow field adequately for case 3. The strength of the buoyancy force is overpredicted since none of the simulations are even capable of predicting the correct flow regime. The three-dimensional prediction has the best agreement as this simulation predicts the buoyancy cell to be the smallest (and jet penetration to be the greatest). The low Reynolds number model predictions are marginally better than the two-dimensional FLUENT simulations as the region of inertially driven flow is slightly larger for the former predictions.

The experimental streamlines for case 4 are shown in Figure 7.51 (a). The circular streamlines in the core of the cavity are not convection rolls as seen in Bernard convection, but are due to experimental errors. In the core of the cavity the flow is nearly stagnant so the measured velocities will be small positive or negative values. When these velocities are integrated to obtain the stream function, the errors are combined. Thus, small errors in the velocities combine to create larger errors in the calculation of stream function. It should also be noted that all of the cells have positive values of stream function which suggests the fluid in all of the cells is rotating counterclockwise. This is not physically realistic when considering the fluid between two cells. The motion from the lower cell would promote fluid motion in the negative X direction while the upper cell would promote fluid motion in the positive X direction. This would create a great deal of shear in the flow and is therefore unlikely to occur. Although all of the simulations overpredict the strength of the buoyancy cell, the overall flow field, being buoyancy dominated is predicted adequately by all of the models. Once again, the three-dimensional results have the best agreement as contour number 2 extends farther into the cavity for this prediction.

The separation location for the experiment, low Reynolds number predictions, two-dimensional FLUENT simulations and the three-dimensional FLUENT predictions are



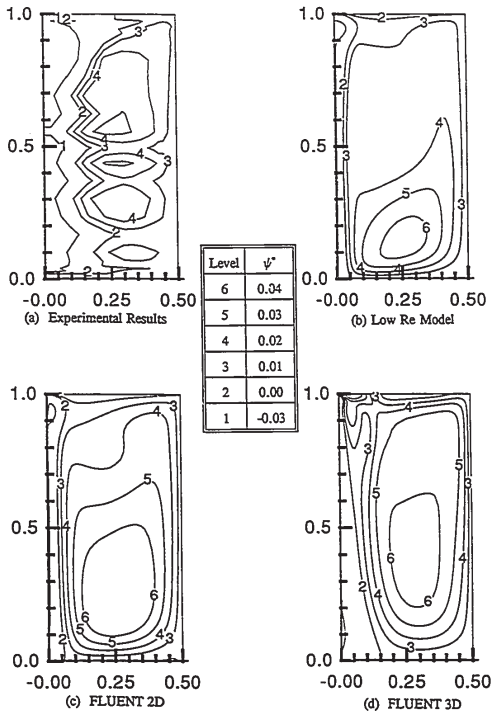


| Level | $\psi^*$ |
|---|---|
| 6 | 0.04 |
| 5 | 0.03 |
| 4 | 0.02 |
| 3 | 0.01 |
| 2 | 0.00 |
| 1 | -0.03 |

Figure 7.51: Case 4 - Streamline Comparison



summarized in Table 7.8. The separation locations quoted for the experimental data are the arithmetic mean of the values presented in Table 7.3 and the values from the three-dimensional FLUENT predictions are in the plane of symmetry.

Table 7.8: Separation Location Comparison

| | Experimental Data* | | Low Re Model Predictions | | FLUENT 2D | | FLUENT 3D | |
|---|---|---|---|---|---|---|---|---|
| Case | $Y_{sep}$ | $X_{pen}$ | $Y_{sep}$ | $X_{pen}$ | $Y_{sep}$ | $X_{pen}$ | $Y_{sep}$ | $X_{pen}$ |
| 1 | 0.29 | - | 0.31 | - | 0.30 | - | 0.27 | - |
| 2 | 0.49 | - | 0.76 | - | 0.58 | - | 0.53 | - |
| 3 | 0.62 | - | - | .025 | - | .035 | - | 0.23 |
| 4 | - | .083 | - | .025 | - | .025 | - | 0.08 |

*Average of Values in Table 7.3

The predicted separation heights for case 1 are in excellent agreement with the experimental data. All of the models are capable of predicting the separation location within experimental error. For case 2, the low Reynolds number model predicts the separation location to be approximately 50% higher than the experimental results. Both of the FLUENT predictions of the separation height are in good agreement with the experiment for case 2. All of the models have difficulty predicting the separation location for case 3 as the simulations predict the separation to occur on the top boundary of the cavity while the experiment shows the separation occurs on the heated wall. For buoyancy dominated flow (case 4), the two-dimensional models underpredict the location of separation on the top boundary of the cavity while the three-dimensional FLUENT calculations have good agreement with the experimental results. It must be noted that both of the two-dimensional simulations predict very little difference in the

separation location between cases 3 and 4. However, the Archimedes number for case 4 is approximately twice that of the Archimedes number for case 3. Thus, the prediction of separation in the two-dimensional simulations are insensitive to Archimedes number for buoyancy dominated flow. The three-dimensional calculations are sensitive as the separation location for case 3 and 4 are 0.23 and 0.08 respectively.

The results in Table 7.8 and Figures 7.48 to 7.51 suggest that all of the models adequately predict the flow field for case 1. The solution of isothermal recirculating turbulent flow in cavities can be successfully modelled as shown by the present work and the work of Johnson [59]. However, differences between the predictions and the experimental results are observed in the cases with heat transfer. The addition of buoyancy in the cavity increases the complexity of the problem as this body force introduces non-isotropic turbulence into the cavity. Davidson [53], Hanjalić and Vasić [85] and Hanjalić [86] studied non-isotropic effects due to buoyancy when applied to natural convection in a cavity. Davidson [53] states the k-ε model is deficient in buoyant flows as all of the normal Reynolds stresses are assumed to be equal but in actual fact, the vertical fluctuating component of velocity is damped and the horizontal component is amplified. This inadequacy in the turbulence modelling may lead to unrealistic predictions of the Reynolds stress and the turbulent heat flux. The k-ε model is used extensively by engineers as it is computationally inexpensive, gives reasonable results for many problems and it usually converges easily. Turbulence models that do account for non-isotropy such as the Reynolds stress model and the algebraic stress model are significantly more expensive to implement in terms of CPU time and may be unstable. The low Reynolds number k-ε model was selected for the turbulence model in the present work as the literature review showed that it was the simplest model that may be able to yield reasonable results (see sections 2.4 and 2.5). In addition, the



k-ε model may be considered the industrial standard for turbulence modelling and it would be insightful to study the performance of this model when applied to mixed convective problems. The remainder of this section discusses the predictions of the turbulence quantities for the cases with heat transfer.

The dimensionless turbulent kinetic energy and the dimensionless turbulent viscosity for cases 2 to 4 are presented in Figures 7.52 to 7.57. The dimensionless turbulent kinetic energy, $k^*$, is defined by equation 5.19 and the dimensionless turbulent viscosity, $\nu^*$, is defined as the viscosity ratio and is computed from

$$\nu^* = \frac{\nu_T}{\nu_L} \tag{7.8}$$

The contour plots for case 3 are discussed in detail and the plots for the remaining cases are not discussed as a similar conclusion can be drawn from those cases. However, the plot for cases 2 and 4 are included in the present work for completeness. In Figure 7.54, contour plots of dimensionless turbulent kinetic energy are plotted for the low Reynolds number predictions and the FLUENT predictions. Experimental values of turbulent kinetic energy could not be computed as the fluctuating component of velocity in the Z direction was not measured. In general, the turbulent kinetic energy for the two-dimensional FLUENT predictions is higher than the other predictions. Figure 7.54 (b) shows the turbulent kinetic energy is greater than 0.005 (contour number 2) in the majority of the cavity. In addition, the fluid flowing down the adiabatic vertical wall has a dimensionless turbulent kinetic energy greater than 0.03 (contour number 4). Both the three-dimensional FLUENT predictions and the low Reynolds number model calculations predict regions in the cavity where the turbulent kinetic energy is less than contour number 2. The low Reynolds number model only predicts a small region in the cavity where the kinetic



| Level | $k^*$ |
|---|---|
| 6 | 0.020 |
| 5 | 0.008 |
| 4 | 0.004 |
| 3 | 0.003 |
| 2 | 0.002 |
| 1 | 0.00 |

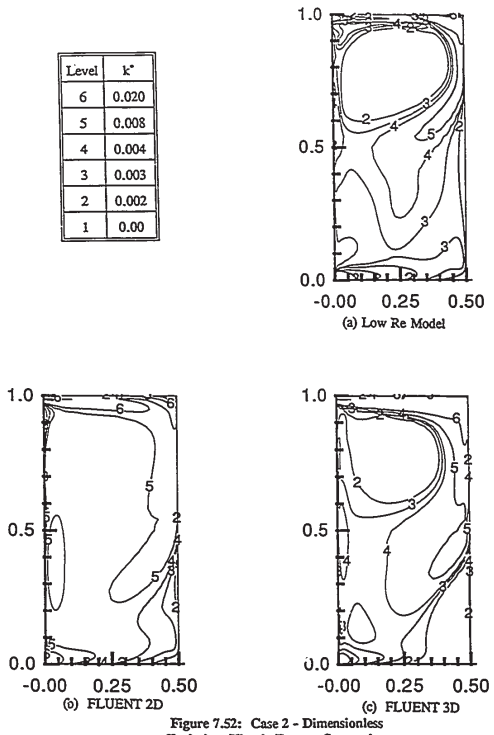


Figure 7.52: Case 2 - Dimensionless Turbulent Kinetic Energy Comparison



| Level | $\nu^*$ |
|---|---|
| 8 | 100 |
| 7 | 80 |
| 6 | 60 |
| 5 | 40 |
| 4 | 20 |
| 3 | 10 |
| 2 | 2 |
| 1 | 0 |

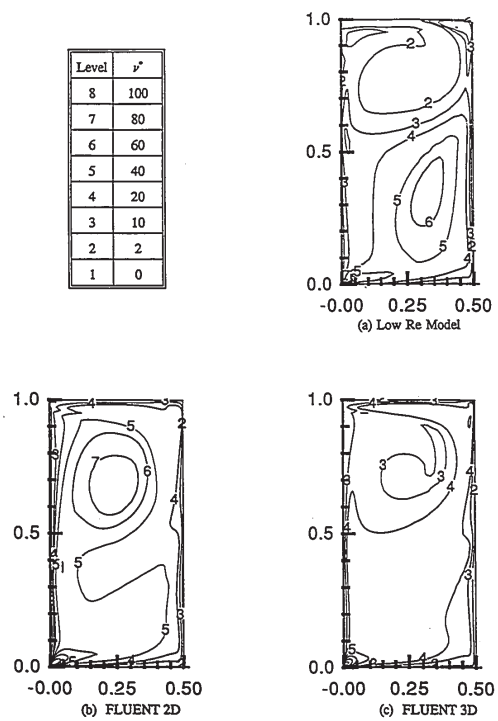


Figure 7.53: Case 2 - Dimensionless Turbulent Viscosity Comparison

| Level | k* |
|---|---|
| 4 | 0.030 |
| 3 | 0.010 |
| 2 | 0.005 |
| 1 | 0.000 |

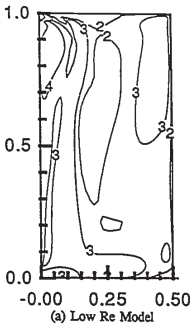

(a) Low Re Model

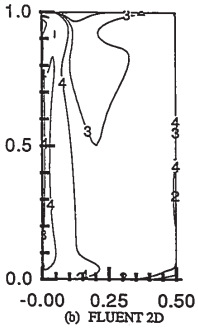

(b) FLUENT 2D

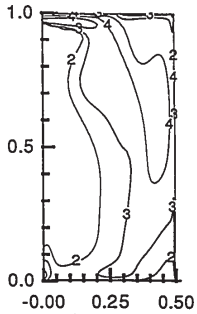

(c) FLUENT 3D

Figure 7.54: Case 3 - Dimensionless Turbulent Kinetic Energy Comparison



| Level | ν* |
|---|---|
| 5 | 80 |
| 4 | 60 |
| 3 | 40 |
| 2 | 20 |
| 1 | 0 |

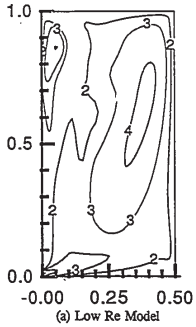

(a) Low Re Model

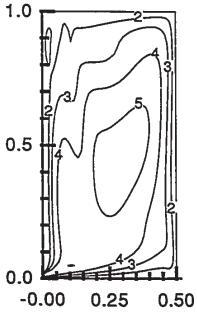

(b) FLUENT 2D

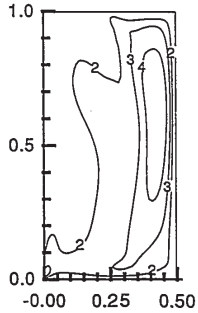

(c) FLUENT 3D

Figure 7.55: Case 3 - Dimensionless Turbulent Viscosity Comparison



| Level | k* |
|---|---|
| 6 | 0.050 |
| 5 | 0.030 |
| 4 | 0.020 |
| 3 | 0.010 |
| 2 | 0.001 |
| 1 | 0.000 |

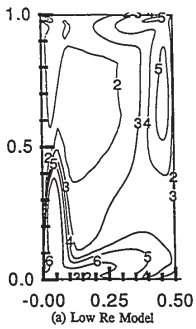

(a) Low Re Model

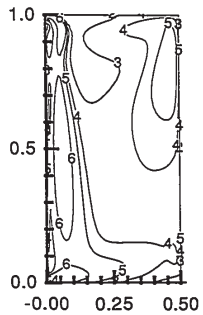

(b) FLUENT 2D

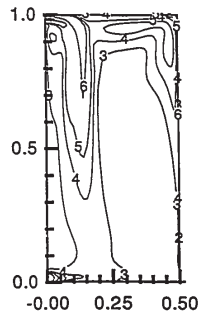

(c) FLUENT 3D

Figure 7.56: Case 4 - Dimensionless Turbulent Kinetic Energy Comparison



| Level | ν* |
|---|---|
| 7 | 100 |
| 6 | 80 |
| 5 | 60 |
| 4 | 40 |
| 3 | 20 |
| 2 | 2 |
| 1 | 0 |

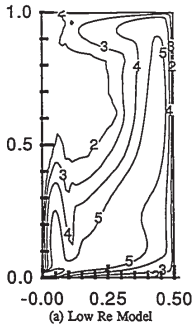

(a) Low Re Model

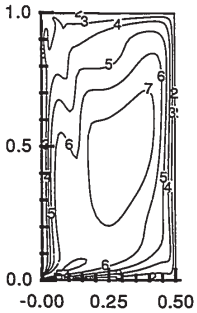

(b) FLUENT 2D

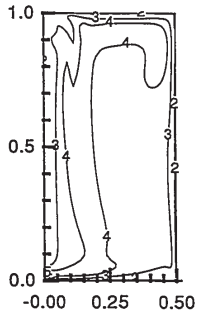

(c) FLUENT 3D

Figure 7.57: Case 4 - Dimensionless Turbulent Viscosity Comparison

energy exceeds contour number 4 (just below the entrance) and the three-dimensional FLUENT model predicts a slightly larger region. In summary, the two-dimensional FLUENT model predicts significantly higher levels of turbulent kinetic energy and the three-dimensional model predicts slightly higher levels than the low Reynolds number model.

Turbulent viscosity ratio contour plots are presented for case 3 in Figure 7.55. The two-dimensional calculations predict a high level of turbulent viscosity in the inertially driven cell just below the entrance. In this region, the low Reynolds number model predicts the turbulent viscosity to be 60 times the laminar viscosity while the two-dimensional FLUENT code predicts this to be just over 40 times. In the remainder of the cavity, the two-dimensional high Reynolds number model typically predicts the turbulent viscosity ratio to be higher than the predictions of the low Reynolds number model. The shape of contour numbers 3 and 4 also differ as the low Reynolds number model predicts these contours to be tall and narrow adjacent to the heated wall while the high Reynolds number version predicts them to encompass the entire width of the cavity.

The turbulent viscosity contour plot of the three-dimensional high Reynolds number model is similar to the two-dimensional low Reynolds number model. The size and shape of contour number 2 is approximately the same for both models. These models also predict contour levels 3 and 4 to enclose a tall and narrow region adjacent to the heated wall. The contour plots differ slightly as the low Reynolds number calculations predict a high levels of turbulent viscosity just below the entrance and the compression of contour levels 3 and 4 against the heated boundary is more pronounced in the three-dimensional prediction. These differences are attributed to differences in the predicted velocity fields. Comparison of the flow fields in Figures 7.38 and 7.46 show the prediction of a small inertially driven cell just below the entrance in the



low Reynolds number predictions. This cell is not observed in the three-dimensional predictions. Thus, in this region, high levels of turbulent viscosity are predicted for the low Reynolds number case but not for the three-dimensional calculations. Figures 7.38 and 7.46 also show the buoyancy induced cell predicted by the three-dimensional case to be narrower than the cell predicted by the low Reynolds number model. Thus, the region of high turbulent viscosity is narrower in the three-dimensional simulation.

For all cases, the two-dimensional FLUENT calculations predict the turbulent viscosity higher than the other computations while the peak values for the low Reynolds number model and the three-dimensional high Reynolds number model are comparable. The predicted turbulence field for each model differs as the predicted velocity and temperature fields for each model also differed.

### 7.6.2 Temperature Field and Heat Transfer Comparison

The experimental horizontal temperature profiles at heights of 200, 140 and 80 mm (0.67, 0.47 and 0.27 dimensionless units respectively) are presented in Figure 7.13. These profiles are compared with the predicted profiles of the low Reynolds number model and the two-dimensional and three-dimensional FLUENT models in Figures 7.58 to 7.60.

The temperature profiles adjacent to the heated wall for case 2 is presented in Figure 7.58. At the 200 mm height, both of the FLUENT models predict a similar profile. These models slightly overpredict the temperature gradient at the boundary and the width of the boundary layer and they underpredict the temperature outside the boundary layer. The low Reynolds number turbulence model is distinctively different from the experimental data and the other predictions as the temperature gradient is significantly underpredicted and the core



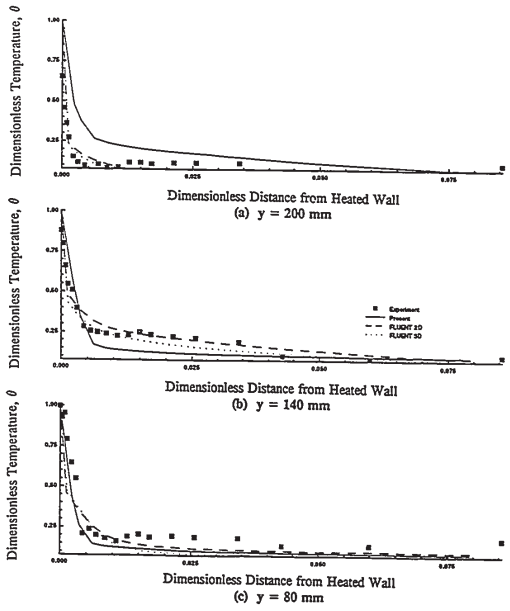


Figure 7.58: Case 2 - Horizontal Temperature Profile Comparison



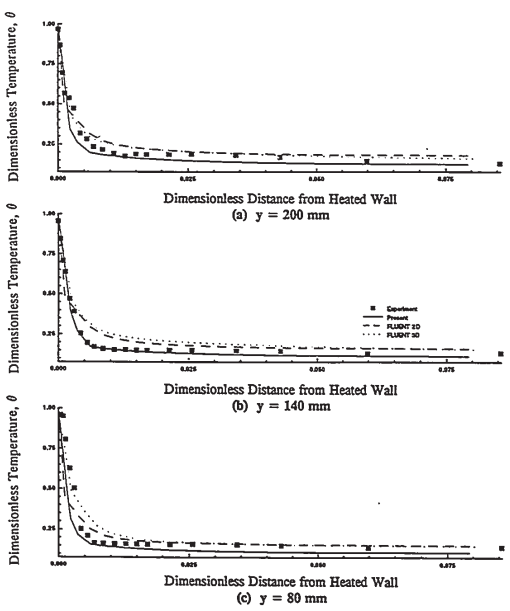


Figure 7.59: Case 3 - Horizontal Temperature Profile Comparison

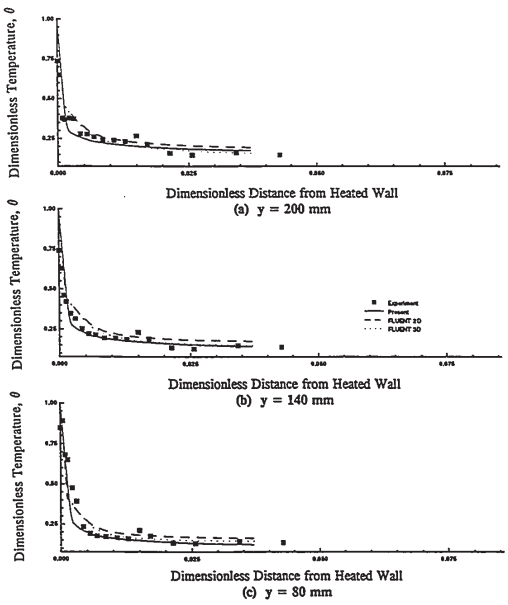


**Figure 7.60: Case 4 - Horizontal Temperature Profile Comparison**



temperature is overpredicted. This is consistent with the flow field as the low Reynolds number model predicted the separation height to be 0.76 dimensionless units. The dimensionless height corresponding to this 200 mm high profile is 0.67. Thus, for the low Reynolds number model, this temperature profile is in the warmer buoyancy driven cell (i.e. below the predicted separation location). Since the fluid is warm, the temperature difference between the wall and the fluid is low. This results in a reduced heat transfer rate and hence a lower temperature gradient at the wall. For the FLUENT predictions, the temperature profiles correspond to a location above the predicted and measured separation location. For these models, the fluid in this region is in the colder inertially driven cell. Since the temperature difference between the wall and the local fluid temperature is greater, the heat transfer rate is also greater (and hence the temperature gradient at the wall). At the 140 mm height, the FLUENT models adequately predict the temperature gradient at the wall while the low Reynolds number model underpredicts the gradient. All of the models underpredict the core temperature at this height. At the 80 mm height, all of the models overpredict the temperature gradient at the wall, adequately predict the boundary layer width and underpredict the core temperature.

The horizontal temperature profiles for case 3 are presented in Figure 7.59. For the 140 and 200 mm heights, all of the models adequately predict the temperature gradient at the wall. At the 80 mm height the two-dimensional models overpredict the wall gradient the three-dimensional model predicts it reasonably well. In general the low Reynolds number model correctly predicts the width of the boundary layer while the FLUENT models overpredict the boundary layer width. Outside the boundary layer, the FLUENT models overpredict the temperature while the low Reynolds number model slightly underpredicts the temperature. This figure suggests that the analysis of the temperature profiles is not a good measure of the ability



of a model to predict the flow field. Both the experimentally obtained temperature profiles and the predictions from the low Reynolds number model are in good agreement. Yet, the velocity profiles differ significantly as Figure 7.8 shows the flow separates on the heated wall and the model predicts the flow to separate on the top boundary (see Figure 7.38).

The temperature profiles for case 4 are presented in Figure 7.60. For this case the results are consistent for all three heights. At the wall, all three of the models predict the temperature gradient well. Both of the FLUENT models predict the thermal boundary layer to be thicker than the experimental data while the low Reynolds number model successfully predicts the width. Outside of the boundary layer, the two-dimensional FLUENT model consistently overpredicts the temperature while the other models adequately predict the temperature.

The comparison of heat transfer is presented in terms of Nusselt number profiles along the heated wall. The Nusselt number is defined as

$$\mathrm{Nu}_H = \frac{hH}{K} = \frac{H}{T_W - T_f}\frac{\partial T}{\partial x} = \frac{\partial \theta}{\partial X} \qquad (7.9)$$

where h is the local heat transfer coefficient.

For cases 2, 3, and 4, the variation of Nusselt number on the heated wall is presented in Figures 7.61 to 7.63 respectively. The predicted Nusselt numbers are computed from the dimensionless temperature gradient at the heated wall and the experimental Nusselt number is calculated from the electrical power input to the heaters.

Figure 7.61 shows the Nusselt number profiles along the heated wall for case 2. Qualitatively, the experiment and the predictions show the Nusselt number is highest at the top of the cavity, reduces to a local minimum at the separation location and increases slightly towards the bottom of the cavity. At the top of the cavity, the fluid motion is driven by the cold fluid



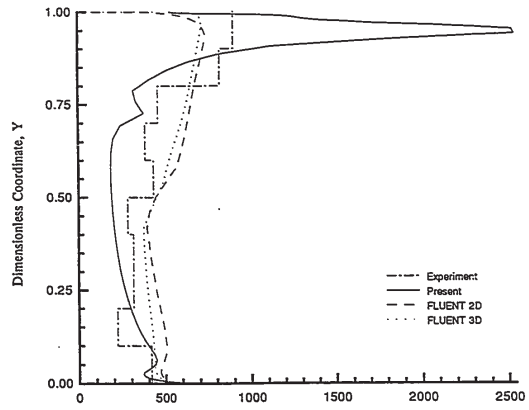


**Figure 7.61: Case 2 - Nusselt Number Profile Comparison**

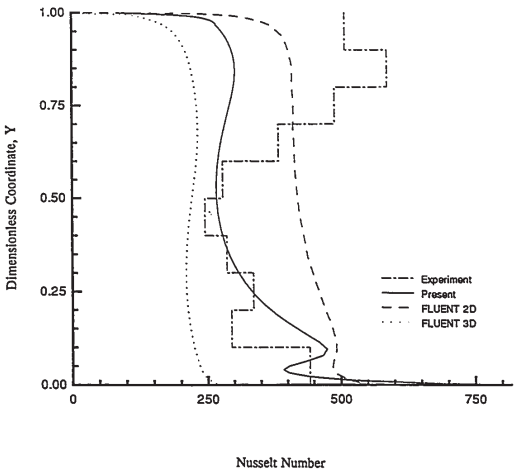


Figure 7.62: Case 3 - Nusselt Number Profile Comparison



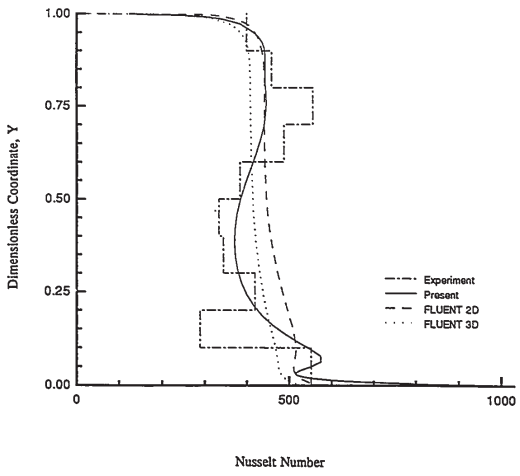


Figure 7.63: Case 4 - Nusselt Number Profile Comparison



entering the cavity. The temperature difference between the wall and the fluid in this region is large resulting in increased heat transfer rates. This is especially true for the low Reynolds number predictions as shown by a large spike in the Nusselt number profile. For this model the predicted inertially driven cell is smaller and hence mixes with the higher temperature buoyancy driven cell less than the other models. Thus the fluid temperature in the inertially driven cell is lower than for the other models and a large spike is shown in the Nusselt number profile. The Nusselt number profiles decrease in magnitude to approximately the separation height (see Table 7.8). Below the separation height, the fluid is rising adjacent to the heated wall. As the fluid rises, the local temperature of the fluid also rises as heat is transferred from the boundary to the fluid. Since the wall temperature is constant, the temperature difference between the wall and the fluid decreases as this fluid flows up the wall. Thus, the resulting Nusselt number profile in this region, decreases as the Y coordinate is increased. The Nusselt number profiles predicted by the FLUENT models are similar in size and have the same shape as the experimental profile. As already discussed, the low Reynolds number model overpredicts the heat transfer at the top of the cavity. All of the calculations predict a local minima in the region $Y < 0.1$ dimensionless units. This minima is attributed to the low velocity of the fluid in the corner of the cavity. This low fluid velocity results in a low convective heat transfer coefficient which in turn creates the observed minima.

The Nusselt number profiles for case 3 are presented in Figure 7.62. The experimental profile is qualitatively similar to the previous case. Experimentally, the flow regime for both of these cases is separated flow. Therefore, the discussion for the previous case also applies to the experimental curve. However, computationally, all of the simulations predict the flow to be buoyancy dominated. For this flow regime, the Nusselt number is largest at the bottom of the



cavity and is smallest at the top of the cavity. As the fluid flows up the heated wall, heat is transferred to the fluid causing the local temperature of the fluid to increase. As the local temperature increases, the temperature difference between the wall and the fluid decreases resulting in lower heat transfer rates (and hence lower Nusselt numbers). The two-dimensional simulations predict a local minima in the Nusselt number profile as in the previous case.

The Nusselt number distribution on the heated wall for case 4 is presented in Figure 7.63. In this figure, both the experimental and the predicted flow fields predict the flow to be buoyancy dominated. The discussion for the predictions of the previous case applies to all of the profiles on this figure.

A summary of the average Nusselt number on the heated wall is present ed in Table 7.9.

Table 7.9: Average Nusselt Number Comparison

| | Average Nusselt Number | | | |
|---|---|---|---|---|
| Case | Experimental Data* | Low Reynolds Number Model | FLUENT 2D | FLUENT 3D |
| 2 | 455. | 449. | 542. | 509. |
| 3 | 385. | 319. | 432. | 217. |
| 4 | 422. | 432. | 460. | 422. |

* Computed from Electric Power Supplied to Heaters

The low Reynolds number model has excellent agreement for cases 2 and 4 and underpredicts the heat transfer in case 3. The two-dimensional FLUENT simulations consistently overpredicted the Nusselt number for all cases. The three-dimensional FLUENT model slightly overpredicted the Nusselt number for case 2, significantly underpredicted the average Nusselt number for case 3 and has excellent agreement for case 4.

The average Nusselt number cannot be used for a meaningful comparison between the experimental results and the predictions of the models as this variable is an integrated quantity and is a measure of the overall performance of the cavity although it is encouraging that reasonably accurate predictions can be made.

The temperature and heat transfer results are consistent with results of the velocity fields. Differences between the two-dimensional and three-dimensional predictions of FLUENT suggest that three-dimensional effects are important for the successful simulation of the flow. The differences between the predictions of the two-dimensional models suggest the selection of an adequate turbulence model plays an important role in the prediction of the flow. As previously mentioned, the buoyancy in the cavity introduces non-isotropic turbulence. The non-isotropy may lead to unrealistic predictions of the Reynolds stress and the turbulent heat flux.

# CHAPTER 8

# CONCLUSIONS AND RECOMMENDATIONS

## 8.1 Contributions

The previously published literature addresses the problem of the lack of detailed experimental data for turbulent mixed convective flows [5]. The data presented in this thesis would aid the scientific community in the understanding of the relevant physics behind this class of flows. In addition, it would provide a data base for the verification of computer programs. In the past, computer codes for the prediction of internal buoyant flows were verified with the natural convection in a vertical rectangular cavity problem (as shown in Figure 2.2). Over ten years ago, a bench mark solution [20] was published for laminar flow in this configuration. This solution provided a reliable data base for the validation of laminar computer codes. In recent years, researchers have also obtained reasonable results for the turbulent case as shown in references [41,42,49,50,53,84]. As computers are developed with larger memories and higher computational ability, it is becoming feasible to use more complex turbulence models such as the algebraic stress model or the Reynolds stress model. These turbulence models have the ability to predict more complex flow problems. The experimental data presented here, provides a data base with an additional level of complexity as the flow may separate on a boundary in which heat is being transferred to the fluid.

The numerical work presented in this thesis, has applied both the low and high Reynolds number form of the k-ε turbulence model to mixed convective flows in enclosures. This model is used extensively in industry and may be considered the industrial standard for turbulence





modelling [53]. Thus, it is insightful to study the performance of this model when applied to this class of flows. In addition to the turbulence modelling, the performance of various mathematical models and numerical formulations have been investigated. The various numerical models and numerical formulations include the two-dimensionality of the flow, the effect of temperature on the fluid properties, the variation of the turbulent Prandtl number, the inclusion of the Yap correction, the order of the advective differencing, and the selection of algebraic solvers.

## 8.2 Conclusions

Comparison of the velocity plots in the plane of symmetry, inlet plane, exit plane, wall plane, exit region and the separation region show consistency between the plots. Since the data for these plots was collected days or even weeks apart, it suggests that the work is repeatable. The experimental velocity vector plots in the inlet, exit and wall planes show the flow has three-dimensional effects in the region of separation and in the corners adjacent to the heated wall.

A detailed study was carried out to investigate the performance of the low Reynolds number turbulence models. The results of this study indicated that, the laminar flow model gave inadequate predictions and the modified form of the Lam and Bremhorst model yielded slightly better predictions than the modified form of Jones and Launder.

A study was then conducted to examine the effects of the various secondary models. The results of this study show the variation of thermophysical properties significantly affected the predictions. The remaining modifications had little effect on the predicted flow field.

The predictions for the isothermal case (case 1) have excellent agreement with the experimental velocity field. Both, the high and low Reynolds number forms of the k-ε model, predicted this case well and no significant improvement was observed with the three-dimensional



model. Thus, a two-dimensional form of the k-ε turbulence model can successfully predict isothermal turbulent recirculating flow. This conclusion is consistent with the results of Johnson [59].

The simulations for the buoyancy dominated case (case 4) have good agreement with the measurements. The velocity field is adequately predicted for both the high and low Reynolds number forms of the k-ε model and the three-dimensional solution had slightly better agreement. For this case, the flow field is similar to the flow field for natural convection in a right vertical cavity. In these cavity flows, a primary vortex forms encompassing almost the entire cavity. The fluid in this primary vortex flows up the heated boundary, across the top, down the opposite vertical boundary, and back across the bottom (see verification study 3). In the natural convection case, the vortex is cooled by a cold vertical wall and in the mixed convection case, the vortex is cooled by a cold liquid jet flowing in the downward direction adjacent to the vortex. The results suggest that satisfactory predictions for buoyancy dominated flows can be made with the k-ε turbulence model. This result is consistent with the predictions of natural convection in a right vertical cavity [41,42,49,50].

The calculations for the intermediate Richardson number cases (case 2 and 3) have also been completed. Qualitatively, the predictions for small amounts of heating ($Ri < 1$) are in agreement with the experiment. For higher amounts of heating ($Ri \approx 10$) the predictions are poor. Three-dimensional effects are important as the three-dimensional FLUENT predictions are in better agreement with the experimental results than the two-dimensional predictions. Neither form of the k-ε turbulence model adequately predicts the flow for intermediate Richardson numbers. In general, the buoyancy component, is overpredicted.

### 8.3 Recommendations

More experimental studies are needed to increase the size of the data base for mixed convective flows. More specifically, data is needed for aiding flow and for higher Reynolds number flows. With an increased data base, overall heat transfer correlations could be developed and a range of Richardson numbers could be quantified in which the k-ε model yields satisfactory results. Detailed measurements of Reynolds stresses and turbulent heat fluxes would aid in the selection and development of turbulence models for this class of problems.

For mixed convection cavity flow, the successful prediction of the k-ε turbulence model appears to be limited to inertially dominated or buoyancy dominated flows. For intermediate values of Richardson numbers, the modelling of the Reynolds stress and the turbulent heat flux need to be investigated. A non-isotropic constitutive turbulence model such as the algebraic stress model or the Reynolds stress model may improve the predictions [48,53,85,86]. In this range of Richardson numbers the three-dimensional effects must also be accounted for.

The predictions using a two-dimensional k-ε turbulence model converged very slowly. The addition of a third dimension to this computer code and the inclusion of a higher order turbulence model would require an excessive amount of computer time for a solution of the present form of the code. The governing equations would have to be solved more efficiently to obtain reasonable computing times. Thus, an acceleration technique, such as the multilevel-multigrid approach would have to be incorporated into the present computer code.

For a complete understanding of turbulent mixed convective flows in cavities, there is a need for a great deal of experimental work to be completed in conjunction with numerical studies. The work presented in this thesis, provides one such investigation into this class of flows.

## REFERENCES


1. Gebhart, B., Jaluria, Y., Mahajan, R.L. and Sammakia, B., Buoyancy Induced Flows and Transport, Hemisphere Publishing Corp., New York, New York, 1988.
2. Oberkampf, W.L. and Crow, L.I., "Numerical Study of the Velocity and Temperature Fields in a Flow-Through Reservoir", J. Heat Transfer, Vol. 98, pp. 353-359, 1976.
3. Cabelli, A., "Storage Tanks-A Numerical Experiment", Solar Energy, Vol. 19, pp. 45-54, 1977.
4. Hjertager, B.H. and Magnussen, B.F., "Calculation of Turbulent Three Dimensional Jet Induced Flow in Rectangular Enclosures", Computers and Fluids, Vol. 9, pp. 395-407, 1981.
5. Hjertager, B.H. and Magnussen, B.F., "Numerical Prediction of Three Dimensional Turbulent Buoyant Flow in a Room", Heat Transfer and Turbulent Buoyant Convection, Spalding, D.B. and Afgan, N. (eds.), Hemisphere Publishing Corp., pp. 429-441, 1977.
6. Ahluwalia, A.K. and Shoukri, M., "Numerical Simulation of Turbulent Mixed Convection Flows", ASME Paper 83-WA/HT-13, ASME Winter Annual Meeting, 1983.
7. Cha, C.K. and Jaluria, Y., "Recirculating Mixed Convection flow for Energy Extraction", Int. J. Heat Mass Transfer, Vol. 27., pp. 1801-1812, 1984.
8. Cha, C.K. and Jaluria, Y.,:Effect of Thermal Buoyancy on the Recirculating Flow in a Solar Pond for Energy Extraction and Heat Rejection", J. Solar Energy Eng., Vol. 106, pp. 428-437, 1984.
9. Oosthuizen, P.H. and Paul, J.T., "Mixed Convective Heat Transfer In a Cavity", 23rd. ASME National Heat Transfer Conference, Denver, Colorado, Vol. 42, pp. 159-169, 1985.
10. Kumar, R. and Yuan, T., "Recirculating Mixed Convection Flows in Rectangular Cavities", J. Thermophysics, Vol. 3, No. 3, pp. 321-329, 1989.
11. Patankar, S.V., "Recent Developments in Computational Heat Transfer", J. Heat Transfer, Vol. 110, pp. 1037-1045, 1988.







12. Lechziner, M.A., "Modeling turbulent recirculating Flows by Finite Volume Methods-Current Status and Future Directions", Int. J. Heat and Fluid Flow, Vol 10. pp. 186-200, 1989.
13. Neiswanger, L., Johnson, G.A. and Carey, V.P., "An Experimental Study of High Raleigh Number Mixed Convection is a Rectangular Enclosure with Restricted Inlet and Outlet Openings", J. Heat Transfer, Vol. 109, pp. 446-453, 1987.
14. Jaluria, Y. and Cooper, L.Y., "Negatively Buoyant Wall Flows Generated in Enclosure Fires", Prog. Energy Combust. Sci., Vol. 15, pp. 159-182, 1989.
15. Catton, I., "Natural Convection in Enclosures", Proc. of the Sixth Int. Heat Trans. Conf., Vol. 6, 1978, pp. 13-31.
16. Ostrach, S., "Natural Convection Heat Transfer in Cavities and Cells", Proc. of the Seventh Int. Heat Trans. Conf., Vol. 1, 1982, pp. 365-379.
17. Ostrach, S., "Natural Convection in Enclosures", ASME J. Heat Transfer, Vol. 110, 1988, pp. 1175-1190.
18. Mallison, G.D. and de Vahl Davis, G., "Three Dimensional Natural Convection in a Box: A Numerical Study", J. Fluid Mech., Vol. 83, 1977, pp. 1-31.
19. De Vahl Davis, G. and Jones, I.P., "Natural Convection in a Square Cavity: A Comparison Exercise", Int. J. Numer. Methods Fluids, Vol. 3, 1983, pp. 227-248.
20. De Vahl Davis, G. and Jones, I.P., "Natural Convection in a Square Cavity: A Bench Mark Numerical Solution", Int. J. Numer. Methods Fluids, Vol. 3, 1983, pp. 249-264.
21. Hortmann, M., Peric, M. and Scheurer, G., "Finite volume Multigrid Prediction of Laminar Natural Convection: Bench Mark Solutions", Int. J. for Num. Meth. in Fluids, Vol. 11, 1990, pp. 189-207.
22. Hyun, J.M. and Lee, J.W., "Numerical Solutions for Transient Natural Convection in a Square Cavity with Different Sidewall Temperatures", Int. J. Heat and Fluid Flow, Vol. 10, 1989, pp.146-151.
23. Markatos, N.C., "Computer Simulation Techniques of Turbulent Flows" Ch. 31 of Encyclopedia of Fluid Mechanics, 1987.
24. Launder, B.E. and Spalding, D.B., "Lectures in Mathematical Modeling of Turbulence", Academic Press, 1972.
25. Rodi, W., "Examples of Turbulence Models for Incompressible Flows", AIAA, Vol 20, pp. 872-879, 1981.





26. Rodi, W., "Turbulence Models for Environmental Problems",Prediction Methods for Turbulent Flows , Kollman, W. (ed.), Hemisphere Publishing Corp., pp. 259-349, 1980.
27. Reynolds, W.C. and Cebeci, T., "Calculation of Turbulent Flows", Turbulence, Bradshaw, P. (ed.), Springer-Verlag, 1978.
28. Markatos, N.C., and Pericleous, K.A., "Laminar and Turbulent Natural Convection in an Enclosed Cavity", Int. J. Heat Mass Transfer, Vol. 27, pp. 755-772, 1984.
29. Markatos, N.C., and Malin, M.R., "Mathematical Modeling of Buoyancy Induced Smoke Flow in Enclosures", Int. J. Heat Mass Transfer, Vol. 25, pp. 63-75, 1982.
30. Ahluwalia, A.K. and Shoukri, M., "Numerical Simulation of Turbulent Mixed (Forced and Free) Convection Flows", Ontario Hydro Research Division Report No. 83-81-K, 1983.
31. Launder, B.E. and Spalding D.B., "The Numerical Computation of Turbulent Flows", Comp. Meths. Appl. Mech. Engrng., Vol. 3, pp. 269-289, 1974.
32. Ciofalo, M. and Collins, M.W., "k-ε Predictions of Heat Transfer in Turbulent Recirculating Flows using an Improved Wall Treatment", Numerical Heat Transfer, Part B, Vol. 15, pp. 21-47, 1989.
33. Patel, V.C. and Chen, H.C., "Turbulent Wake of a Flat Plate", AIAA, Vol. 25, No. 8, pp. 1078-1085, 1987.
34. Launder, B.E., "Numerical Computation of Convective Heat Transfer in Complex Turbulent Flows: Time to Abandon Wall Functions?", Int. J. Heat Mass Transfer, Vol. 27. pp. 1485-1491, 1984.
35. Patel, V.C., Rodi, W., and Scheuerer, G., "Turbulence Models for Near Wall and Low Reynolds Number Flows: A Review", AIAA, Vol. 23, pp. 1308-1319, 1984.
36. Launder, B.E., "On the Computation of Convective Heat Transfer in Complex Turbulent Flows", J. Heat Transfer, Vol. 110, pp. 1112-1128, 1988.
37. Henkes, R.A.W.M. and Hoogendoorn, C.J., "Comparison of Turbulence Models for the Natural Convection Boundary Layer along a Heated Vertical Plate", Int. J. Heat Mass Transfer, Vol. 32, No. 1, pp. 157-169, 1989.
38. Jones, W.P. and Launder, B.E., "The Prediction of Laminarization with a Two-Equation Model of Turbulence", Int. J. Heat Mass Transfer, Vol. 15, 1972, pp. 301-314.
39. Lam, C.K.G. and Bremhorst, K.A., "Modified Form of the k-ε Model for Predicting Wall Turbulence", Journal of Fluids Engineering, Vol. 103, 1981, pp. 456-460.

40. Chien, K.-Y., "Predictions of Channel and Boundary-Layer Flows with a Low Reynolds Number Turbulence Model", AIAA Journal, Vol. 20, 1982, pp. 33-38.

41. Giel, P.W., "A Numerical and Experimental Study of High Raleigh Number Natural Convection in Enclosures", Ph.D. Thesis, Pennsylvania State University, 1988.

42. Davidson, L., "Calculation of the Turbulent Buoyancy Driven Flow in a Rectangular Cavity using an Efficient Solver and Two Different Low Reynolds Number k-ε Turbulence Models", Numer. Heat Transfer, Part A, Vol. 18, pp. 129-147, 1990.

43. Yap, C., "Turbulent Heat and Momentum Transfer in Recirculating and Impinging Flows", Ph.D. Thesis, University of Manchester, U.K., 1987.

44. Ince N. Z. and Launder, B.E., "On the Computation of Buoyancy Driven Turbulent Flows in Rectangular Enclosures", Int. J. Heat and Fluid Flow, Vol. 10, No. 2, pp. 110-117, 1989.

45. Iacovides, H. and Launder, B.E., "PSL - An Economical Approach to the Numerical Analysis of Near Wall, Elliptic Flow", Technical Brief in J. Fluids Eng., Vol. 106, pp. 241-242, 1984.

46. Chen, H.C. and Patel, V.C., "Practical Near Wall Turbulence Models for Complex Flows Including Separation", AIAA Paper No. 87-1300, 1987.

47. Abrous, A., "A Numerical Study of the Turbulent Free Convection in Rectangular Cavities", Ph.D. Thesis, University of Washington, 1988.

48. Silva, D.J. and Emery, A.F., "A Preliminary Comparison of the k-ε and Algebraic Stress Models for Turbulent Heat Transfer in a Square Enclosure", Proc. of the National Heat Transfer Conference, Vol. 110, 1989, pp. 193-200.

49. Schmidt, F.W. and Wang, D.F., "Experimental Study of Natural Convection in an Enclosure", ASME Winter Annual Meeting, Phoenix, 1982, ASME Paper No. 82-WA/HT-72.

50. Phillips, R.E., "A Multilevel-Multigrid Method for Recirculating Flow", Ph.D. Thesis, Pennsylvania State University, 1984.

51. Humphrey, J.A.C. and To, W.M., "Numerical Simulation of Buoyant Turbulent Flow-II. Free and Mixed Convection in a Heated Cavity", Int. J. Heat Mass Transfer, Vol. 29, 1986, pp.593-610.





52. Cheesewright, R., King, K.J., and Ziai, S., "Experimental Data for the Validation of Computer Codes for the Prediction of Two-Dimensional Buoyant Cavity Flows", Significant Questions in Buoyancy Affected Enclosure or Cavity Flows, Vol. HTD60, 1986, pp. 75-81.

53. Davidson, L., "Second-order Corrections of the k-ε Model to Account for Non-isotropic Effects due to Buoyancy", Int. J. Heat Mass Transfer, Vol. 33, 1990, pp. 2599-2608.

54. Galpin, P.F. and Raithby, G.D., "Numerical Solution of Problems in Incompressible Fluid Flow: Treatment of the Temperature-Velocity Coupling", Numer. Heat Transfer, Vol. 10, 1986, pp. 409-426.

55. Henkes, R.A.W.M., Van der Vlugt, F.F., and Hoogendoorn, C.J., "Natural-Convection Flow in a Square Cavity Calculated with Low-Reynolds Number Turbulence Models", Int. J. Heat Mass Transfer, Vol. 34, 1991, pp. 377-388.

56. Lankhorst, A.M., Angirasa, D., and Hoogendoorn, C.J., "LDV Measurements of Buoyancy-Induced Flows in an Enclosure at High Rayleigh Numbers", Experimental Thermal and Fluid Science, Vol. 6, 1993, pp. 74-79.

57. Lankhorst, A.M., Henkes, R.A.W.M., and Hoogendoorn, C.J., "Natural Convection in Cavities at High Rayleigh Numbers, Computations and Validation", Second UK Natl. Conf. Heat Transfer, Vol. 1, 1988.

58. Drain, L.E., The Laser Doppler Technique, John Wiley & Sons Ltd., 1980.

59. Johnson, D.A., "An Experimental and Numerical Investigation of Turbulent Recirculating Flow within a Cavity with an Inlet Wall Jet", M. Eng. Thesis, McMaster University, Hamilton, Ont. 1988.

60. Buchave, P., George, W.K., and Lumley, J.L., The Measurement of Turbulence with the Laser Doppler Anemometer", Ann. Rev. Fluid Mech., Vol. 11, pp. 443-503, 1979.

61. Edwards, Robert V., ed., "Report of the Special Panel on Statistical Particle Bias Problems in Laser Anemometry", J. Fluids Eng., Vol. 109, pp. 89-93, 1987

62. Bradshaw, P. and Woods, J.D., "Geophysical Turbulence and Buoyant Flows", Turbulence, Bradshaw, P. (ed.), Springer-Verlag, 1978.

63. FLUENT, Version 4, Creare Incorporated, Hanover, N.H., U.S.A., 1991.

64. Plumb, O.A. and Kennedy, L.A., "Application of a k-ε Turbulence Model to Natural Convection From a Vertical Surface", J. Heat Transfer, Vol. 99, 1977, pp. 79-85.





65. Shaukatullah, H. and Gebhart, B., "The Effect of Variable Properties on Laminar Natural Convection Boundary-Layer Flow Over a Vertical Isothermal Surface in Water", Numer. Heat Transfer, Vol. 2, 1979, pp. 215-232.

66. White, F.M., Viscous Fluid Flow, McGraw-Hill, New York, 1974.

67. Kays, W.M. and Crawford, M.E., Convective Heat and Mass Transfer, McGraw-Hill, New York, 1980.

68. Patankar, S.V., Numerical Heat Transfer and Fluid Flow, Hemisphere Publishing Corp., U.S.A., 1980.

69. Patankar, S.V., "A Calculation Procedure for Two Dimensional Elliptic Situations", Numer. Heat Transfer, Vol. 4, 1981, pp. 409-425.

70. Van Doormal, J.P. and Raithby, G.D., "Enhancements of the SIMPLE Procedure for Predicting Incompressible Flow", Numer. Heat Transfer, Vol. 7, 1984, pp. 147-163.

71. Latimer, B.R. and Pollard, A., "Comparison of Pressure-Velocity Coupling Solution Algorithms", Numer. Heat Transfer, Vol. 8, 1985, pp. 635-652.

72. Jang, D.S., Jetli, R, and Acharya, S., "Comparison of the PISO, SIMPLER, and SIMPLEC Algorithms for the Treatment of the Pressure Velocity Coupling in Steady Flow Problems", Numer. Heat Transfer, Vol. 10, 1986, pp. 209-228.

73. Leschziner, M.A., "Modeling Turbulent Recirculating Flows by Finite-volume Methods——Current Status and Future Directions", Int. J. Heat Fluid Flow, Vol. 10, 1989, pp. 186-200.

74. Atias, M., Wolfshtein, M., and Isreali, M., "Efficiency of Navier Stokes Solvers", AIAA, Vol. 15, 1977, pp. 263-266.

75. Leonard, B.P., "A Stable and Accurate Convective Modeling Procedure based on Quadratic Upstream Interpolation", Comput. Methods Appl. Mech. Eng., Vol. 19, 1979, pp. 59-98.

76. Raithby, G.D., "Skew Upstream Differencing Schemes for Problems involving Fluid Flow", Comp. Meths. Appl. Mech. and Engng., Vol. 9, 1976, pp. 153-164.

77. Patankar, S.V., "Recent Developments in Computational Heat Transfer", J. Heat Trans., Vol. 110, 1988, pp. 1037-1045.

78. Raithby, G.D. and Schneider, G.E., "Elliptic Systems: Finite Difference Method II", Ch. 7 of Handbook of Numerical Heat Transfer, Minkowycz, W.J., Sparrow, E.M., Schneider, G.E. and Pletcher, R.H. (eds.), John Wiley & Sons, 1988.





79. Peaceman, D.W. and Rachford, H.H., "The Numerical Solution of Parabolic and Elliptic Differential Equations", J. Soc. Ind. Appl. Math., Vol. 3, 1955, pp. 28-41.

80. Stone, H.L., "Iterative Solution of Implicit Approximation of Multidimensional Partial Differential Equations", SIAM J. Numer. Anal., Vol. 5, 1968, pp. 530-558.

81. Schneider, G.E. and Zedan, M., "A Modified Strongly Implicit Procedure for the Numerical Solution of Field Problems", Numer. Heat Transfer, Vol. 4, 1981, pp. 1-19.

82. Le Quere, P., "Onset of Unsteadiness, Routes to Chaos and Simulations of Chaotic Flows in Cavities Heated from the Side: a Review of the Present Status", Proc. 10th Int. Heat Transfer Conf., Brighton, U.K., Vol. 1, pp. 281-296, 1994.

83. Henkes R.A.W.M. and Hoogendorn C.J., "Bifurcation to Unsteady Convection for Air and Water in a Cavity Heated from the Side", Proc. 9th Int. Heat Tranfer Conf., Jerusalem, Vol. 2, pp. 257-262, 1990

84. Nurnberg, G., "Numerical Investigation of Laminar and Turbulent Natural Convection in Enclosures", M. Eng. Thesis, McMaster University, Hamilton, Ont.,1988.

85. Hanjalić, K. and Vasić, S., "Computation of Turbulent Natural Convection in Rectangular Enclosures with an Algebraic Flux Model", Int. J. Heat Mass Transfer, Vol. 36, 1993, pp. 3603-3624.

86. Hanjalić, K., "Acheivements and Limitations in Modelling and Computation of Buoyant Turbulent Flows and Heat Transfer", Proc. 10th Int. Heat Tranfer Conf., Brighton, U.K., Vol. 1, pp. 1-18, 1994.

87. Haar, L., Gallagher, J.S., and Kell, G.S., NBS/NRC Steam Tables, Hemisphere, Washington, 1984.

# APPENDIX A

## Derivation of QUICK Grid Coefficients for a Non-Uniformly Spaced Grid

The QUICK coefficients are derived using the geometry of Figure A.1 [33]. The value of a variable at the west face, $\phi_w$, is calculated using a standard parabolic fit. This value of $\phi_w$ is used in the flux equation (eqn. 6.2).

$$\phi = ax^2 + bx + c \tag{A.1}$$

The points that the parabola is fit through depends on the sign of the normal velocity at the west face. If the velocity is positive, the parabola fits through $\phi_{WW}$, $\phi_W$, and $\phi_P$ as shown in Figure A.1 (a). For a negative velocity the parabola fits through $\phi_W$, $\phi_P$, and $\phi_E$ (see Figure A.1 (b)). The derivation for the QUICK grid coefficients is described in [33]. In general, a parabola must fit through the points

$$(-\delta x_1, \phi_W) \quad (\delta x_2, \phi_P) \quad (\delta x_3, \phi_3) \tag{A.2}$$

The values $\delta x_1$, $\delta x_2$, $\phi_W$, and $\phi_P$ are calculated as shown in Figure A.1 (c). The other values depend on the sign of the velocity at the west face, $u_w$ and are calculated as follows.

$$\begin{aligned} &\text{If } u_w > 0, \text{ then } \delta x_3 = -\delta x_1 - \Delta x_{i-2} \text{ and } \phi_3 = \phi_{WW} \\ &\text{If } u_w < 0, \text{ then } \delta x_3 = \delta x_2 + \Delta x_1 \text{ and } \phi_3 = \phi_E \end{aligned} \tag{A.3}$$





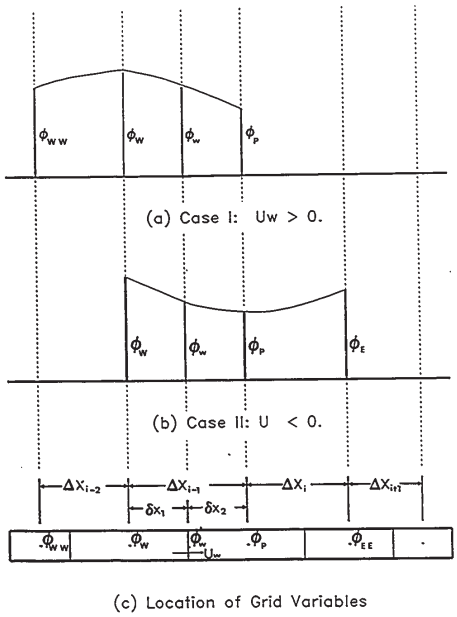


(c) Location of Grid Variables

**Figure A.1: QUICK Description**



Substituting equation (A.2) into equation (A.1) yields

$$\begin{aligned} \phi_P &= a\delta x_2^2 + b\delta x_2 + c \\ \phi_W &= a\delta x_1^2 + b\delta x_1 + c \\ \phi_3 &= a\delta x_3^2 + b\delta x_3 + c \end{aligned} \tag{A.4}$$

The solution of equation (A.4) yields

$$\phi_W = c = \frac{B_{1w}}{B_w}\phi_W - \frac{B_{2w}}{B_w}\phi_P + \frac{B_{3w}}{B_w}\phi_3 \tag{A.5}$$

where

$$\begin{aligned} B_{1w} &= \delta x_2 \delta x_3 (\delta x_2 - \delta x_3) \\ B_{2w} &= \delta x_1 \delta x_3 (\delta x_1 + \delta x_3) \\ B_{3w} &= \delta x_1 \delta x_2 (\delta x_1 + \delta x_2) \end{aligned} \tag{A.6}$$

and

$$B_w = B_{1w} - B_{2w} + B_{3w} \tag{A.7}$$

Other equations may be derived for the value of $\phi$ at the north, south and east faces.

# APPENDIX B

## UNCERTAINTY ANALYSIS

### B.1 Introduction

The reliability of the experimental results was estimated through examining the uncertainties associated with the calculated parameters. In general, if one parameter is a function of several variables which is given as follows:

$$\Phi = f(\phi_1, \phi_2, \ldots, \phi_n) \tag{B.1}$$

Then, its uncertainty can be expressed by

$$\frac{\Delta\Phi}{\Phi} = \sqrt{\left[\frac{\partial\Phi}{\partial\phi_1}\frac{\Delta\phi_1}{\Phi}\right]^2 + \left[\frac{\partial\Phi}{\partial\phi_2}\frac{\Delta\phi_2}{\Phi}\right]^2 + \ldots + \left[\frac{\partial\Phi}{\partial\phi_n}\frac{\Delta\phi_n}{\Phi}\right]^2} \tag{B.2}$$

The uncertainties in the basic measurements are estimated in Table B.1. The uncertainties in the tank dimensions are estimated from the accuracy of modern machine tools and the operator skill. The fluid temperature uncertainty is based on typical accuracy of thermocouples and the data acquisition system. The wall temperature has these uncertainties as well as an additional uncertainty since the thermocouples in the wall can differ by up to 0.5 °C. The flowmeter reading could easily be kept within a 5 mm band. The uncertainties in the heater voltage and resistance are estimated to be ±5% and ±10% respectively. The value for the resistance was provided by the manufacturer. The ratio of time on to time off was monitored by an oscilloscope. This ratio could be accurately measured and was consistent over time.

Table B.1: Uncertainties in the Basic Measurements

| | |
|---|---|
| Tank Dimensions L, H, W, D | ± 0.2 mm |
| T Fluid Temperature | ± 1 °C |
| $T_W$ Wall Temperature | ± 1½ °C |
| Q Flowmeter Reading | ± 2.5 mm |
| V Voltage of Power Supply | ± 5% |
| R Resistance of Heaters | ± 10% |
| $t^*$ Heater Time Ratio | ± 5% |

## B.2 Thermophysical Properties

The thermophysical properties of water are functions of temperature. Since there are uncertainties in the temperature measurements, the uncertainties are carried through to the calculation of the thermophysical properties. In addition, errors are introduced by the use of equations 5.49 to 5.53. For a representative test case (Case 3), the calculated uncertainties for the thermophysical properties at the reference temperature are presented in Table B.2. The error due to the uncertainty in temperature is calculated from equation B.2. A maximum and standard deviation are also cited in Equations 5.49 to 5.52. These deviations are cited from Giel [41] and are determined from the difference between the computed value and the value quoted in standard water tables [87]. The uncertainties quoted in Table B.2 have included both the uncertainty in the calculation of reference temperature and the uncertainty in the use of equations 5.49 to 5.53.



Table B.2: Uncertainty in the Thermophysical Properties

| | |
|---|---|
| $T_{REF}$ (° C) Reference Temperature | ± 0.9 |
| $\rho$ (kg/m$^3$) Density | ± 0.04% |
| $\mu$ (kg/m s) Dynamic Viscosity | ± 1.99% |
| k (W/m K) Thermal Conductivity | ± 0.196% |
| $C_p$ (J/kg K) Specific Heat | ± 0.07% |
| $\beta$ (1/K) Expansion Coefficient | ± 1.6% |

## B.3 Dimensionless Parameters

The uncertainties in the dimensionless parameters used to define the cases are due to uncertainties in tank dimensions, temperatures, inlet velocity and thermophysical properties. For Case 3, the uncertainties in the dimensionless parameters and the inlet velocity are calculated from equation B.2 and summarized in Table B.3. The largest uncertainty is in the calculation of Reynolds and Grashof numbers. A sensitivity study was performed using the low Reynolds number models. In this study, the dimensionless parameters were changed by the values listed in Table B.3. No significant changes in the predicted flow fields were observed in this study.



Table B.3: Uncertainties in the Dimensionless Parameters

| | |
|---|---|
| $u_j$ (m/s) Inlet Velocity | ± 5.5% |
| a Inlet Ratio | ± 2.5% |
| A Aspect Ratio | ± 0.15% |
| Pr Prandtl Number | ± 2% |
| $Re_D$ Reynolds Number | ± 6.3% |
| $Gr_H$ Grashof Number | ± 6.3% |

## B.4 Measured Quantities

In a recent study, Johnson [59] performed an error analysis on the laser doppler anemometer (LDA) technique. He found, that for a conventional LDA, the error in velocity measurement was typically to within 2%. In a study of natural convection in enclosures, Giel [41] performed an error analysis on the location of the LDA probe based on changing index of refraction considerations. Giel [41] found the probe location to be within 0.1 mm in the majority of the cavity. In regions where there are large temperature fluctuations and hence large changes in index of refraction this error was larger but could not be quantified. In addition, the laser beams were observed to bend considerably in these regions in the present work bringing the probe volume temporarily out of focus. This phenomena was observed near the separation region adjacent to the heated wall as shown by a low data rate. Typically, the error associated with thermocouples is taken to be about ± 1 °C. The data acquisition system has a very small error



so the uncertainty in the temperature measurements are taken to be the error in the thermocouple measurement. A test dial indicator with an accuracy of 0.001 inches (0.0254 mm) was used to locate the thermocouple. In reality, the thermocouple wires extending from the probe could move slightly due to fluid motion. This movement should be small in the vicinity of the heated wall since the fluid velocity is low in that region. The uncertainty associated with the thermocouple location is estimated to be approximately 0.05 mm. The uncertainty in the Nusselt number is computed from equation B.2 and is based on uncertainties in the geometry, the voltage supply, the heater resistance and the heater time ratio. The uncertainties in the measured quantities are summarized in Table B.4

Table B.4: Uncertainties in the Measured Quantities

| | |
|---|---|
| Velocity Measurement | ± 2% [59] |
| Location of Velocity Probe | ± 0.1 mm [41] |
| Temperature Measurement | ± 1 °C |
| Location of Temperature Probe | ± 0.05 mm |
| Nusselt Number | ± 15% |

# APPENDIX C

## EXPERIMENTAL DATA

The experimental velocity data presented in Figures 7.6 to 7.11 and the experimental temperature data presented in Figures 7.13 and 7.14 are stored on the floppy disk on the following page. The data for each case is stored in a separate ASCII file. The format for each file is similar. For a given case, *n*, the file is named CASEN.DAT and consists of eight tables. The tables for case *n* would be

Table C.*n*.1 - Velocity Data in the Inlet Plane for Case *n* in Figure 7.*n+5* (a)
Table C.*n*.2 - Velocity Data in the Plane of Symmetry for Case *n* in Figure 7.*n+5* (b)
Table C.*n*.3 - Velocity Data in the Wall Plane for Case *n* in Figure 7.*n+5* (c)
Table C.*n*.4 - Velocity Data in the Exit Plane for Case *n* in Figure 7.*n+5* (d)
Table C.*n*.5 - Velocity Data in the Separation Region for Case *n* in Figure 7.10
Table C.*n*.6 - Velocity Data in the Exit Region for Case *n* in Figure 7.11
Table C.*n*.7 - Horizontal Temperature Profiles for Case *n* in Figure 7.13
Table C.*n*.8 - Vertical Temperature Profile for Case *n* in Figure 7.14

The isothermal case (Case 1) consists of only the first six tables. In all of the tables except Table C.*n*.7, the coordinate system for Figure 3.1 applies and the dimensions of the coordinates are mm. Table C.*n*.7 uses a coordinate that is defined as the distance from the heated wall in dimensions of mm. All time-averaged and fluctuating velocities have the units of mm/s and the temperatures are made dimensionless with equation (5.17).

Additional copies of this data may be obtained from the author, Dr. M. Shoukri or Dr. P. Wood at

Department of Mechanical Engineering
McMaster University
Hamilton, Ontario
Canada
L8S 4L7